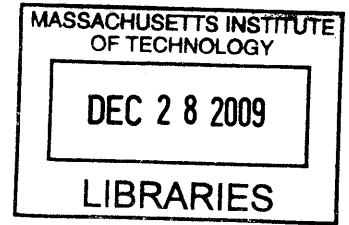# Internal Tide Generation by Tall Ocean Ridges

by

Paula Echeverri Mondragón

B.S., Aerospace Engineering (2004)
S.M., Mechanical Engineering (2006)
Massachusetts Institute of Technology

Submitted to the Department of Mechanical Engineering, MIT
and the Department of Applied Ocean Science and Engineering, WHOI
in partial fulfillment of the requirements of

Doctor of Philosophy in Mechanical and Oceanographic Engineering

at the

MASSACHUSETTS INSTITUTE OF TECHNOLOGY

and the

WOODS HOLE OCEANOGRAPHIC INSTITUTION

September, 2009

Author . . . .

MIT-WHOI Joint Program
August, 2009

Certified by . . . .

Thomas Peacock
Associate Professor of Mechanical Engineering, MIT
Thesis Supervisor

Accepted by . . . .

James Preisig
Associate Scientist, Department of Applied Ocean Science and Engineering, WHOI
Chairman, Joint Committee for Applied Ocean Science and Engineering

Accepted by . . . .

David E. Hardt
Ralph E. and Eloise F. Cross Professor of Mechanical Engineering, MIT
Chairman, Committee on Graduate Students

Internal Tide Generation by Tall Ocean Ridges

by

Paula Echeverri Mondragón

Submitted to the Department of Mechanical Engineering, MIT and the Department of Applied Ocean Science and Engineering, WHOI on August, 2009, in partial fulfillment of the requirements of
Doctor of Philosophy in Mechanical and Oceanographic Engineering

Abstract

Internal tides are internal waves of tidal period generated by tidal currents flowing over submarine topography. Tall ridges that are nominally two-dimensional (2-D) are sites of particularly strong generation. The subsequent dissipation of internal tides contributes to ocean mixing, thereby playing an important role in the circulation of the ocean. Strong internal tides can also evolve into internal wave solitons, which affect acoustic communication, offshore structures and submarine navigation. This thesis addresses the generation of internal tides by tall submarine ridges using a combined analytical and experimental approach.

The first part of the thesis is an experimental investigation of a pre-existing Green function formulation for internal tide generation by a tall symmetric ridge in a uniform density stratification. A modal decomposition technique was developed to characterize the structure of the experimental wave fields generated by 2D model topographies in a specially configured wave tank. The theory accurately predicts the low mode structure of internal tides, and reasonably predicts the conversion rate of internal tides in finite tidal excursion regimes, for which the emergence of non-linearities was notable in the laboratory.

In the second part of the thesis, the Green function method is advanced for asymmetric and multiple ridges in weakly non-uniform stratifications akin to realistic ocean situations. A preliminary investigation in uniform stratification with canonical asymmetric and double ridges reveals asymmetry in the internal tide that can be very sensitive to the geometric configuration. This approach is then used with realistic topography and stratification data to predict the internal tide generated by the ridges at Hawaii and at the Luzon Strait. Despite the assumption of two-dimensionality, there is remarkably good agreement between field data, simulations and the new theory for the magnitude, asymmetry and modal content of the internal tide at these sites.

The final part of the thesis investigates the possibility of internal wave attractors in the valley of double-ridge configurations. A one-dimensional map is developed to identify the existence and stability of attractors as a function of the ridge geometry. The Green function method is further advanced to include a viscous correction to balance energy focusing and dissipation along an attracting orbit of internal wave rays, and very good agreement is obtained between experiment and theory, even in the presence of an attractor.

Thesis Supervisor: Thomas Peacock
Title: Associate Professor of Mechanical Engineering, MIT

Acknowledgments

This work has been fun and rewarding, and I feel privileged to have had such a rich Ph. D. experience. I owe a lot of this to the support, guidance, good temper and enthusiasm of Professor Thomas Peacock, who has that capacity for wonder that makes science a pleasure.

My thesis work provided me with the opportunity for interactions with bright and good spirited people. Working with Professor Morris Flynn on the investigations of chapter 3 was a pleasure, and every issue that came up was approached with honesty and care. Professor Neil Balmforth was a patient guide for the analytical work of chapters 4 and 5, and a good host at Walsh cottage during the summers in Woods Hole. I also collaborated with Professor Kraig Winters, who was kind and clear in our communications, and enjoyed working with Tite Yokossi, who was always excited about work. I also thank Damon Vanderlind for his contribution in the early days of developing the modal decomposition code and Andy Gallant for his expert construction skills.

I have never been lacking for support. My thesis committee were generous with their time and advice. I shared my work with my lab-mates Mani Mathur and Michael Allshouse, and I appreciate their interest and their sense of humor. From Ray Hardin, Leslie Regan, Marsha Gomez and Ronni Schwartz I always had immediate answers and access to any resources I needed. I am in awe of their efficiency and always grateful for their kindness.

I also have a beautiful family in Colombia. They know that my life here has been an adventure, and they too think that this is great. That is the best support I could ever ask for. Apart from my family, the coolest people in my life I met at Number Six. Since they are now spread around the world, *anywhere* is *the* place to go. A few of them have been with me in Boston the last five years, and they are my family here.

Contents

List of Figures

12

13

14

16

17

List of Tables

Nomenclature

b buoyancy field

U tidal current amplitude

ψ stream function

ϕ steady state stream function

f Coriolis frequency

N buoyancy frequency

ω_0 tidal frequency

θ angle of the internal wave group velocity with the horizontal

μ slope parameter

h topography

H ocean depth

ε criticality parameter

χ excursion parameter

X dimensionless horizontal coordinate

Z dimensionless vertical coordinate

G Green function

γ distribution of sources

γ_p modal amplitude

Φ_p modal phase

C barotropic to baroclinic conversion rate

$C_*^{\pm}$ directional dimensionless conversion rate

K numerical resolution

P truncation of Fourier series

α dissipation term

Chapter 1

Introduction

Internal gravity waves propagate in density-stratified media, where the weight and the buoyancy of water masses act as restoring forces, and are ubiquitous in the ocean interior. The waves are generated, for instance, by lunar and solar tidal currents flowing back and forth over ocean-bottom topography. The resulting example internal waves have tidal frequencies and are called internal tides. On the global scale, internal tides are an important component of the ocean's energy budget [62]; and on the local scale, they can give rise to strong perturbations such as nonlinear solitary waves on the ocean thermocline [70], which can transport nutrients [12], affect underwater acoustic communications [23] and interact with offshore structures [71].

The work presented here uses both laboratory experiments and theory to investigate internal tide generation by topography and to apply this understanding to geophysical situations. Specifically, a new experimental wave tank facility has been developed and analytical models of tidal conversion have been advanced to study internal tide generation over tall ocean ridges. The results of these investigations are applied to internal tide generation at the Hawaiian Ridge and at the Luzon Strait between Taiwan and the Philippines.

The introduction presents a general review of internal tides, starting with their relevance to the physical structure of the ocean on a global scale and to ocean dynamics on a regional scale. The basis of the analytical formulation of internal tide generation by topography is then summarized, followed by a review of analytical models and laboratory and numerical experiments that address this problem. A detailed outline of the thesis is given at the end of the chapter.

1.1 Internal tides

The weight and the buoyancy of a mass of water act as competing restoring forces when the fluid is perturbed away from its neutrally buoyant state, and so the stratified ocean is an elastic medium in which internal waves propagate. Internal waves that have the same periods as the forcing tides are called internal tides. These are generated by perturbations to the tidal currents that balance the rise and fall of the water level caused by the tidal forces of the Earth-sun and the Earth-moon orbits. As the earth and the moon rotate, so does the alignment of the tidal forces, such that at a particular location on the surface of the Earth the water level will rise and fall every day or every half a day, and therefore the tidal currents will reverse direction with the corresponding diurnal and semi-diurnal periods, respectively. When unobstructed, tidal currents are barotropic disturbances, meaning that lines of constant density and pressure remain parallel. However, if the currents are forced to flow over topography, then dense deep water will be forced up toward less dense regions. The internal wave field that is generated by this perturbation is a baroclinic flow, whereby pressure gradients exist across constant-density surfaces.

The first scientific record of internal waves was reported by Nansen [63] during the Norwegian polar expedition of the mid-1890's. He reported oscillations in the water column that were not associated with the motion of the ship, as well as the 'dead-water' phenomenon. Internal tides, however, were first described as such by Otto Pettersson [76] (according to Ekman [21]), who studied them in field experiments off the west coast of Sweden over a period of two years. Pettersson noted that differences in temperature and salinity allowed him to identify separate water layers, and that these layers, which moved independent from each other and from the surface wind, oscillated with tidal periods.

It has since become recognized that internal tides are part of important global energy systems: the orbits of the moon around the Earth and the Earth around the sun, and the energy budget of the ocean. For instance, the energy in the moon-Earth system is decreasing, such that every year the moon recedes a few centimeters from the Earth. The dissipation rate has been estimated to be 3.7TW, and about 1TW of this is now attributed to energy conversion from barotropic to internal (baroclinic) tides, as detailed by Munk and Wunsch [62].

Internal tides play a role in the maintenance of the non-homogeneous structure of tem-

perature and salinity (thermo-haline structure) in the ocean interior because they provide a source of mechanical energy for abyssal ocean mixing [62]. A simple one-dimensional (1-D) model suggests that the thermo-haline structure persists despite the upwelling of cold deep water as part of the Meridional Ocean Circulation (MOC) because vertical diffusion due to mixing balances the vertical advection. Almost 50% of the total mixing required to maintain this balance would occur in the abyssal ocean; yet direct mixing by the wind over the ocean surface and friction-driven mechanisms along the ocean floor cannot account for the entirety of this estimate. A strong candidate source for the remaining energy is the internal tide field, which may provide 0.6 to 0.9 TW [62]. This small amount of mechanical mixing would be crucial, for instance, to explain a 2000 TW poleward heat flux. A remaining open question is how the tides dissipate in the open ocean, and whether and how that leads to mixing [41].

Recent observations demonstrate the important role of internal tide generation over topography. Egbert and Ray [20] used TOPEX/Poseidon satellite altimetry data to constrain a tidal model and map the rate of energy lost from the barotropic M2 tide (a strong component of the semi-diurnal lunar tides), as shown in figure 1-1. Most of the 1TW of dissipation in the deep ocean occurs in regions with significant topography; including isolated and tall features, such as the Hawaiian Ridge, and broader regions of rough topography, such as the mid-Atlantic Ridge. For instance, Ray and Mitchum [80] estimate that 15GW propagate away from the Hawaiian Ridge in the first baroclinic vertical mode. The surface displacements from satellite data that led to this estimate are shown in figure 1-2. The tidal dissipation estimated over rough bathymetry also coincides with measurements of enhanced mixing. A notable example is the experiment by Polzin *et al.* [77] in the Brazil Basin, which detected an order of magnitude higher diffusivity over rough topography of the mid-Atlantic Ridge as compared to the flat-bottom regions between the continent and the ridge.

Global and regional simulations confirm what the aforementioned observations suggest, and also highlight the effectiveness of tall and nominally two-dimensional (2-D) ridges as internal wave generators, since water is forced to flow over instead of around such features. Using a global multi-layer numerical model, Simmons *et al.* [82] identified 20 regions of abrupt topography that contribute 75% of the global barotropic to baroclinic conversion. This is the case in Hawaii and in the Luzon Strait, which stand out in figure 1-1 as areas of high generation. Merrifield and Holloway [61] used the Princeton Ocean Model (POM) to
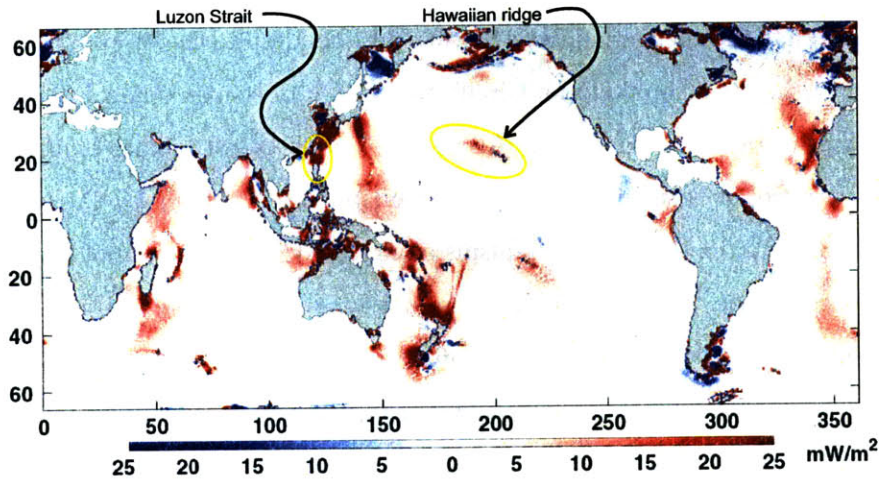
Figure 1-1: Dissipation of the M2 tide per surface area estimated using TOPEX/Poseidon data to constrain barotropic tide equations. Negative dissipation is not physical but illustrates the level of noise in the computation. Reproduced from [20]. The locations of the Hawaiian and Luzon ridges are encircled.
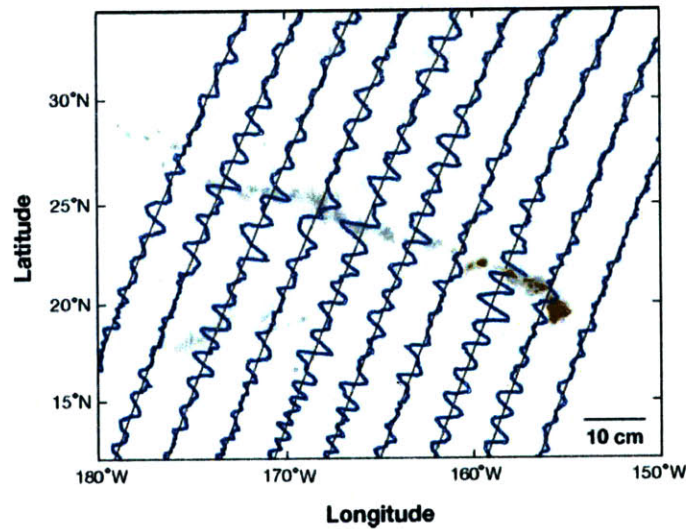
Figure 1-2: Surface displacement at the M2 frequency propagating away from Hawaii measured by the TOPEX/Poseidon. The original figure from [80] was updated and reproduced (as shown here) in [25]).

do a numerical simulation of the barotropic tides over the steep Hawaiian Ridge and found a 9.7GW-energy flux into the M2 internal tide. Niwa and Hibiya [66] did a similar study using POM in the East China Sea, and estimated a 7.4GW-energy flux into the M2 internal tide radiating away from the Luzon Strait. This stands in comparison to the less efficient barotropic to baroclinic conversion over smaller and deeper rough topography. For instance, St. Laurent and Garrett [83] estimate conversion rates of $O(10^{-3})\mathrm{W/m}^2$ throughout the mid-Atlantic Ridge, as compared to conversion rates of $O(1)\mathrm{W/m}^2$ estimated over topography in Hawaii by Merrifield and Holloway [61].

Mixing can occur where internal tides dissipate, even in the ocean, and therefore internal tide propagation away from generation sites and its subsequent dissipation are important open questions. Garrett and Kunze [25] review numerical and observational studies that show that low vertical modes, associated with large vertical scales of the order of the ocean depth, propagate far; while high modes with vertical scales much shorter than the ocean depth are more vulnerable to shear and buoyancy instabilities, leading to eventual wave breaking and dissipation. It is widely believed that most of the energy converted into the internal tide travels away in the form of low modes, so a large fraction of the baroclinic energy dissipates far from its generation site, as discussed by St. Laurent and Garrett [83]. This varies at different generation sites: Jan *et al.* [42] find that more baroclinic energy is dissipated locally at the Luzon Strait (18 GW) than radiated in the internal tide (12 GW), and report that this ratio is 5 times larger than the corresponding ratio for Hawaii. Several mechanisms can extract energy from the far-propagating low modes. Examples include internal wave reflections off supercritical slopes (Kunze and Llewellyn Smith [48]), scattering off far-field topography (Johnston and Merrifield [43]), wave-wave interactions, such as the parametric sub-harmonic instability (described by Young *et al.* [88] and explored numerically by MacKinnon and Winters [58]), and wave field interactions with the mean flow (Grimshaw [30], St. Laurent and Garrett [83]).

It is also important to understand strong internal tides before they dissipate, as they affect the local state and dynamics of the regions in which they propagate. In particular, strong internal tides can evolve into nonlinear internal solitary waves, which are large amplitude and high-frequency baroclinic perturbations for which non-linearity and dispersion effects balance, such that an internal wave soliton can persist for long distances. Analytical models of internal wave solitons are reviewed by Helfrich and Melville [36]. Strong solitons

27

produce a visible manifestation at the ocean surface that consist of propagating strips in which the sea surface is alternatingly rough and smooth, generated by diverging and converging surface currents associated with the internal waves. These signatures have been observed passing by ships and arriving on shore since at least the 1920's (as reported by Apel *et al.* [3]), and, more recently, in aircraft and satellite images. An early comprehensive field experiment by Apel *et al.* [3] was performed in 1980 in the Sulu Sea using moored oceanographic stations, ship casts and observations from space. They identified nonlinear solitons with approximately 100 m amplitudes, 20 km wave lengths and over 100 km crest lengths, propagating with periods of about 1 hour into the Sulu sea from the topography at the southeastern side. The speed and wavelength of the internal waves satisfied the finite-depth, solitary wave evolution theory of Joseph [44].

Some of the largest nonlinear internal waves in the world are found in the South China Sea, attesting to the strength of the internal tide radiating from the tall topography at the Luzon Strait. Figure 1-3 shows three nonlinear internal wave packets in a synthetic aperture radar (SAR) satellite image of the region. Several studies have analyzed the propagation of these solitons using data collected during the Asian Seas International Acoustics Experiment (ASIAEX) in 2001. For example Ramp *et al.* [79] trace soliton observations back to a region between the Batanes Islands, Liu *et al.* [53] use data from SAR images as initial conditions in a soliton propagation model, obtaining good agreement with mooring measurements downstream, and Duda *et al.* [16] describe the behavior of solitons as these encounter the Chinese shelf break. Zhao and Alford [90] use ASIAEX data to argue that the solitons evolve from non-linear steepening of strong internal tides.

Nonlinear internal waves create large amplitude perturbations of the environmental conditions. A good example is in the South China Sea, where vertical currents of up to $O(0.5)$ m/s and vertical displacements of the water column of $O(100)$ m are observed. Nonlinear internal waves interact with and affect many engineered systems, such as offshore structures (motivating the work of Osborne *et al.* [71] and Osborne and Burch [70]), acoustic communications and submarine navigation. For instance, submarines often travel along the thermocline, which is a region, usually tens to hundreds of meters deep, where the temperature and density change rapidly between a relatively well mixed top layer and the strongly stratified deep ocean. Because of the rapid change in acoustic propagation properties, sound waves reflect off the thermocline, so submarines can travel along an effectively
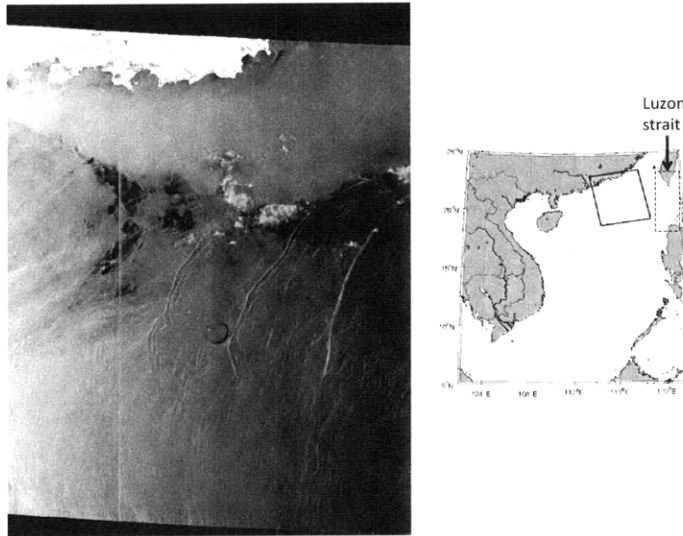
Figure 1-3: RADARSAT-1 ScanSAR image (left) taken on April 26th, 1996, of the area enclosed by the solid line in the map of the South China Sea (right). The dashed line indicates the location of the Luzon Strait. Both figures are reproduced from [28].

'quiet zone' below the thermocline to minimize the risk of being detected by sonar. However, navigation in this region is also particularly difficult, as the thermocline coincides with the largest amplitudes of internal solitary waves because of the strong stratification, and submarines must compensate for passing waves. Submarine accidents have been attributed to the presence of internal waves on the thermocline. Such was the fate of a Russian submarine that entered the Mediterranean through the Strait of Gibraltar, which is a region where the surface manifestation of solitons is often seen. The submarine was traveling in the quiet zone, hiding in the wake of a tanker, when a cold temperature front associated with an internal wave caused it to rise and collide with the tanker [1].

Having reviewed the significance of internal tides, the next section presents the equations that govern their generation and dynamics.

1.2 Analytical formulation

1.2.1 Governing equations

The following form of the Navier-Stokes equation, which governs the flow velocity $\mathbf{u} = \mathbf{u}(\mathbf{r}, t)$, pressure $p(\mathbf{r}, t)$ and density $\rho(\mathbf{r}, t)$ in a rotating frame, is a general description of incompressible and adiabatic fluid motion in the ocean:

$$\frac{D\mathbf{u}}{Dt} + 2\mathbf{\Omega} \times \mathbf{u} + \frac{\nabla p}{\rho} + \mathbf{g} = \mathbf{F}. \tag{1.2.1}$$

Here, $\mathbf{r}$ is a position vector, $\mathbf{\Omega}$ is the angular velocity of the Earth ($|\mathbf{\Omega}| = 7.29 \times 10^{-5}$ rad/s), $\mathbf{g} = -g\hat{k} = -9.81$ m/s^2 is the gravitational acceleration and $\hat{k}$ is an upward vertical unit vector. Any external forcing on the flow is represented by $\mathbf{F} = \mathbf{F}(\mathbf{r}, t)$. Viscosity and diffusion are not included at this point in equation 1.2.1. The viscous term is usually neglected for high Reynolds number flows such as internal wave motion in the ocean, where $Re = UL/\nu = O(10^7)$, although this decision is revisited in the discussions of experimental wave fields in chapters 3 and 5, as Reynolds numbers are much lower in a laboratory setting. Diffusion is neglected throughout the thesis as it does not play a significant role in the internal tide generation problem. On the other hand, diffusion would be an important mechanism to account for in investigating the important problem of internal tide dissipation. The thermodynamic energy equation for an adiabatic and incompressible fluid is

$$\frac{D\rho}{Dt} = \rho_t + \mathbf{u} \cdot \nabla \rho = 0, \tag{1.2.2}$$

and the continuity equation, which is derived from the conservation of mass and the density equation (1.2.2), is

$$\nabla \cdot \mathbf{u} = \mathbf{0}. \tag{1.2.3}$$

Equations (1.2.1) through (1.2.3) can be linearized for small perturbations about a background state. The linear problem of 2-D internal tide generation by topography, shown schematically in figure 1-4, is formulated about a stably stratified ocean and a 2-D barotropic tidal current flowing over 2-D topography. The y-axis is defined along the crest of a 2-D ridge $h(x)$, such that $\partial h/\partial y = 0$. Therefore, all the field variables vary in space only across

the ridge (in x) and with depth (in z). The total velocity field can be expressed as

$$\mathbf{u}(x, z, t) = (U \cos \omega_0 t, V(t), 0) + \mathbf{u}'(x, z, t), \qquad (1.2.4)$$

where U is the far-field, constant tidal amplitude, ω_0 is the tidal frequency, and the prime indicates a small perturbation variable. The y-component of the barotropic tide $V(t)$, which is aligned with the crest of the ridge, arises to balance the barotropic forcing $\mathbf{F}(t) = F\hat{i}$ in the presence of background rotation. The external forcing can be found by substituting $\mathbf{u} = U \cos \omega_0 t \hat{i} + V(t)\hat{j}$, where $\hat{i}$ and $\hat{j}$ are unit vectors in the x and y directions, respectively, into the momentum equation (1.2.1). In the absence of additional horizontal pressure gradients or perturbations, and assuming that the background rotation is aligned with the vertical, where $2\Omega = (0, 0, f)$, the barotropic forcing F is found from the $x-$component of the momentum equation (1.2.1):

$$-\omega_0 U \sin \omega_0 t - fV(t) = F. \qquad (1.2.5)$$

The velocity along the ridge, $V(t)$, can be found by integrating the $y-$component of (1.2.1):

$$\frac{dV}{dt} + fU \cos \omega_0 t = 0, \qquad (1.2.6)$$

such that

$$V = -\frac{fU}{\omega_0} \sin \omega_0 t + C. \qquad (1.2.7)$$

Substituting equation (1.2.7) into (1.2.5) yields

$$F = \left(\frac{f^2 - \omega_0^2}{\omega_0} \right) U \sin \omega_0 t. \qquad (1.2.8)$$

The total density is

$$\rho(x, z, t) = \rho_0(z) + \rho'(x, z, t), \qquad (1.2.9)$$

and can be expressed in terms of the buoyancy frequency $N(z)$, which is defined as

$$N^2(z) \equiv -\frac{g}{\rho_0(z)} \frac{\partial \rho_0}{\partial z}(z), \qquad (1.2.10)$$

31
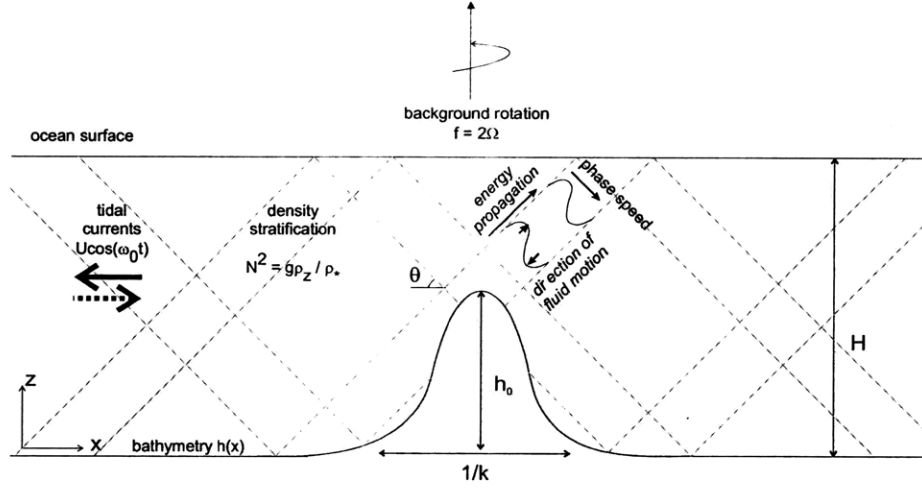
Figure 1-4: Schematic illustrating the linear problem of 2-D internal tide generation by topography. A 2-D tidal current, $U \cos \omega_0 t$, flows over topography $h(x)$ with maximum height h_0 and horizontal wave number k. The ocean depth is H, the ocean stratification is characterized by the buoyancy frequency profile $N(z)$, and the background rotation of the earth is 2Ω. Internal wave beams propagate away from the topography at an angle θ with respect to the horizontal.

plus a perturbation term. The Boussinesq approximation holds if the absolute change in density is small, such that $\Delta \rho / \rho_0(z) \ll 1$. This is the case for internal tides in the ocean, where

$$\frac{\Delta \rho}{\rho_0(z)} = O(N^2 H/g) = O(10^{-4}), \tag{1.2.11}$$

taking $H = O(1000)$m to be the typical vertical scale of a tall ridge and $N = O(10^{-3})$rad/s. Therefore, $\rho_0(z) \approx \rho_*$, where ρ_* is a reference background density value at z_*, and the buoyancy frequency is

$$N^2(z) \approx -\frac{g}{\rho_*} \frac{\partial \rho_0(z)}{\partial z}. \tag{1.2.12}$$

In the Boussinesq limit, the total density in (1.2.9) can be expressed as

$$\rho(x, z, t) = \frac{\rho_*}{g} \left[g + \int_z^{z_*} N^2(z')dz' + b \right], \tag{1.2.13}$$

where $b = \rho' g / \rho_*$ is the buoyancy field that arises from perturbations to the background density stratification. The buoyancy field can be interpreted as the force per unit mass acting on fluid that has been displaced from its neutrally buoyant state.

32

Finally, the total pressure is

$$p(x, z, t) = p_0(z) + p'(x, z, t). \tag{1.2.14}$$

Setting $mathbfF \cdot \hat{k} = 0$, $w = 0$ and $\rho' = 0$ in the vertical momentum equation (1.2.1) yields an expression for the hydrostatic pressure:

$$p_0(z) = -g \int_H^z \rho_0(z')dz', \tag{1.2.15}$$

so equation (1.2.14) becomes

$$p(x, z, t) = -g \int_H^z \rho_0(z')dz' + p'(x, z, t). \tag{1.2.16}$$

The equations of motion (1.2.1) through (1.2.3) are linearized by substituting equations (1.2.4), (1.2.12), (1.2.13) and (1.2.16) and neglecting the products of small quantities. We assume that the tidal excursion (U/ω_0) is small compared to the characteristic width of the topographic feature $(1/k)$, such that the excursion parameter $\chi = Uk/\omega_0 \ll 1$. Therefore, in the total derivative $(D/Dt = \partial/\partial t + \mathbf{u} \cdot \nabla)$ of the horizontal momentum equation (1.2.1), both parts of the advective term are small compared to the partial time derivative:

$$u \cdot \nabla u = (U + u') \cdot \nabla u \ll u_t. \tag{1.2.17}$$

The linearized equations governing the perturbations are, therefore,

$$\mathbf{u}_t + 2\Omega \times \mathbf{u} + \frac{\nabla p}{\rho_*} - b\hat{k} = 0 \tag{1.2.18}$$

$$b_t + wN^2 = 0, \tag{1.2.19}$$

and

$$\nabla \cdot \mathbf{u} = 0; \tag{1.2.20}$$

where the variables denote perturbation quantities and the primes have been dropped. Note that b has replaced the last term in the left hand-side of the momentum equation (1.2.18), and it acts as a restoring force responsible for internal waves in density-stratified flows. It is also the only term in which the density perturbation has a first order effect that cannot

33

be neglected.

The curvature of the Earth is small in the spatial domain of internal waves, which means that the β-plane approximation holds and that equations (1.2.18) through (1.2.20), which are exact in curvilinear coordinates, are approximately valid in cartesian coordinates. In particular, the following assumptions, which are required to use the β-plane approximation (as reviewed in LeBlond and Mysak [50]), are satisfied: the horizontal domain of the flow $L = O(10^5)$m is less than the radius of the earth $R = 6.4 \times 10^6$m, so

$$\left(\frac{L}{R}\right)^2 = O(10^{-2}) \ll 1; \qquad (1.2.21)$$

the ocean is a thin layer of fluid $H = O(10^3)$m around the Earth, so

$$\frac{H}{R} = O(10^{-3}) \ll 1; \qquad (1.2.22)$$

and the flow takes place at low enough latitudes $\phi_0 < 45°$, so

$$\frac{L \tan \phi_0}{R} = O(10^{-2}) \ll 1. \qquad (1.2.23)$$

The f-plane approximation, which builds upon the β-plane, is used throughout this thesis. The Coriolis term in the momentum equation (1.2.18) can be simplified (as has been done previously in this discussion) via the f-plane approximation [50]. From the β-plane approximation, the rotation of the Earth near a given latitude ϕ_0 is

$$\mathbf{\Omega} = (0, \Omega \cos \phi, \Omega \sin \phi) \approx (0, \tilde{f}/2, f/2 + \beta y), \qquad (1.2.24)$$

where $f = 2\Omega \sin \phi_0$, $\tilde{f} = 2\Omega \cos \phi_0$, $\beta = 2 \cos \phi_0 / R$ and the approximate y-coordinate aligned with the meridians is $y = R(\phi - \phi_0)$. As long as $O(\beta y/f) = L/R \ll 1$, the vertical component of $\mathbf{\Omega}$ is approximately f. Furthermore, the meridional component $\tilde{f}$ can be neglected because the vertical velocity perturbation w, which scales $\tilde{f}$ in the cross-product of equation (1.2.18), is relatively small. In particular, $O(\tilde{f}w \ll fv) = H/\tan \phi_0 L \ll 1$.

Finally, the inviscid, linearized 2-D Boussinesq equations of motion in the f-plane that

govern perturbations to the barotropic flow are:

$$u_t - fv + \frac{p_x}{\rho_*} = 0, \tag{1.2.25}$$

$$v_t + fu = 0, \tag{1.2.26}$$

$$w_t - b + \frac{p_z}{\rho_*} = 0, \tag{1.2.27}$$

$$b_t + N^2 w = 0, \tag{1.2.28}$$

and

$$u_x + w_z = 0. \tag{1.2.29}$$

These can be combined into a single equation by defining a stream function ψ such that $(u, w) = (-\psi_z, \psi_x)$, which immediately satisfies the continuity equation (1.2.29). The substitution yields:

$$\left(N^2 + \frac{\partial^2}{\partial t^2}\right)\psi_{xx} + \left(f^2 + \frac{\partial^2}{\partial t^2}\right)\psi_{zz} = 0. \tag{1.2.30}$$

The dispersion relation, which specifies the angle θ of the internal wave group velocity with respect to the horizontal, is obtained by substituting a propagating plane wave of the form $\psi = \psi_0 \exp\left[\mathbf{k} \cdot \mathbf{x} - i\omega_0 t\right]$ into equation (1.2.30), giving

$$\tan\theta = \sqrt{\frac{\omega_0^2 - f^2}{N^2 - \omega_0^2}}. \tag{1.2.31}$$

Equation (1.2.31) is valid for uniform stratifications and when the WKB scaling is used, as discussed in chapter 4.

An internal tide is a solution of the internal wave equation (1.2.30) with the same periodic time dependence as the forcing barotropic tide:

$$\psi(x, z, t) = U\Re\left\{\phi(x, z)e^{-i\omega_0 t}\right\}, \tag{1.2.32}$$

where $\Re$ denotes the real part of the argument. The governing equation used throughout this work is a single, linear partial differential equation for $\phi(x, z)$ and comes from substituting $\psi(x, z, t)$ from (1.2.32) into equation (1.2.30), giving

$$\left(N^2 - \omega_0^2\right)\phi_{xx}(x, z) - \left(\omega_0^2 - f^2\right)\phi_{zz}(x, z) = 0. \tag{1.2.33}$$

35

1.2.2   Boundary conditions

For internal tide generation by topography, the flow is required to satisfy the inviscid, no-normal flow boundary condition at the topography and at the free surface (the latter is referred to as the 'rigid-lid' condition). At the topography, the condition is that the component across the topography of the total velocity from (1.2.4) is zero:

$$\left[U \cos\omega_0 t \hat{\imath} - \frac{fU}{\omega_0} \sin\omega_0 t \hat{\jmath} + \mathbf{u}(x, h(x), t) \right] \cdot \mathbf{n} = 0, \tag{1.2.34}$$

where $\mathbf{n} = -h'(x)\hat{\imath} + \hat{k}$ is a vector normal to the topography. This requires that the streamlines of the flow must follow the shape of the topography, which is satisfied for

$$\psi(x, h(x), t) = Uh(x) \cos\omega_0 t, \tag{1.2.35}$$

which reduces to

$$\phi(x, h(x)) = h(x). \tag{1.2.36}$$

At the free surface in an ocean with far-field depth H, we can assume that there is no vertical motion

$$\phi(x, H) = 0. \tag{1.2.37}$$

Finally, the internal wave field must satisfy the radiation condition, which dictates that the waves propagate away from the topography. The application of the radiation condition is discussed as it is used in chapters 3 and 4.

Often, the propagating internal wave field in the ocean is described in terms of vertical modes. This derives from the solution to equation (1.2.33) away from topography in an ocean of constant depth. Here, the ocean can be reasonably modeled as a vertical channel with flat top and bottom boundaries, such that

$$\phi(x, 0) = \phi(x, H) = 0. \tag{1.2.38}$$

In this case, the solution to equation (1.2.33) has a separable form $\phi(x, z) = \mathcal{F}(x)\mathcal{H}(z)$. Substituting this form into (1.2.33) and looking to satisfy the condition in (1.2.38) yields a Sturm-Liouville problem for the vertical structure, which is therefore characterized by

parameter	symbol	dimensions
ocean depth	H	L
topographic height	h_0	L
topographic horizontal wave number	k	1/L
tidal current amplitude	U	L/T
tidal frequency	ω_0	1/T
buoyancy frequency	N	1/T
coriolis frequency	f	1/T

Table 1.1: Dimensional parameters.

discrete vertical modes:

$$\mathcal{H}(z) = \sum_{p=1}^{\infty} a_p(z). \qquad (1.2.39)$$

The eigenfunctions $a_p(z)$ are orthogonal over the domain, such that

$$\int_0^H w(z) a_p(z) a_q(z) dz = 0, \qquad (1.2.40)$$

for some weight function $w(z)$ and for $p \neq q$. In particular, for a uniformly stratified ocean with $N \neq N(z)$, the vertical modes are sines and cosines. The modal structure of the far-field internal tide, which is important, for instance, because the low modes carry the majority of the baroclinic energy, emerges in the solutions discussed in chapters 3 and 4, and is discussed there in more detail.

1.2.3 Parameter regimes

Figure 1-4 introduces physical parameters that characterize internal tide generation in space (L) and time (T). The buoyancy and Coriolis frequencies, N and f respectively, characterize the medium in which internal waves travel; the ocean depth H and the topographic height h_0 and width $1/k$ characterize the boundary conditions; and the amplitude U and frequency ω_0 of the barotropic tidal current characterize the forcing. These parameters and their corresponding dimensions are summarized in table 1.1.

The Buckingham-Pi theorem states that a problem that involves $n = 7$ physical parameters expressible in $m = 2$ fundamental physical quantities (L and T) can be fully defined using $n - m = 5$ independent non-dimensional parameters. The following five independent non-dimensional parameters, summarized in table 1.2, have relevant physical meanings and

37

parameter	symbol	formula
criticality	ε	$h'_{max}/\tan\theta$
excursion	χ	kU/ω_0
depth ratio	h_0/H	h_0/H
horizontal Froude number	Fr_x	Uk/N
vertical Froude number	Fr_z	U/Nh_0

Table 1.2: Non-dimensional parameters.

describe different parameter regimes that have been investigated previously, as summarized by Garrett and Kunze [25].

The criticality ε is the ratio of the slope of the topography to the local slope of internal wave rays. Usually in internal tide generation problems, the maximum value of this ratio is used to define the criticality of the configuration as a whole. In the case of generation by supercritical topographies, with $\varepsilon > 1$, the propagation of internal waves is unobstructed in both the up- and downward directions, which is the case illustrated in figure 1-4. When the topography is subcritical, with $\varepsilon < 1$, the waves only propagate in the upward direction. For example, at some locations the Keana Ridge is supercritical (Nash *et al.* [64]), while a majority of the topography of the east-Pacific rise is subcritical (St. Laurent and Garrett [83]).

The excursion parameter χ is the ratio of the tidal excursion to the horizontal extent of the topography. In equation (1.2.17), the excursion χ is assumed to be small in order to simplify the governing equations by eliminating the nonlinear advective terms. Note, however, that it is possible to keep the advective term and still obtain linear equations, as in the theory of Bell [10] that will be discussed in section 1.3. In that case, the more general form of the dispersion relation (1.2.31) for internal waves is

$$\tan\theta = \left(\frac{\omega^2 - f^2}{N^2 - \omega_0^2}\right)^{1/2}, \tag{1.2.41}$$

where the wave frequency $\omega \to \omega_0$ if the excursion parameter is small and the internal waves are internal tides; or $\omega \to Uk$ if the excursion parameter is large and the waves are so-called lee-waves.

The depth ratio h_0/H is the ratio of the maximum height of the topography to the far-field depth of the ocean. When the depth ratio is $O(1)$, it is closely related to the

modal structure of internal tides: small depth ratios are associated with more energetic high vertical modes, whereas large depth ratios are associated with energetic low modes. Furthermore, in the case of 2-D internal tide generation, a large depth ratio has an important effect because, by conservation of mass, it dictates the acceleration of the flow over the top of the topography. For very small depth ratios $h_0/H \ll 1$, the problem can be approximated as internal tide generation in a semi-infinitely deep domain, and the internal tide can be accurately and more conveniently described as internal wave beams propagating away from topography, as opposed to as a sum of vertical modes.

The horizontal Froude number Fr_x is the ratio of the velocity of the background flow (in this case U) to the internal wave speed (which is proportional to k/N). Here, Fr_x determines the extent to which internal tides are advected by the barotropic tide. Hibiya [37] described a mechanism by which periods of trans-critical flow (with $Fr_x \approx 1$) allow for constructive interference of elementary waves that radiate away from an obstacle. The steepening leads to solitary waves of the sort that were observed experimentally by Maxworthy [60]. The studies of the following chapters are concerned with subcritical flow in the sense that $Fr_x < 1$.

The vertical Froude number Fr_z compares inertia to buoyancy forces. Due to the stratification, the flow resists being forced to a different depth, and therefore, if the buoyancy forces are strong and $Fr_z < 1$, the flow has the tendency to remain attached on the lee-side of a ridge. On the other hand, if $Fr_z > 1$, then the inertia of rapid flow over topography may overcome buoyancy such that lee-side flow separation occurs. Different separation regimes depending on Fr_z are summarized in figure 5.8 of Baines [5]. The studies in the following chapters are concerned with regimes in which no flow separation occurs.

1.3 Internal tide models

Early solutions to the linear problem of internal tide generation over topography use ray-tracing methods. The solution of Baines [4], for example, is specified along the characteristics determined by the internal wave dispersion relation, which trace the propagation of the internal wave rays in some prescribed spatial domain. This solution is applicable to arbitrary subcritical topography and allows for varying stratification, but the method is difficult to apply and to generalize. Bell [10] presented a different approach using Fourier transforms, which is easily applied to any topography that is very subcritical ($\varepsilon \ll 1$) in

an infinitely deep ocean. These conditions must be satisfied to use the weak topography approximation (WTA), by which the bottom boundary condition is applied at $z = 0$. The linearized boundary condition and a version of the internal wave equation (1.2.33) that includes the linear advective term can be Fourier-transformed and readily solved. Ultimately, this provides an expression for the baroclinic vertical energy flux as an integral function of the Fourier transform of the topography.

The approach of Bell has been applied to case studies of internal tide generation by topography, most notably by St. Laurent and Garrett [83]. They evaluated the Fourier transform of deep subcritical topography at the Atlantic and Pacific mid-ocean ridges, which was available from the RIDGE Multibeam Synthesis Project, and applied a modified version of Bell's solution to estimate $3 - 5\mathrm{mW/m^2}$ of internal tide generation at the mid-Atlantic Ridge. The authors introduced corrections to address the infinite depth and subcritical topography assumptions. Since there is an upper bound on the size of the vertical modes in a finite depth channel, St. Laurent and Garrett truncated the lower limit of the integral in Bell's solution at an adequate low wave number. They then used perturbation theory to investigate the effect of finite amplitude subcritical slopes. For topography that is characteristic of the mid-Atlantic Ridge, St. Laurent and Garrett found that the linear theory does not predict local instabilities or other mechanisms that may lead to dissipation, such that the linear internal tide energy radiates away from its generation site in the low vertical modes.

Bell's solution was formally extended for an ocean of finite depth by Llewellyn Smith and Young [54] and by Khatiwala [45]. Llewellyn Smith and Young define an eigenvalue problem with vertical mode solutions that satisfy homogeneous top and bottom boundary conditions, and express the wave field as a weighted sum of these vertical modes. Projecting the governing equations onto these vertical modes reduces the problem to a Klein-Gordon equation with a Green function solution, which simplifies to a function of the Fourier transform of the topography. This approach also provides an approximate solution for weakly non-uniform stratifications using the WKB approximation to find the shape of the relevant vertical modes. Llewellyn Smith and Young found that the infinite-depth estimate over-predicts internal tide conversion in a finite-depth ocean. Khatiwala solved the problem using Fourier transforms in the frame of reference moving with the background flow, and applied Bell's linearized condition on the bottom boundary and a rigid-lid condition on the

top boundary. The solution includes an integral with singularities, which was solved using contour integration. This theory compared well with numerical simulations using the MIT General Circulation Model (GCM). This approach also showed that infinite-depth theory over-predicts barotropic to baroclinic conversion, and more so for topography that is tall compared to the ocean depth; and that the WTA theory under-predicts conversion for finite amplitude topography, for example as much as 20% for a Gaussian bump with critical slopes.

The WTA is not representative of important sites of internal tide generation, so further studies sought to avoid making this assumption. Assuming an infinitely deep ocean, Balmforth, Ierley and Young [6] developed a solution for generation by up-to critical topographies ($\varepsilon < 1$) by assuming a periodic bottom topography and thus simplifying the boundary condition. They found that the conversion rate for $\varepsilon \sim 0.95$ is enhanced $O(10)\%$ above the prediction of Bell's solution, and that near criticality the wave field develops small scale features and local overturns. Balmforth, Ierley and Young's solutions were compared to laboratory experiments by Peacock *et al.* [73] that are also reported in Echeverri [17]. Peacock *et al.* [73] also successfully compared experiments for a knife-edge ridge in a very deep ocean with the solution of Hurley and Keady [40] for waves generated by an oscillating ellipse, which, in the limit where the width of the ellipse goes to zero, models a knife-edge. The solution of Hurley and Keady was also compared to experiments by Zhang *et al.* [89].

The solution for a knife-edge was further generalized for an ocean of finite depth by St. Laurent *et al.* [85] and by Llewellyn Smith and Young [55]. The former solve the problem of generation at abrupt topography by matching conditions at either side of depth discontinuities, and find that a top hat is a more efficient internal tide generator than a knife-edge, and that modeling topography as a series of discrete steps does not give an accurate estimate of the radiated internal tide. Llewellyn Smith and Young used the Green function solution of Robinson [81], who studied internal wave scattering by a vertical barrier, to model internal tide generation by a knife-edge topography in finite depth. They also provide a WKB approximate solution for generation in weakly non-uniform stratifications. The conversion rates that they evaluate for a knife-edge with parameters that are representative of the ridge at Hawaii are of the same order of magnitude as numerical estimates and estimates based on observations in Hawaii. The important parameters affecting internal tide generation over a knife edge are the gap between the top of the topography and the 'rigid-

lid' surface, and the value of the density gradient at the depth of the top of the topography. Using the same Green function solution, Pétrélis et al. [75] modeled generation by symmetric topographies with monotonic but arbitrarily steep slopes in channels of arbitrary depth and uniform stratification. The experimental investigation presented in chapter 3 of this thesis is concerned with the generation scenario of Pétrélis et al.'s solution, and includes comparisons of laboratory and numerical wave fields to the solution of Pétrélis et al. The results have also been published in Echeverri et al. [18].

Nycander [68] and Balmforth and Peacock [7], who also use a Green function approach, solve for an array of knife edges and periodic topography of arbitrary steepness, respectively, in an infinitely deep ocean. Their work highlights the effects of scattering and interference with the internal tides generated at neighboring ridges on the radiated energy flux and on the structure of the radiated internal tide. Nycander [68] finds that the energy flux of each wall in a periodic array is only equivalent to that of an isolated wall when the height of the walls in the array is small with respect to the distance between neighboring walls. Similarly, Balmforth and Peacock [7] find that the energy flux is not only a function of ε, but also of the ratio of the obstacle height to the separation between obstacles, which affects the nature of the interference between internal tides generated at neighboring ridges.

Overall, the aforementioned analytical models cover broad regimes of criticalities and depth ratios, however, there remain open questions to address in applying these models to internal tide generation by real topography in the ocean. The models presented above consider idealized topographies, whereas the topographic features found in regions of strong internal tide generation can be very intricate. For instance, at the Luzon Strait there is an asymmetric double ridge which, according to estimates by Niwa and Hibiya [66], generates asymmetric internal tides. Previous studies suggest that asymmetric topography can lead to asymmetry in internal tide generation, for example Griffiths and Grimshaw [29] consider generation at continental shelves and show notable differences in the shoreward and ocean-ward internal tides. The asymmetry of internal tide generation at the Luzon Strait cannot be investigated using most of the models described above, with the possible exception of the method of Griffiths and Grimshaw [29]. To this date and to our knowledge, no analytical model has been applied to internal tide generation by realistic ridge topographies. Furthermore, it is not clear when the linear models break down for intermediate excursion parameters. An objective of the following investigation is to assess the validity of existing

models, and to extend their application to more general topographies and ultimately to realistic internal wave generation scenarios in the Hawaiian and the Luzon ridges.

1.4 Thesis overview

Following this introduction, chapter 2 describes the experimental facilities and methods for generating and measuring internal tides in the laboratory. The experimental facilities were designed and set-up for the experimental investigations described in subsequent chapters. The waves were generated in a large tank by oscillating foam models of topographic features in salt-water density stratifications. The experimental method used was particle image velocimetry (PIV).

Chapter 3 reports the results of an experimental investigation of internal tides generated by an isolated and tall topography in finite depth and uniform stratification. The relevant analytical model of Pétrélis et al. [75] is reviewed and a method for extracting the modal structure of experimental wave fields is developed and implemented. Results for small and intermediate excursion parameters are presented for laboratory experiments and numerical simulations, and the modal decomposition of the resulting wave fields is compared to the analytical wave fields. Experiments and numerics are used to assess the validity of the linear theory in the presence of emerging nonlinearities.

Chapter 4 develops an analytical approach to complex topography, such as asymmetric and multiple ridges, in non-uniform stratifications via the WKB approximation. The model is first used to analyze the internal tide generated by different canonical topographic configurations in uniform stratifications, noting that wave fields generated in non-uniform stratifications can be related to wave fields generated in uniform stratifications by topographic shapes that have been scaled according to the WKB coordinate. The model is then applied to realistic geophysical situations, focusing on the Hawaiian and Luzon ridges.

As part of the investigation of internal waves generated by double ridges, the possibility of attractive internal wave limit cycles in the valley of a double ridge is recognized. Chapter 5 presents an investigation of internal wave attractors for double ridges. A one-dimensional return map is developed to identify the existence of internal wave attractors and the analytical method of chapter 4 is modified for such configurations. As an example, a laboratory experiment in which an internal wave attractor exists is presented.

Finally, chapter 6 is a discussion of the conclusions and the contributions of this work.

Chapter 2

Experimental facilities

This chapter describes the experimental set-up and techniques used in the investigations of internal tide generation by topography reported in the following chapters. Foam cut-outs representing idealized oceanic ridges were submerged up-side down in a tank filled with density-stratified salt-water, and oscillated side-to-side in the plane perpendicular to gravity to mimic the relative flow of the barotropic tide. The wave fields generated were measured using particle image velocimetry (PIV).

Section 2.1 describes the apparatus and the procedures used to generate internal wave fields over 2-D ridges. This includes a description of the experimental tank, the procedure to fill the tank with any desired density stratification profile, and a description of the model topography and the system used to oscillate the topography with prescribed motion. Section 2.2 describes the particle image velocimetry (PIV) system that was used to measure the experimental internal wave fields.

2.1 Wave generation

2.1.1 Wave tank

A large glass wave tank was designed and constructed according to the schematic shown in figure 2-1(a). The capacity of the tank is 5.45 ± 0.01 m-long, 0.55 ± 0.01 m-wide and 0.615 ± 0.005 m-tall, which is comparable to the tank in the laboratory of Professor Greg Ivey in the University of Western Australia [39]. The tank is suspended 0.912 ± 0.005 m above the ground, cradled in a frame of 8020 aluminum beams, which is useful for mounting other

apparatus for the experiments. The vertical walls and the bottom walls are clear glass; the front and back walls are 0.5 in-thick and the end and bottom walls are 0.75 in-thick. There is, therefore, open access to the tank from the top and optical access from the bottom and from all sides. There are four foam-covered 1.27 cm-diameter inlets located 3.81 cm above the base of the left end-wall, which are used for filling. The incoming flow, which is controlled by a single two-way valve, is distributed over these four inlets to reduce the momentum of the fluid, thereby significantly reducing mixing of the stratification as the tank fills. There is an outlet with a valve on the bottom wall for emptying the tank after experiments.

Two 800 l reservoirs sit underneath the two ends of the tank and are used to store fresh and salt-water during the filling process, which is done via the double-bucket technique of Oster [72] that is explained in detail in section 2.1.2. Each reservoir is equipped with a re-circulating pump to maintain the water inside at a homogeneous density at any one point in time. The right reservoir, which is used to store very salty water, has a single outlet with a two-way valve from which the salt-water is extracted to be transferred to the second reservoir on the left. Inside the left reservoir, fresh water is continuously being mixed with salt-water, and this mixed water is simultaneously transferred to the experimental tank. The left reservoir has one inlet with a three-way valve, from which the salt-water comes in, and one outlet with a two-way valve that is connected directly to the inlet of the experimental tank. The additional access on the three-way valve is used as needed to extract water from the reservoir.

For the experiments reported in chapter 3, internal wave reflections from the end-walls of the tank were damped using Blocksom filter material, a coarse matting used in fish-tank applications, which has been shown to damp internal waves of the scales that are typical to the laboratory. For example, figure 2-2 (reproduced here from [17]) shows a snapshot of the perturbation to the buoyancy frequency ΔN^2, which is measured directly using synthetic Schlieren [14], for an experiment in which an internal wave beam is generated at the bottom right corner of the image. The amplitude of the ~ 10 cm-wide internal wave beam is reduced by 70% as it reflects off a 2 cm-wide layer of Blocksom matting. In the experiments of chapter 3, the end-walls were lined with an approximately 10 cm-thick layer of matting, and the last 50 cm of the bottom wall and the free surface at either end were lined with approximately 4 cm-thick layers of matting. The damping provided was observed to be sufficient such that

46

(a)

parabolic end wall

partition wall

8020 frame

55

545.5

237.2

36.1

15.5

mixed water reservoir

91.2

61.3

salt water reservoir

(b)

channel for end-wall
reflections

100mm

150 mm

experimental
section

waves

front

400 mm
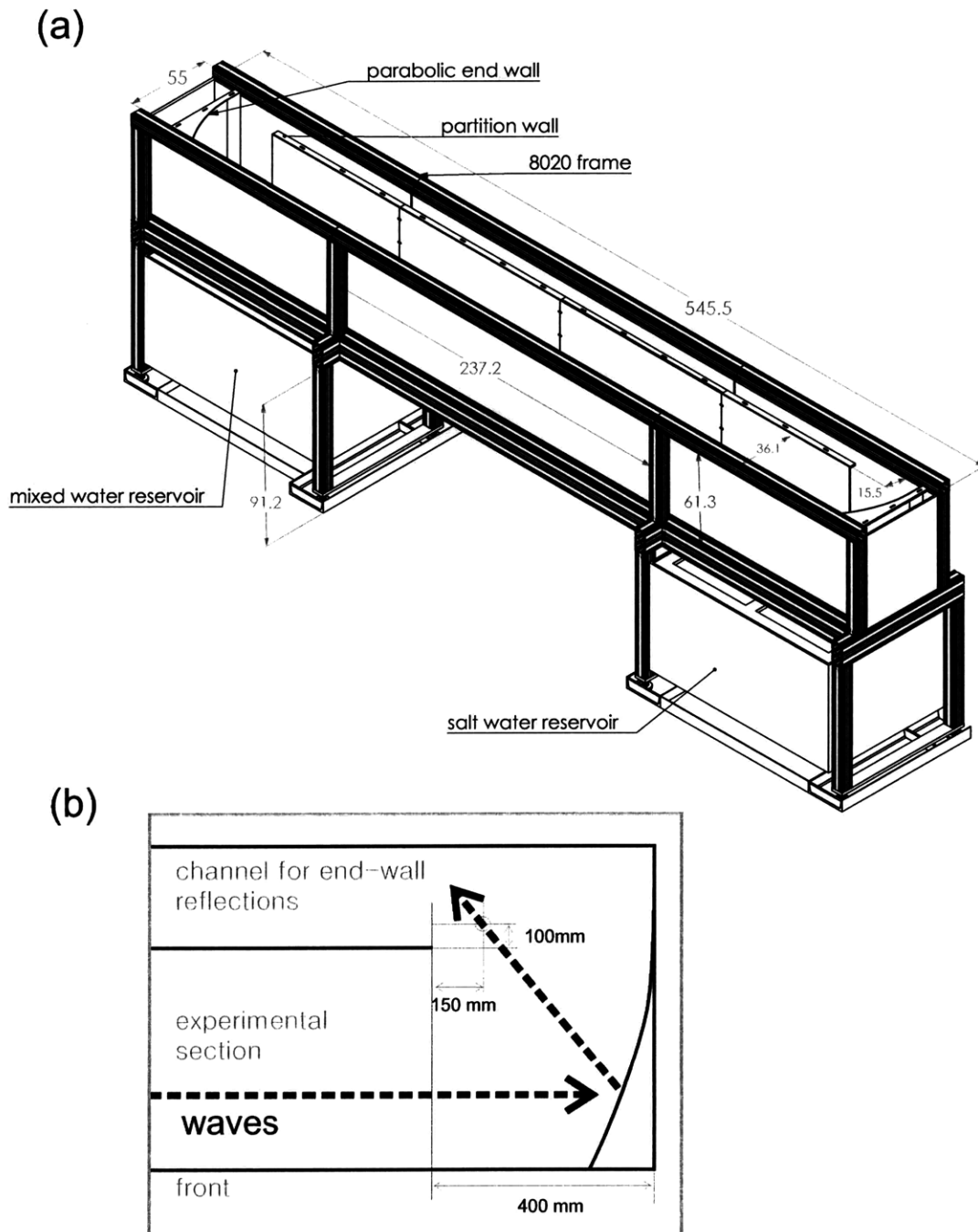
Figure 2-1: Engineering drawing of the experimental tank with key dimensions indicated in centimeters. The capacity of the tank is 5.45 ± 0.01 m-long, 0.55 ± 0.01 m-wide and 0.615 ± 0.005 m-tall. Inside are mounted one straight partition wall and two parabolic end-walls, designed to reflect the internal wave field generated in the front section toward the back section. Below the wave tank are two 800 l storage reservoirs. (b) Top-view sketch of the right end of the tank. The internal wave field that reaches the end-wall is reflected through the focus of the parabola towards the back section.

47
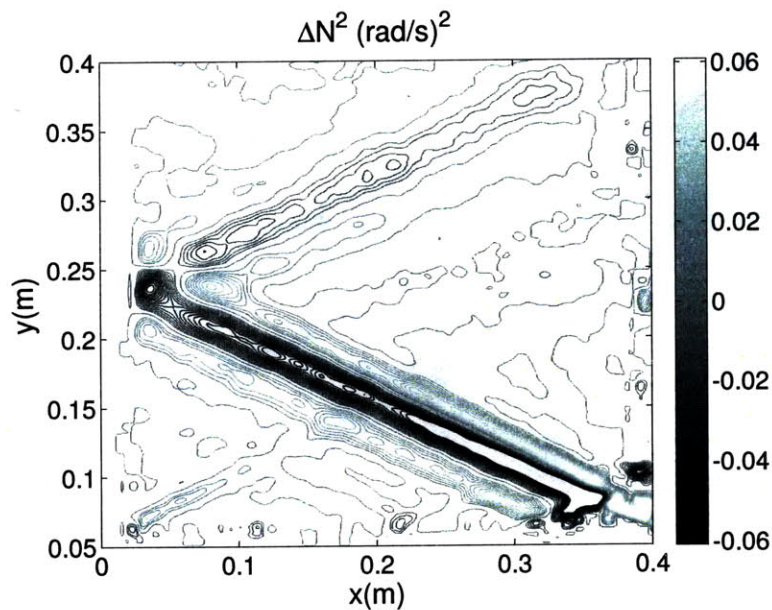
Figure 2-2: Internal wave beam reflection off a wall lined with Blocksom matting. The figure is reproduced from [17].

no returning internal wave signal was observed in the experimental region near the center of the tank. This technique was also effectively used in the experimental investigations of Peacock *et al.* [73]. For the experiments reported in chapter 4, the tank was modified by introducing a partition and a pair of parabolic end-walls, as indicated in figure 2-1. The tank is divided length-wise by a vertical wall that is 35 cm from the front-wall and has 40 cm clearance before each end-wall. The wave field is generated and measured in the 35 cm-wide front-section. At both ends of the tank, the parabola-shaped walls are positioned such that the focus of the parabola is skewed towards the rear section of the wave tank. Therefore, the energy of the wave field approaching the end-walls is reflected towards the back section so that it does not return to the experimental investigation region. Furthermore, the rear section of the tank is lined with Blocksom matting to effectively damp these unwanted waves. There was no detectable reflected wave field coming back to the experimental region in any of the experiments reported in this thesis.

48

2.1.2 Density stratification

The tank was filled with salt-stratified density gradients using the double-bucket technique of Oster [72], by which fresh and salt-water are initially kept in two separate reservoirs, and then the salt-water is mixed into the fresh water reservoir (hereby referred to as tank 2), and water from tank 2 is transferred to the experimental tank (tank 1). As time progresses, the concentration of salt in tank 2 increases. Therefore, the density in the experimental tank varies with depth in a manner that depends on the flow rates used for the mixing and for the filling. Hill [38] expanded this technique to use varying flow rates to create non-uniform stratifications. Although only the former technique was used in the experiments reported in this thesis, the laboratory is equipped to create continuous non-uniform gradients using Hill's method (this procedure is discussed in appendix A). The two large reservoirs that are seen below the tank in figure 2-1 were used to keep the (initially) fresh water and the salt-water. Cole-Palmer Masterflex computer-controlled peristaltic pumps transferred the water between reservoirs and into the experimental tank. The pumps were calibrated before each run.

Starting with a desired density profile $\rho(z)$ and a fixed flow rate f_1 into tank 1, the flow rate $f_2(t)$ into tank 2 can be computed by solving the following system of equations. The desired density in tank 2 as a function of time is related to the desired density profile $\rho_2(t(z)) = \rho(z)$, where $t(z)$, the time elapsed since the filling process is started, is given by inverting the relationship

$$z(t) = H - \frac{f_1 t}{A}, \tag{2.1.1}$$

A being the horizontal cross-sectional area of the tank and H the desired depth of the stratification. The desired density in tank 2 is therefore known at all times. Thus, the flow rate $f_2(t)$ must be set to achieve

$$\rho_2(t) = \frac{1}{V_2(t)} \left(\rho_2(0)V_2(0) + \int_0^t \rho_3 f_2(t')dt' - \int_0^t \rho_2(t')f_1(t')dt' \right), \tag{2.1.2}$$

where known parameters are the initial density $\rho_2(0)$ and volume $V_2(0)$ in the mixed reservoir, and the density in the salt-water reservoir ρ_3. The volume in tank 2 is given by

$$V_2(t) = V_2(0) + \int_0^t f_2(t')dt' - f_1 t. \tag{2.1.3}$$

To fill the wave tank with a linear density gradient simply requires that the flow rates f_1 and f_2 are set to values with a ratio of 2 : 1. For example, to fill a 30 cm-deep uniform stratification with $N = 1.0\pm$ rad/s, the mixed reservoir was filled with 750 l of water at 1000 ± 2 kg/m^3 and the salt-water reservoir was filled with 750 l of water at 1055 ± 5 kg/m^3. The pumps were set to $f_1 = 4$ l/min and $f_2 = 2$ l/min and left to run for 3.4 hours.

A uniform salt-water stratification in the wave tank persists during a period of time substantially larger than the time scale of an experiment. The one-dimensional diffusion length, found by solving Fick's second law for Dirichlet boundary conditions, is $L_D = 2\sqrt{kT_D}$, where $k = O(10^{-9})$m^2/s is the diffusivity of salt in water and T_D is the diffusion time. Therefore, it would take $T_D = O(100)$ days for a 30 cm-deep uniform stratification to erode by diffusion alone. If there are small-scale non-uniformities in the density profile, however, the diffusion process smoothes these more rapidly, for instance, $T_D = O(1000)$ s for $L_D = O(1)$ mm. Therefore, the stratification was left to settle for about an hour after filling and before running experiments, expecting that in this period diffusion would smooth out small features.

After filling the stratification and waiting, there was a thin layer of mixed fluid ~ 2 cm-thick at the very bottom of the tank. This is possibly because the inlet nozzles have a finite inner diameter of 1.27 cm, and they are centered 3.81 cm above the bottom wall of the tank, so the last volume of fluid to enter the tank may not settle properly into its buoyant level at the very bottom but instead mix within the layer of water below the height of the inlet nozzle. The resulting curvature in the profile can also enhance the beginning of the diffusion process, which starts (albeit slowly) at the top and bottom boundaries where the second derivative of the density gradient is non-zero. This bottom layer was removed before running experiments by slowly draining the tank at 1 l/min via the outlet on the bottom wall.

The stratification was measured using a Precision Measurements Engineering (PME) conductivity and temperature (CT) probe. The probe was calibrated using two sets of 6 samples of salt-water with different densities within the range of densities found in the tank (typically $\sim 1005-1020$ kg/m^3), and each set of samples was held at a different temperature, spanning the range of temperatures found in the tank (typically $T_1 = 19.00 \pm 0.05°$C and $T_2 = 24.00 \pm 0.05°$). Density and temperature profiles for a typical experiment are shown in figure 2-3. The samples were held in constant temperature baths using Neslab RTE-
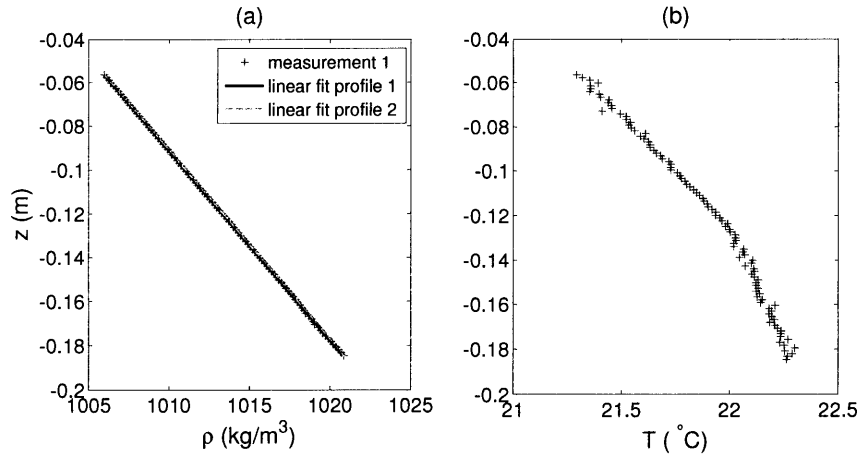
Figure 2-3: Typical vertical profiles of (a) density and (b) temperature measured in the tank. Panel (a) shows the raw data and the linear fit for one of the profile measurements, and super-imposed is the fit for the second measurement, showing negligible variability in the measurement.

140 temperature control units, the temperature was monitored using an OMEGA HH42 digital thermometer accurate to 0.01°C, and the densities were measured using a vibrating glass U-tube Anton-Paar DMA 38 densitometer accurate to 0.1kg/m^3. Figure 2-4 shows the two conductivity versus density calibration curves for the CT probe during a typical experiment. A calibration surface was defined by doing a linear interpolation between the two conductivity-density curves.

To obtain the stratification profile, the calibrated probe was lowered slowly into the tank using a Parker ER linear actuator, and held in place for 2 seconds every 1 mm. At each depth the voltage outputs, which are proportional to the conductivity and the temperature of the medium, were recorded and averaged in order to reduce high frequency noise. The probe motion control and data recording for the C-T instrument was done simultaneously via a VI using a National Instruments (NI) PCI-7344 motion controller card and a NI PCI-6036E 16-bit analog to digital converter. For each experiment set-up, two profiles were measured and the average value of N was assumed. The profiles were measured during the downward trajectory of the probe to avoid the wake that would form below the sensor tips in the upward trajectory. The calibrations were done one before and one after the profile measurements to minimize the effect of voltage drift on the sensors. The density
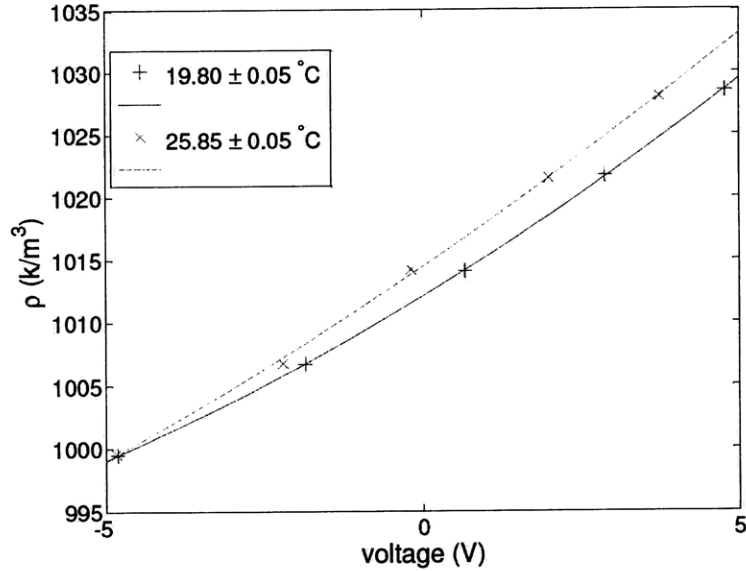
Figure 2-4: Conductivity-density calibration curves for the CT probe at two different temperatures.

and temperature profiles shown in figure 2-3 were measured in this way before one of the experiments reported in chapter 3. For this example, the stratification was measured to be $N = 1.02 \pm 0.5 \text{rad/s}$.

The involuntary temperature gradient of figure 2-3(b) develops in the tank in the period between filling and measuring the stratification and is due to temperature gradients in the laboratory, for instance due to an air conditioning unit located above the tank. The typical temperature difference, which is $O(1)°C$, is most significant in so far as it affects the conductivity of salt-water and thus the measurement obtained from the PME probe. This effect is effectively accounted for in the aforementioned calibration procedure. The effect on the uniformity of the stratification, on the other hand, is negligible, as salt-water of density 1010kg/m^3 at $21°C$ is only a hundredth of a percent ($\Delta\rho = 0.25 \text{kg/m}^3$) higher density at $22°C$.

The procedure of calibrating the probe and measuring the stratification is time consuming, taking over an hour to perform. An alternative method is to generate an internal wave beam in the stratification by oscillating an obstacle at a known frequency ω_0, use an imaging technique such as PIV to visualize the wave beam, and measure its angle of propagation θ

with respect to the horizontal. The buoyancy frequency N is related to θ and ω_0 by the dispersion relation (1.2.31). The value of θ used was the average of several measurements made from different images and at different locations within an image. The value of N was consistent whether it was calculated from direct measurements of the density profile or from measurements of the internal wave beam angles, and therefore the latter method was used in a majority of the experiments performed in uniform stratifications.

2.1.3 Topography

The model ridges were cut out of DOW blue extruded polystyrene, commonly known as insulation foam, using a FoamLinx 4-axis hot wire foam cutter that was computer-controlled to make cross-sectional cuts of any prescribed shape using the DeskCNC software. The wire cutter is shown in figure 2-5. The nickel chrome wire used for cutting was 0.25 mm in diameter. It was held between two carriages set 75 cm apart and moved simultaneously by each pair of (x, z) translation stages, tracing along a prescribed trajectory.

To achieve a smooth cut, the wire must be hot enough to melt the polystyrene faster than it travels through the foam. The wire is heated using Joule's heating, whereby the heat Q in the wire scales with the square of the current I that is passed through it:

$$Q \propto I^2 R, \qquad\qquad (2.1.4)$$

where $R = l\rho_e/A$ is the resistance of a wire with length l, cross-sectional area A and electrical resistivity ρ_e. The temperature T of the wire scales with Q according to the heat capacity c_h and the mass m of the wire: $Q = mc_h T$. For the set-up used, it was found empirically that passing a current of 1 A (which requires 12 V) through the wire and setting the cut speed to 10 in/min makes a smooth, 1 mm-thick cut.

The insulation foam was purchased in 8 ft-long, 2 ft-wide, 1 ft-tall blocks. The blocks were first cut to make one of the large faces flat, and subsequent perpendicular cuts were used to shape the block such that it would fit inside the experimental section of the tank. For the experiments performed without the partition wall, the blocks were cut to a width of 48.0 ± 0.2 cm, and for the experiments performed with the tank partition, the width was set to 33 ± 0.2 cm; thus providing, in either case, a 1 cm-clearance at either side of the tank walls. The block was then turned around to lie on the horizontal surface, and the

hot wire   computer   hot wire   foam block

x-axis z-axis   x-axis   z-axis   cut trajectory

(a)   (b)
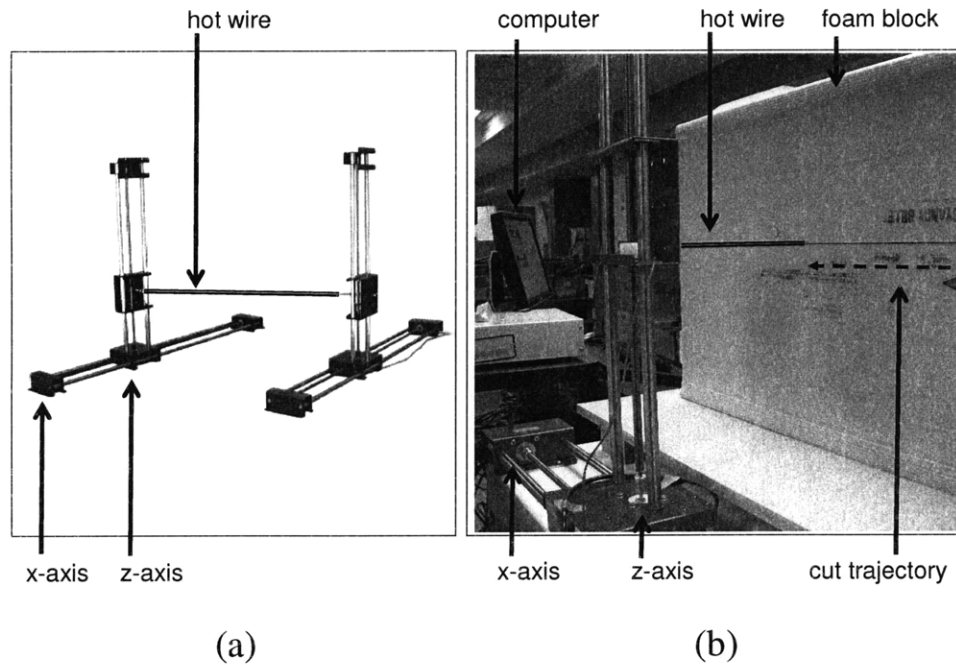
Figure 2-5: (a) Photograph of an assembled Foamlinx foam cutter, and (b) photograph while cutting a model ridge.

topographic shape was cut. The desired Gaussian shape was achieved to within ± 2 mm-accuracy.

The surface of the topographic feature was finished with a layer of Devcon 5-minute epoxy and coated with a mixture of oil-based Minwax polyurethane and pink Rhodamine 6G fluorescent dye that absorbs light at 530 nm. The epoxy allows for a smooth and impermeable surface finish to prevent the formation of air bubbles once the topography is submerged, and the pink dye absorbs the light of the green laser used in the PIV system. These measures significantly reduce the brightness of the laser reflections off the surface of the topography in order to maximize the locus of the PIV measurements, as discussed in section 2.2.

2.1.4 Tidal forcing

The barotropic tide was modeled by moving the topography back and forth in the horizontal plane, which is equivalent to oscillating currents flowing over fixed topography. As shown schematically in figure 2-6, the foam topography was mounted onto a pair of slotted plates attached to the carriage of a Parker ER linear actuator, and this was attached to the frame
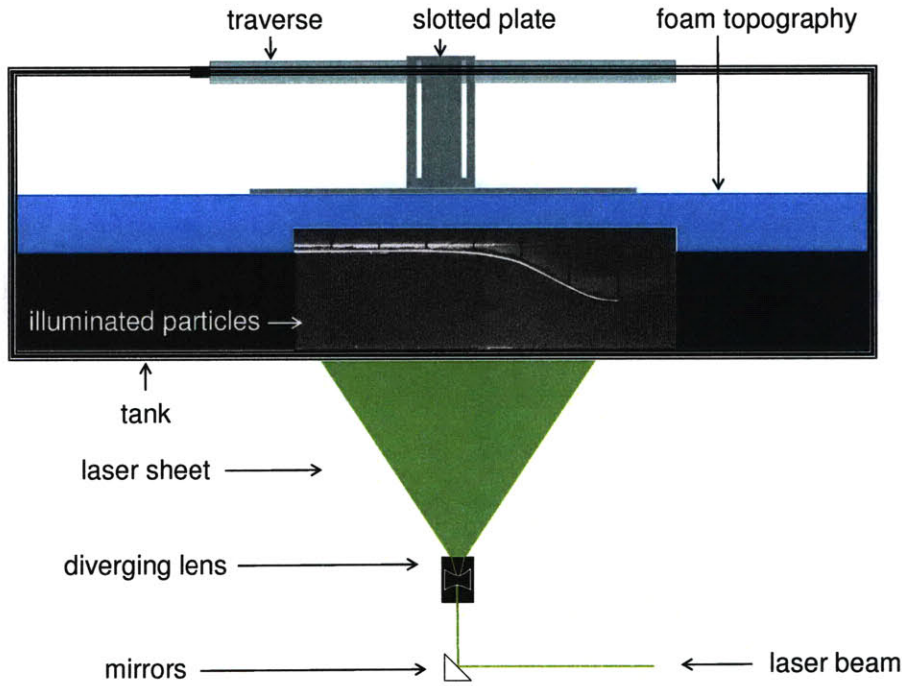
Figure 2-6: Schematic of the PIV set-up showing the laser beam passing through a cylindrical lens to form a laser sheet. A PIV image of the illuminated particles where the surface of the topography is visible is super-imposed. The foam block is on an adjustable mount that connects to the traverse, which is attached to the top of the tank.

at the top of the tank and suspended mid-way along the experimental section of figure 2-1. The actuator was oriented lengthwise. The height of the topography was adjustable up and down the slotted plates to set the depth of the experimental channel between the bottom wall of the tank and the surface of the foam.

The horizontal motion of the carriage driving the topography was controlled using a LabVIEW VI and the NI PCI-7344 motion control card. Typical peak-to-peak displacements ranged from $2A = 1 - 30 \pm 0.1$ mm and frequencies ranged from $\omega_0 = 0.5 - 1$ rad/s. The oscillatory motion was ramped up exponentially to mitigate initialization transients via the motion

$$x_t(t) = A \sin \omega_0 t (1 - e^{-t/T_s}), \tag{2.1.5}$$

where x_t is the position of the topography and $T_s = 7/\omega_0$ is the 'spin-up' time constant.

For the value of T_s given here, the amplitude of oscillation reached 99% of its final value after 5 periods of oscillation $T = 2\pi/\omega_0$. Note that the apparatus allows asymmetric tides to be reproduced, although this was not used in any of the experiments reported in this thesis.

2.2 Measurement

The velocity field of internal tides propagating in the tank was measured using a LaVision particle image velocimetry (PIV) system, shown schematically in figure 2-6. The stratification was seeded with small particles distributed randomly through the tank, which become visible when illuminated with a laser sheet. The motion of the particles was recorded using a digital camera and the velocity field was derived from the relative displacement of the particles between frames. The laser sheet was generated with a pair of class 4 Nd-Yag BigSky lasers, and the motion of the illuminated particles was recorded with an Imager Pro X 4M LaVision CCD camera with maximum resolution of 2000 by 2000 pixels for frame rates up to 14 Hz. The lasers and the camera were synchronized and controlled and the images were recorded using the DaVision 7.1 imaging software.

The seeding particles used were 8–12 μm-diameter SPHERICELL hollow glass spheres from Potter Industries, which are commercially used to reduce the viscosity of paint. Approximately 20 ml of particles were mixed into to each 800 l reservoir before filling the experimental tank. The densities of these particles are normally distributed between 1050 and 1150 kg/m^3[2], so they are slightly heavier than the range of densities found in a typical stratification. Even the heavier particles have slow settling speeds relative to the experimental time scales. The settling speed is given by Stoke's formula

$$u_\infty = -\frac{2(\rho_s - \rho_f)gd^2}{9\mu_v}, \qquad (2.2.1)$$

which yields $u_\infty = 0.04$ mm/s for $\rho_s = 1100$ kg/m^3 spheres in $\rho_f = 1025$ kg/m^3 water, where g is the acceleration due to gravity, d is the diameter of the particles and $\mu_v \approx 10^{-3}$ Pa-s is the dynamic viscosity of salt-water. Therefore, the particle settling is negligible between consecutive frames in the PIV movies, which are typically 1 s apart. Furthermore, the particles remain suspended evenly throughout the stratification up to a day after the tank is filled, which is the period when PIV measurements are taken.

A configuration of mirrors guided the laser beam through the bottom of the tank into the field of view that was captured during experiments. Before entering the tank, the laser beam passed through a LaVision sheet optics device that has a cylindrical divergent lens with focal length -20 mm, which splits a 3 mm-diameter beam into a triangular sheet with a $20°$ spread angle. The forward face of the partition wall and the bottom wall of the tank were lined with matte black contact-paper except for a 2 cm-wide length-wise slot through which the laser sheet entered the tank. The laser sheet illuminated the particles in the stratification and hit the surface of the topographic feature, where a significant fraction of the light intensity was absorbed by the rhodamine dye. The black lining of the surrounding walls served to reduce reflections of the laser light scattered by the variety of surfaces in the tank.

The typical area captured in the PIV images was 30 cm by 30 cm, corresponding to an image of 804 by 804 pixels. With the camera placed about 1 m in front of the tank, the energy level of the laser beam was set so that a typical particle was about 3 pixels in diameter. Particles were about 10 pixels apart. After experiments, a ruler was introduced in the tank and aligned with the laser sheet location, and this was used to provide a calibration length-scale for the movies.

The displacement of the particles between frames, as shown for example in figure 2-7, is obtained by maximizing the cross-correlation between consecutive frames. The movies were analyzed in DaVision 7.1 using the PIV time-series algorithm, for which one laser is synchronized with the camera and set to pulse at a rate typically around 1 Hz. The rates were chosen to have at least 16 (and always an exact power of 2) data points per tidal cycle for a given experiment. The velocity estimation is performed as follows, with representative values quoted for the computation parameters. Each image is divided into 32 by 32 pixels interrogation windows that overlap by 75%. Each of these windows is cross-correlated with a set of windows of the same size in the following image that are centered within 12 pixels of the center of the original window. Typical particle displacements between images were about 10 pixels. The velocity vector at the center of the original window is chosen to be the frame rate times the displacement vector between the two consecutive windows that have the highest cross-correlation. In post-processing, the software can be used to remove vectors that deviate significantly from the root mean square of their neighbors and to apply spatial smoothing and filters.
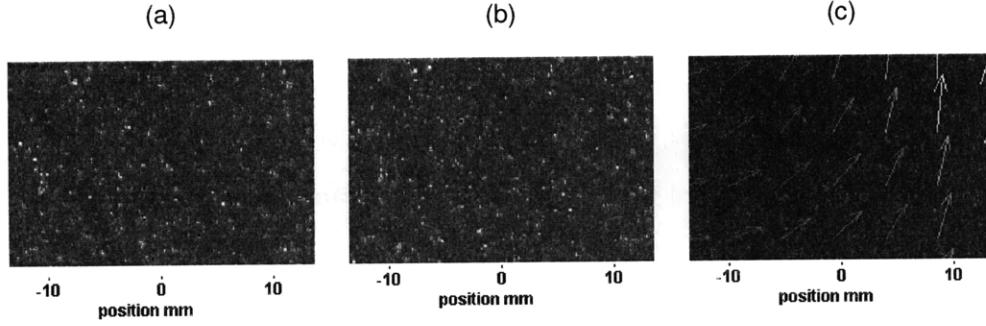
Figure 2-7: Zoom-in on (a,b) two consecutive snapshots of the wave field captured using the PIV apparatus, and (c) the particle displacement obtained by processing the raw images using the PIV time-series algorithm. The time elapsed between frames (a) and (b) is 0.45 s. The size of the vectors in panel (c) is 10 times the calculated particle displacement between the two frames, and the actual resolution of the PIV data is 4 times the resolution of the vectors shown.

The density stratification in the tank is associated with a change in the refractive index of the salt-water medium. The light that is scattered by the PIV particles is therefore diffracted as it travels through the tank, such that the particle position z_a captured in the image on the CCD sensor is not the true position of the particle z_p. Therefore, there is a small distortion of the velocity field and also a small spurious velocity $\Delta w = |w_a - w_p|$ due to the time-varying density perturbations associated with the internal wave field, as investigated by Dalziel *et al.* [13]. However, the magnitude of these errors is negligible for the experiments performed. In particular, the position error

$$\Delta z = |z_a - z_p| = \frac{1}{8}\frac{W^2}{n_0}\frac{\partial n}{\partial z} \approx 2.5 \times 10^{-6}\text{m}, \tag{2.2.2}$$

and the velocity error

$$\Delta w = \frac{1}{8}\frac{W^2}{n_*}\frac{\partial^2 n}{\partial z \partial t} \approx 2.3 \times 10^{-6}\text{m/s}, \tag{2.2.3}$$

where $W = 0.1\,\text{m}$ is the distance between the front wall of the tank and the plane of the laser light-sheet, n is the local refractive index of the stratification and $n_* = 1.33$ is the refractive index of fresh water. In the tank, the change in the refractive index is due to density perturbations:

$$\frac{\partial n}{\partial z} = \frac{\partial n}{\partial \rho}\frac{\partial \rho}{\partial z}, \tag{2.2.4}$$

58

and the relationship between density and refractive index can be linearized locally such that

$$\frac{\partial n}{\partial \rho} = \frac{n_*}{\rho_*}\beta, \tag{2.2.5}$$

where the empirical constant $\beta = 0.184$ and $\rho_* = 998\mathrm{kg/m^3}$. The typical density perturbation is

$$\frac{\partial \rho}{\partial z} = \frac{-\rho_*}{g}\Delta N^2 \approx 10.3\mathrm{kg/m^{-4}}, \tag{2.2.6}$$

where $\Delta N^2 \approx 0.05\,\mathrm{rad/s}$ is a typical perturbation associated with an internal wave signal generated in the laboratory as shown, for instance, in figure 2-2. Substituting these values into equations (2.2.4) and (2.2.5) yields the error reported in (2.2.2). The rate of change of the perturbations to the refractive index is

$$\frac{\partial}{\partial t}\frac{\partial n}{\partial z} = \beta\frac{n_*}{g}\frac{\partial}{\partial t}\left(\Delta N^2\right), \tag{2.2.7}$$

and

$$\frac{\partial}{\partial t}\left(\Delta N^2\right) = \frac{\partial}{\partial t}\left(b_z\right) = \frac{\partial}{\partial z}\left(wN^2\right) \approx 10^{-2}\ \mathrm{rad/s^2}, \tag{2.2.8}$$

for a typical perturbation velocity $w \approx 10^{-4}\,\mathrm{m/s}$ over a typical vertical distance $\approx 0.01\,\mathrm{m}$. Substituting the estimate of (2.2.8) into equation (2.2.7) yields the error reported in (2.2.3).

Chapter 3

An isolated ridge in uniform stratification

This chapter presents the results of an experimental investigation of the fundamental problem of internal tide generation by a two-dimensional isolated tall ridge in a uniform density stratification. This configuration is representative of sites of strong internal tide generation in the ocean, and is a simple canonical shape worth investigating before tackling the complexities of more realistic topographies in non-uniform stratifications. The frequency and amplitude of the tidal forcing were varied to span parameter regimes corresponding to sub- to supercritical topographies and small to intermediate excursion amplitudes. The geometry of the topographic feature and the depth of the channel were unchanged. The wave fields generated in the laboratory are compared to the theoretical solution of Pétrélis *et al.* [75] and to numerical simulations performed by Professor Kraig Winters.

The following section 3.1 is a review of a theoretical approach to modeling 2-D internal tide generation. This is followed in section 3.2 by a description of the configuration of the experiments and the simulations, and the method for performing a modal decomposition of the experimental and numerical wave fields. Section 3.3 presents a direct comparison of the wave fields generated in experiments and numerics and predicted by theory, and section 3.4 presents the results of the modal decomposition analysis on experiments with small and large excursion amplitudes. The results are discussed in section 3.5.

3.1 Linear theory

The problem of linear internal tide generation by a finite-amplitude, single symmetric ridge with monotonic slopes in a finite-depth ocean of uniform stratification was solved by Pétrélis et al. [75] using the Green function solution of Robinson [81]. In this approach, the topography is modeled as a distribution of singularities and the wave field as the super-position of the Green functions that solve the governing equation for each singularity in the domain. The solution can be expressed as a sum of vertical modes that conveniently characterize the wave field, such that the rate of energy converted into the baroclinic tide can be directly related to the modal structure of the internal tide.

3.1.1 Green function solution

The following non-dimensional coordinates simplify the boundary value problem of section 1.2 that governs internal tide generation:

$$Z = \frac{\pi z}{H} \qquad \text{and} \qquad X = \frac{\pi x}{\mu H}, \qquad (3.1.1)$$

where $\mu = 1/\tan\theta$ is the inverse slope of the direction of the propagation of internal wave rays. This operation maps the vertical coordinate into $Z = [0 : \pi]$ and scales the horizontal coordinate X so that internal wave rays propagate at $45°$. Substituting X and Z into the internal wave equation (1.2.33) and the boundary conditions (1.2.34), yields the governing equation

$$\phi_{XX}(X, Z) - \phi_{ZZ}(X, Z) = 0, \qquad (3.1.2)$$

where ϕ is the spatial structure of the stream function $\psi = U\Re[\phi e^{-i\omega_0 t}]$; and boundary conditions

$$\phi(X_T, Z) = z \qquad \text{and} \qquad \phi(X, \pi) = 0. \qquad (3.1.3)$$

The non-dimensional profile of the topography, which is assumed to be horizontally symmetric, is expressed as a function of Z as $X_T = \pm Q(Z)$ in $Z \in [0 : \hat{h}_0]$, where $\hat{h}_0 = h_0\pi/H$ is the non-dimensional height of the topography. In addition, the wave field must satisfy the radiation condition, which requires that the stream function of equation (1.2.32) propagates away from the topography. Note that, despite having introduced a dimensionless coordinate system, at this stage it is still convenient to retain ϕ as a dimensional quantity.

62

The general solution to equation (3.1.2) can be expressed in terms of the Green function $G(X, X'; Z, Z')$ that solves an analogous equation forced by a singularity at (X', Z'):

$$G_{XX} - G_{ZZ} = i\delta(X - X')\delta(Z - Z'), \qquad (3.1.4)$$

where δ is Dirac's delta function. The Green function is also subject to homogeneous boundary conditions in Z

$$G(X, X'; 0, Z') = G(X, X'; \pi, Z') = 0, \qquad (3.1.5)$$

and to the radiation condition away from X'.

When $X \neq X'$ and $Z \neq Z'$, equation (3.1.4) is a homogeneous problem with a separable solution

$$G(X, X'; Z, Z') = G(X, Z) = \mathcal{F}(X)\mathcal{H}(Z). \qquad (3.1.6)$$

Substituting (3.1.6) into equation (3.1.2) yields

$$\mathcal{F}''\mathcal{H} = \mathcal{F}\mathcal{H}'', \qquad (3.1.7)$$

which implies that

$$\frac{\mathcal{F}''}{\mathcal{F}} = \frac{\mathcal{H}''}{\mathcal{H}} = q^2 \qquad (3.1.8)$$

where q is a constant. These second order ordinary differential equations have solutions

$$\mathcal{F}(X) = C_1 e^{qX} + C_2 e^{-qX} \qquad \text{and} \qquad \mathcal{H}(Z) = D_1 e^{qZ} + D_2 e^{-qZ}. \qquad (3.1.9)$$

The boundary conditions in Z,

$$\mathcal{H}(0) = \mathcal{H}(\pi) = 0 \qquad (3.1.10)$$

and so

$$D_1 + D_2 = D_1 e^{q\pi} + D_2 e^{-q\pi} = 0,$$

require q to be an imaginary integer, such that, if we let $q = ip$, then

$$\mathcal{H}_p(Z) = b_p \sin pZ \qquad \text{and} \qquad \mathcal{F}_p(X) = C_1 e^{ipX} + C_2 e^{-ipX}. \qquad (3.1.11)$$

63

The form of $\mathcal{H}_p(Z)$ reveals that the solution is a linear combination of sinusoidal vertical modes. The form of $\mathcal{F}(X)$ suggests a way to interpret the radiation condition in X. The stream function has the form

$$\psi(X, Z, t) \propto \Re\left\{b_p \sin pZ \left[C_1 e^{i(pX - \omega_0 t)} + C_2 e^{i(-pX - \omega_0 t)}\right]\right\}. \qquad (3.1.12)$$

For the term proportional to C_1, a line of constant phase $\Phi = pX - \omega_0 t$ propagates to the right because the X-position, $X = (\omega_0 t + \Phi)/p$, increases with time. Similarly, the term proportional to C_2 propagates to the left. We require that the waves propagate to the right for $X > X'$ and to the left for $X < X'$. This is satisfied if

$$\mathcal{F}_p(X) = C e^{ip|X - X'|}, \qquad (3.1.13)$$

for which

$$\psi(X, Z, t) \propto \Re\left\{b_p \sin pZ \left[C e^{i(p|X - X'| - \omega_0 t)}\right]\right\} \qquad (3.1.14)$$

and, therefore, for a line of constant phase $\Phi = p|X - X'| - \omega_0 t$, the relative X-position with respect to X' increases with time: $|X - X'| = (\omega_0 t + \Phi)/p$.

Thus so far, for $X \neq X'$ and $Z \neq Z'$, the most general form of the Green function is

$$G(X, X'; Z, Z') = \sum_{p=1}^{\infty} g_p(X, X'; Z') \sin pZ, \qquad (3.1.15)$$

where

$$g_p(X - X'; Z') = f_p(Z') e^{ip|X - X'|}, \qquad (3.1.16)$$

and equation (3.1.4) becomes

$$\sum_{p=1}^{\infty} (g_{p,XX} + p^2 g_p) \sin pZ = i\delta(X - X')\delta(Z - Z'). \qquad (3.1.17)$$

An expression for $f_p(Z')$ is found by ensuring that equation (3.1.17) is satisfied across the singularity. First, we project equation (3.1.17) onto the sinusoidal vertical modes of the solution:

$$\int_0^{\pi} \sum_{p=1}^{\infty} (g_{p,XX} + p^2 g_p) \sin pZ \sin mZ \, dZ = i\delta(X - X') \int_0^{\pi} \delta(Z - Z') \sin mZ \, dZ. \qquad (3.1.18)$$

64

On the right-hand side, the result of the convolution with the Dirac function is the value of the vertical mode evaluated at Z':

$$\int_0^\pi \sum_{p=1}^\infty (g_{p,XX} + p^2 g_p) \sin pZ \sin mZ dZ = i\delta(X - X') \sin mZ'. \qquad (3.1.19)$$

On the left hand side, one can exchange the order of summation and integration,

$$\sum_{p=1}^\infty (g_{p,XX} + p^2 g_p) \int_0^\pi \sin pZ \sin mZ dZ = i\delta(X - X') \sin mZ', \qquad (3.1.20)$$

and invoke orthogonality, whereby the integral is only non-zero when $p = m$, and in particular

$$\frac{\pi}{2}(g_{m,XX} + m^2 g_m) = i\delta(X - X') \sin mZ'. \qquad (3.1.21)$$

Then, we integrate in a small interval around X':

$$\lim_{\varepsilon \to 0} \left[\frac{\pi}{2} \int_{X'-\varepsilon}^{X'+\varepsilon} (g_{p,XX} + p^2 g_p) dX \right] = i \sin pZ', \qquad (3.1.22)$$

where we have resumed using p for the integer mode numbers. The second term in the integrand has a finite value at X', so it goes to zero in the limit of $\varepsilon \to 0$. The rest of the integral is evaluated using the first fundamental theorem of calculus:

$$\lim_{\varepsilon \to 0} \left[\frac{\pi}{2} g_{p,X} \Big|_{X'-\varepsilon}^{X'+\varepsilon} \right] = i \sin pZ', \qquad (3.1.23)$$

where $g_{p,X}$ can be evaluated by differentiating the definition given in equation (3.1.16), so

$$\lim_{\varepsilon \to 0} \left[ip\, \text{sgn}(X - X') f_p(Z') e^{ip|X-X'|} \Big|_{X'-\varepsilon}^{X'+\varepsilon} \right] = i \frac{2}{\pi} \sin pZ'. \qquad (3.1.24)$$

Equation (3.1.24) can be solved for $f_p(Z')$:

$$
\begin{aligned}
\lim_{\varepsilon \to 0} \left[p f_p(Z')(e^{ip\varepsilon} - -e^{-ip\varepsilon}) \right] &= \frac{2}{\pi} \sin pZ', \\
\lim_{\varepsilon \to 0} \left[2p f_p(Z') \cos p\varepsilon \right] &= \frac{2}{\pi} \sin pZ', \\
f_p(Z') &= \frac{1}{\pi p} \sin pZ'. \qquad (3.1.25)
\end{aligned}
$$

65

Substituting $f_p(Z')$ back into equation (3.1.15) yields the Green function:

$$G(X, X'; Z, Z') = \sum_{p=1}^{\infty} \frac{1}{\pi p} \sin pZ' \sin pZ e^{ip|X-X'|}. \tag{3.1.26}$$

Following the lead of Robinson [81], the solution to equations (3.1.2) and (3.1.3) can be expressed as a super-position of Green functions, which solve the wave field for a distribution $\gamma(Z)$ of singularities along the topography X_T:

$$\phi(X, Z) = \frac{H}{\pi} \int_0^{\hat{h}_0} \gamma(Z') G(X, X_T; Z, Z') dZ'. \tag{3.1.27}$$

More specifically,

$$\phi(X, Z) = \frac{H}{\pi} \int_0^{\hat{h}_0} \gamma(Z') \left[G(|X - Q(Z')|; Z, Z') + G(|X + Q(Z')|; Z, Z') \right] dZ' \tag{3.1.28}$$

to account for both slopes of the topography X_T.

It remains to find $\gamma(Z)$ so that the solution (3.1.28) satisfies the boundary condition (3.1.3) on the topography:

$$Z = \int_0^{\hat{h}_0} \gamma(Z') \left[G(|Q(Z) - Q(Z')|; Z, Z') + G(|Q(Z) + Q(Z')|; Z, Z') \right] dZ'. \tag{3.1.29}$$

Substituting the Green function (3.1.26) into equation (3.1.29) yields

$$Z = \frac{1}{\pi} \sum_{p=1}^{\infty} \frac{\sin pZ}{p} \int_0^{\hat{h}_0} \gamma(Z') \sin pZ' \left[e^{ip|Q(Z)-Q(Z')|} + e^{ip|Q(Z)+Q(Z')|} \right] dZ'. \tag{3.1.30}$$

Equation (3.1.30) is discretized and solved for $\gamma(Z)$ in the manner described in the appendix of Pétrélis *et al.* [75]. The analytical results shown in this chapter were produced from the $\gamma(Z)$ obtained using the numerical code provided by Pétrélis *et al.* [75]. A different algorithm was used to solve problems involving more complex topography and nonlinear stratifications, and this effort is detailed in chapter 4.

Note that in the far field, where $X > Q(Z)$, the solution (3.1.28) can be written as

$$\phi(X, Z) = \frac{H}{\pi} \int_0^{\hat{h}_0} \gamma(Z') \sum_{p=1}^{\infty} \frac{2}{\pi p} \sin pZ \sin pZ' \left[e^{ip(X - Q(Z'))} + e^{ip(X + Q(Z'))} \right] dZ'$$

$$= \frac{H}{\pi} \sum_{p=1}^{\infty} \frac{4}{\pi p} \sin pZ e^{ipX} \int_0^{\hat{h}_0} \gamma(Z') \sin pZ' \cos(pQ(Z')) dZ'. \qquad (3.1.31)$$

Exploiting this simplification, one can define

$$\gamma_p \equiv \frac{4}{\pi} \int_0^{\hat{h}_0} \gamma(Z') \sin pZ' \cos(pQ(Z')) dZ', \qquad (3.1.32)$$

so, in the far right field, the solution (3.1.31) is conveniently expressible as a sum over the vertical basis modes of the uniform stratification:

$$\phi(X, Z) = \frac{H}{\pi} \sum_{p=1}^{\infty} \frac{\gamma_p}{p} \sin pZ \, e^{ipX}. \qquad (3.1.33)$$

3.1.2 Energy flux

The energy equation for linear internal waves is found by taking the scalar product of the perturbation velocity with the linearized momentum equation (1.2.18). This yields

$$\mathbf{u} \cdot \frac{\partial \mathbf{u}}{\partial t} = -\mathbf{u} \cdot \left(\frac{\nabla p}{\rho_*} + b\hat{k} \right), \qquad (3.1.34)$$

and after some re-arrangement

$$\rho_* \frac{\partial}{\partial t} \left(\frac{\mathbf{u} \cdot \mathbf{u}}{2} \right) + \psi_x p_z - \psi_z p_x + w \rho_* b = 0. \qquad (3.1.35)$$

Using the density equation (1.2.19), the last term in equation (3.1.35) can be written as the rate of change of potential energy:

$$w \rho_* b = -\rho_* \frac{b}{N^2} \frac{\partial b}{\partial t} = -\rho_* \frac{\partial}{\partial t} \left(\frac{1}{2} \frac{b^2}{N^2} \right). \qquad (3.1.36)$$

Now equation (3.1.35) can be re-written

$$\frac{\rho_*}{2} \frac{\partial}{\partial t} \left(u^2 + v^2 - \frac{b^2}{N^2} \right) + \psi_x p_z - \psi_z p_x = 0, \qquad (3.1.37)$$

67

where the first term represents the local rate of change of energy, and the second and third terms in combination represent the divergence of the energy flux. The instantaneous two-dimensional energy flux, measured in Watts/m per unit of length along the ridge, is

$$\mathbf{J} = p\mathbf{u}. \tag{3.1.38}$$

The divergence of the energy flux is

$$\nabla \cdot \mathbf{J} = \nabla p \cdot \mathbf{u} + p\nabla \cdot \mathbf{u}, \tag{3.1.39}$$

where the second term in equation (3.1.39) is zero by the continuity equation (1.2.29), so

$$
\begin{aligned}
\nabla \cdot \mathbf{J} &= p_x u + p_z w \\
&= -p_x \psi_z + p_z \psi_x.
\end{aligned} \tag{3.1.40}
$$

The barotropic to baroclinic conversion rate is the rate at which baroclinic energy radiates away from the generation region, and it is found by integrating the time-averaged far-field energy flux over the vertical domain:

$$C = \int_0^H <\mathbf{J} \cdot \hat{\imath}> dz = -\int_0^H <p\psi_z> dz. \tag{3.1.41}$$

Equation (3.1.41) can be evaluated in a slightly different manner, which is more amenable to the following discussion. The energy flux can be written as

$$\mathbf{J} = \psi p_z - \psi p_x - \nabla \times \psi p. \tag{3.1.42}$$

Applying the same operation that acts on $\mathbf{J}$ in equation (3.1.41) to the curl term in equation (3.1.42) yields

$$-\int_0^H <(\nabla \times \psi p) \cdot \hat{\imath}> dz = \int_0^H <\frac{\partial}{\partial z}(\psi p)> dz, \tag{3.1.43}$$

since $\partial/\partial y = 0$ for the 2-D problem. Furthermore,

$$-\int_0^H <(\nabla \times \psi p) \cdot \hat{\imath}> dz = (\psi p)\,|_0^H = 0, \tag{3.1.44}$$

68

by the far-field boundary condition $\psi(x,0) = \psi(x,H) = 0$. Therefore,

$$\int_0^H < p\psi_z > dz = \int_0^H < p_z\psi > dz, \tag{3.1.45}$$

and for convenience it is the right-hand side of equation (3.1.45) that is evaluated. This has been implemented before by Llewellyn Smith and Young [54], [55] and Pétrélis *et al.* [75], and the equivalence of either side of (3.1.45) has been confirmed by plotting the corresponding wave fields using the theory.

One can express p_z in terms of ψ. From the vertical momentum equation (1.2.27),

$$p_z = \rho_*(-w_t + b). \tag{3.1.46}$$

The time derivative of the vertical velocity is

$$
\begin{aligned}
w_t &= U\frac{\partial}{\partial t}\Re\left[\phi_x e^{-i\omega_0 t}\right] \\
&= \omega_0 U\left\{-\Re[\phi_x]\sin\omega_0 t + \Im[\phi_x]\cos\omega_0 t\right\} \\
&= \omega_0 U\Im\left[\phi_x e^{-i\omega_0 t}\right],
\end{aligned}
\tag{3.1.47}
$$

where $\Re$ and $\Im$ indicate the real and imaginary parts, respectively; and the buoyancy field is obtained by integrating the density equation (1.2.28)

$$b_t = N^2 w = N^2 U\Re\left[\phi_x e^{-i\omega_0 t}\right], \tag{3.1.48}$$

and assuming zero initial buoyancy $b(x,z,0) = 0$, such that

$$
\begin{aligned}
b &= \frac{N^2 U}{\omega_0}\left\{\Re[\phi_x]\sin\omega_0 t - \Im[\phi_x]\cos\omega_0 t\right\}, \\
&= -\frac{N^2 U}{\omega_0}\Im\left[\phi_x e^{-i\omega_0 t}\right].
\end{aligned}
\tag{3.1.49}
$$

Substituting (3.1.47) and (3.1.49) into (3.1.46) yields

$$p_z = -\rho_* U\frac{N^2 - \omega_0^2}{\omega_0}\Im\left[\phi_x e^{-i\omega_0 t}\right]. \tag{3.1.50}$$

69

Implementing the time-average requires the following operation:

$$
\begin{aligned}
< p_z \psi > \ &= \ -\rho_* U^2 \frac{(N^2 - \omega_0^2)}{\omega_0} < \Im[\phi_x e^{-i\omega_0 t}] \Re[\phi e^{-i\omega_0 t}] > \\
&= \ -i\rho_* U^2 \frac{(N^2 - \omega_0^2)}{\omega_0} \frac{\omega_0}{2\pi} \int_0^{2\pi/\omega_0} \Im[\phi_x e^{-i\omega_0 t}] \Re[\phi e^{-i\omega_0 t}] dt.
\end{aligned} \tag{3.1.51}
$$

Expanding the integrand in equation (3.1.51) yields three terms:

$$
\begin{aligned}
I \ &= \ \Im[\phi_x e^{-i\omega_0 t}] \Re[\phi e^{-i\omega_0 t}] \\
&= \ -\Im[\phi]\Re[\phi_x] \cos^2(\omega_0 t) + \Im[\phi_x]\Re[\phi] \sin^2(\omega_0 t) \\
&\quad + \{\Im[\phi]\Im[\phi_x] - \Re[\phi]\Re[\phi_x]\} \cos\omega_0 t \sin\omega_0 t.
\end{aligned} \tag{3.1.52}
$$

Since

$$
\int_0^{2\pi/\omega_0} \cos^2(\omega_0 t) dt = \int_0^{2\pi/\omega_0} \sin^2(\omega_0 t) dt = \pi/\omega_0, \tag{3.1.53}
$$

and

$$
\int_0^{2\pi/\omega_0} \cos\omega_0 t \sin\omega_0 t \, dt = 0, \tag{3.1.54}
$$

the integral in (3.1.51) is

$$
\int_0^{2\pi/\omega_0} I \, dt = \frac{\pi}{\omega_0} \left(\Re[\phi]\Im[\phi_x] - \Im[\phi]\Re[\phi_x]\right) = -\frac{i\pi}{2\omega_0} \left(\phi\phi_x^* - \phi^*\phi_x\right), \tag{3.1.55}
$$

where the super-script (*) denotes a complex conjugate.

The integrand for the conversion rate (3.1.41) is thus

$$
< p_z \psi > = -i\rho_* U^2 \frac{(N^2 - \omega_0^2)}{4\omega_0} \left(\phi\phi_x^* - \phi^*\phi_x\right). \tag{3.1.56}
$$

To evaluate the far-field conversion, ϕ in (3.1.56) can be expressed in terms of γ_p's using equation (3.1.33), giving

$$
< p_z \psi > = -i\rho_* U^2 \frac{(N^2 - \omega_0^2)}{4\omega_0} \frac{iH}{\mu\pi} \sum_{p=1}^{\infty} \sum_{q=1}^{\infty} \frac{1}{q} \sin\left(\frac{pz\pi}{H}\right) \sin\left(\frac{qz\pi}{H}\right) \left(\gamma_p\gamma_q^* e^{i(p-q)x} + \gamma_p^*\gamma_q e^{i(q-p)x}\right).
$$

$$\tag{3.1.57}$$

The only non-zero term after integrating equation (3.1.57) over the vertical domain corre-

sponds to $p = q$, in which case the depth integral of the z-dependent part is

$$\int_0^H \sin^2\left(\frac{pz\pi}{H}\right)dz = \frac{H}{2},$$

(3.1.58)

so

$$
\begin{aligned}
C &= \int_0^H <p_z\psi> dz \\
&= \rho_* U^2 H^2 \frac{(N^2 - \omega_0^2)}{8\mu\pi\omega_0} \sum_{p=1}^\infty \frac{1}{p}\left(\gamma_p\gamma_p^* + \gamma_p^*\gamma_p\right) \\
&= \rho_* U^2 H^2 \frac{(N^2 - \omega_0^2)}{4\mu\pi\omega_0} \sum_{p=1}^\infty \frac{|\gamma_p|^2}{p}.
\end{aligned}
$$

(3.1.59)

We thus define the non-dimensional conversion rate as

$$C_* = \sum_{p=1}^\infty \frac{|\gamma_p|^2}{p},$$

(3.1.60)

which captures the dependence of the conversion rate on the modal composition.

3.1.3 Modifications for comparison with laboratory experiments

The solution of Pétrélis et al. [75] is applicable to tidal conversion by topography on geophysical scales, so three modifications were implemented for comparison with laboratory measurements. Firstly, in the experiments ω_0 and N are of the same order of magnitude, so the derivation presented in sections 3.1.1 and 3.1.2 retained the non-hydrostatic terms. Secondly, the experiments are non-rotating, so that $f = 0$ and the inverse slope of the internal wave rays is therefore

$$\mu = \frac{\sqrt{N^2 - \omega_0^2}}{\omega_0}.$$

(3.1.61)

Finally, in the experiments the Reynolds number, $\text{Re} = U h_0/\nu$, lies in the range $50 \leq \text{Re} \leq 850$ as opposed to $\text{Re} \approx O(10^7)$ in the ocean (for tidal currents $U = O(1)\text{cm/s}$, ridge heights $h_0 = O(1000)\text{m}$ and $\nu \approx 1.1 \times 10^{-6}\text{m}^2/\text{s}$ for salt water). The propagating wave field was therefore corrected for the effect of viscosity in a similar manner to the approaches of Hurley and Keady [40], Flynn, Onu and Sutherland [24] and Peacock, Echeverri and Balmforth [73].

The viscous correction is obtained by assuming that the wave field is dissipated by

viscosity as it propagates along X. Thus, if the solution has an X-dependent factor $\phi_p(X)$, such that

$$\phi(X, Z) = \frac{H}{\pi} \sum_{p=1}^{\infty} \phi_p(X) \frac{\gamma_p}{p} \sin pZ, \qquad (3.1.62)$$

then, reverting to dimensional coordinate for the moment, $\phi(x, z)$ must satisfy the fully viscous internal wave equation

$$(N^2 - \omega_0^2) \frac{\partial^2 \phi(x, z)}{\partial x^2} - \omega_0^2 \frac{\partial^2 \phi(x, z)}{\partial z^2} = i\omega_0 \nu \nabla^4 \phi(x, z), \qquad (3.1.63)$$

and ϕ_p must decay away from the generation site. Substituting into equation (3.1.63) yields

$$(N^2 - \omega_0^2)\phi_p'' + \omega_0^2 \left(\frac{p\pi}{H}\right)^2 \phi_p = i\omega_0 \nu \left[\phi_p^{(4)} + \left(\frac{p\pi}{H}\right)^4 - 2\left(\frac{p\pi}{H}\right)^2 \phi_p''\right]. \qquad (3.1.64)$$

Equation (3.1.64) has solutions $\phi_p = C_p e^{k_p x}$ with roots k_p that satisfy the characteristic polynomial

$$(N^2 - \omega_0^2)k_p^2 + \omega_0^2 \left(\frac{p\pi}{H}\right)^2 = i\omega_0 \nu \left[k_p^4 + \left(\frac{p\pi}{H}\right)^4 - 2\left(\frac{p\pi}{H}\right)^2 k_p^2\right]. \qquad (3.1.65)$$

Out of the four roots we seek the dominant term that allows the solution to dissipate in X. This is expected to be a weakly viscous correction to the inviscid solution, so it can be approximated as a leading order correction in ν:

$$k_p \approx k_{p,I} + i\nu k_{p,V},$$

$$k_p^2 \approx k_{p,I}^2 + 2i\nu k_{p,I} k_{p,V}, \qquad (3.1.66)$$

where the inviscid solution,

$$k_{p,I}^2 = -\left(\frac{p\pi}{\mu H}\right)^2, \qquad (3.1.67)$$

is obtained by multiplying equation (3.1.65) by ν and setting $\nu = 0$. Substituting (3.1.66) into (3.1.65) yields

$$k_{p,V} = -\frac{p^2}{2\omega_0 \mu} \left(\frac{\pi}{H}\right)^3 \left(\frac{N^2}{N^2 - \omega_0^2}\right)^2. \qquad (3.1.68)$$

72

We express the viscous correction as a factor κ_p of the exponent in equation (3.1.33):

$$\omega(X, Z) = \frac{H}{\pi} \sum_{p=1}^{\infty} \frac{\gamma_p}{p} \sin pZ \, e^{ip\kappa_p X}, \tag{3.1.69}$$

where

$$\kappa_p = 1 + \frac{i\nu}{2\omega_0} \left(\frac{p\pi}{H}\right)^2 \left[\frac{N^2}{N^2 - \omega_0^2}\right]^2. \tag{3.1.70}$$

Note that the κ_p provides aggressive damping of high vertical modes ($p \geq 4$) and is also strongly dependent on the fluid depth and the ray slope.

Incorporating these considerations, the theoretical far-field vertical ($w = \psi_x$) and horizontal ($u = -\psi_z$) components of velocity are

$$w(X, Z, t) = \frac{U}{\mu} \Re \left\{ \sum_{p=1}^{\infty} \gamma_p \, \kappa_p \sin pZ \, e^{i\,(p\kappa_p X - \omega_0 t + \pi/2)} \right\} \tag{3.1.71}$$

and

$$u(X, Z, t) = -U \Re \left\{ \sum_{p=1}^{\infty} \gamma_p \cos pZ \, e^{i\,(p\kappa_p X - \omega_0 t)} \right\}. \tag{3.1.72}$$

For small p and non-vanishing μ, $\gamma_p \kappa_p \simeq \gamma_p$, and thus the impact of viscosity on the vertical velocity in equation (3.1.71) is principally through the exponential term.

The factor κ_p corrects for the propagating wave field, but the generation remains inviscid, since the inviscid, no-normal flow boundary condition is applied at the boundary. This is widely regarded as an acceptable approximation because the viscous boundary condition is satisfied in the thin Stokes layer around the topography, which is $\sqrt{\nu}/\omega_0 = O(1)$mm . However, it also means that there remain singularities in the theoretical solution at the location of critical and supercritical wave generation.

3.2 Methods

3.2.1 Laboratory experiments

Laboratory experiments were performed using a Gaussian ridge with $h_0 = 0.098 \pm 0.001$ m and a maximal topographic slope of $45.0 \pm 1.5°$, cut out of a 2.05 m-long styrofoam block. The stratification was linear with buoyancy frequency $N = 1.03 \pm 0.04$rad/s. The channel

| ε | χ |

ε	0.004	0.008	0.017	0.042	0.084	0.150
0.57		✓				
0.70		✓		✓	✓	
1.00		✓				
1.73	✓	✓	✓	✓	✓	✓

Table 3.1: Criticality ε and excursion χ of the experiments performed.

depth far away from the ridge was $H = 0.196 \pm 0.001\,\mathrm{m}$, giving a depth ratio $h_0/H = 0.50 \pm 0.01$.

We investigated the internal wave field response to changes in criticality and excursion. Thus, the forcing frequency and amplitude of oscillation were systematically varied. Peak-to-peak amplitudes were in the range $1.0 \times 10^{-3}\,\mathrm{m} \le 2A \le 35.0 \times 10^{-3}\,\mathrm{m}$, corresponding to excursion parameters $0.004 \le \chi \le 0.147$. The frequency ω_0 was selected such that the wave beams propagated at angles to the horizontal in the range $30° \pm 1° \le \theta \le 60° \pm 2°$, corresponding to $0.57 \pm 0.05 \le \varepsilon \le 1.73 \pm 0.05$. Table 3.1 summarizes the variable parameters of the experiments performed.

The horizontal motion of the topography was ramped-up to a sinusoid over five periods of oscillation, in the manner specified by equation (2.1.5). Movies of the experimental wave fields for PIV processing were captured starting 3 minutes (approximately 20 periods) after the motion started. The frame rates were set at 16, 32 and 64 frames per internal wave period for experiments with $\chi \le 0.008$, $0.008 < \chi \le 0.084$ and $\chi = 0.147$, respectively, as needed to ensure that the particle displacements between images recorded by the PIV system were on the order of 10 pixels. In each experiment, 300 frames were recorded, so time series contained between 16 and 18 complete time periods for the experiments with a small excursion parameter. The field of view covered very nearly the entire vertical domain of the tank, the only absent region being layers less than 8 mm-thick at the top and bottom boundaries that were saturated by the laser intensity. The horizontal domain spanned at least a 10 cm-wide region within $0.17\,\mathrm{m} \le x \le 0.36\,\mathrm{m}$ in which the fluid depth was constant; $x = 0$ being the center of the topography.

Mode 1, which is the fastest propagating mode, traveled at $c_{g,1} = 5.6 \pm 0.3\,\mathrm{cm/s}$ (where $c_{g,p} = NH \cos^3 \theta / p\pi$ is the horizontal group velocity of mode p) and, in principle, had time to reach the end of the tank and reflect back into the field of view during an experiment.

The observed modal structure of wave fields before and after reflections could return into the field of view were consistent, however, demonstrating that the matting used to line the end-wall of the wave tank was effectively damping the reflections.

3.2.2 Numerical solution

The numerical experiments, performed by Professor Kraig Winters, solved two-dimensional, non-hydrostatic, non-linear equations of motion under the Boussinesq approximation:

$$\frac{\partial \mathbf{u}}{\partial t} + \mathbf{u} \cdot \nabla \mathbf{u} + \hat{k}\frac{g}{\rho_0}\rho = -\frac{1}{\rho_0}\nabla p + \nu\nabla^2\mathbf{u} + \mathcal{F}_D + i\mathcal{F}, \tag{3.2.1}$$

$$\frac{\partial \rho}{\partial t} + \mathbf{u} \cdot \nabla \rho = \kappa\nabla^2\rho, \tag{3.2.2}$$

$$\nabla \cdot \mathbf{u} = 0. \tag{3.2.3}$$

The viscosity ν and diffusivity κ were both set to $10^{-6}\,\mathrm{m^2/s}$. The barotropic tide was modeled via the body force $\mathcal{F}$ and a damping $\mathcal{F}_D$ was imposed at the ends of the horizontal domain.

The flow was solved in a domain $x = [-L/2, L/2]$ and $z = [-\Delta, H]$, where $L = 5\,\mathrm{m}$, $\Delta = 0.1H$ and $H = 19.70\,\mathrm{cm}$. A no-slip condition was imposed on the surface of the topography, and the non-physical flow below that surface was held stationary. The topography was set as a fixed Gaussian ridge with $h_0 = 9.80\,\mathrm{cm}$ and $\sigma = 5.94\,\mathrm{cm}$ to match the dimensions of the ridge used in the laboratory. A free-slip rigid lid condition was imposed on the upper boundary $z = H$. At the ends of the horizontal domain, all the derivatives with respect to x were set to zero. Furthermore, the damping term attenuated the amplitude of the perturbations near the boundaries to avoid reflections. For example, the damping term in the vertical momentum equation near $x = -L/2$ was

$$-e^{-(x+L/2)^2/\lambda^2}w(x, z, t)/T_D, \tag{3.2.4}$$

where the spatial and temporal scales of the damping were set using $\lambda = 5\sigma$ and $T_D = 0.1\mathrm{s}$, respectively.

The body force $\mathcal{F}$ was a sinusoidal with amplitudes and frequencies set to match the excursion and criticality of the laboratory experiments, and modulated with the same ramp-

	χ			
ε	0.008	0.042	0.084	0.168
0.57	✓			
0.70	✓	✓	✓	
1.00	✓			
1.73	✓	✓	✓	✓

Table 3.2: Criticality ε and excursion χ of the numerical wave fields.

up term introduced in equation 2.1.5. Table 3.2 summarizes the numerical wave fields generated for this study. Vertical velocity data for each of these wave fields was obtained over the entire computational domain and sub-sampled to match the spatial and temporal resolution of the laboratory experiments.

3.2.3 Analytical solution

The code of Pétrélis *et al.* [75] was used to solve equation (3.1.30) for $\gamma(Z)$ and evaluate the modal amplitudes γ_p in equation (3.1.32) that characterize the far-field wave fields generated by an isolated, two-dimensional Gaussian ridge,

$$z_T = \begin{cases} \frac{h_0}{1-e^{-8}} \left[\exp\left(-\frac{x^2}{2\sigma^2}\right) - e^{-8} \right] & |x| \leq 4\sigma \\ 0 & |x| > 4\sigma \end{cases}, \tag{3.2.5}$$

where the ridge height was set to $h_0 = 9.8$cm and

$$\sigma = \frac{h_0}{e^{1/2}\left(1 - e^{-8}\right)}, \tag{3.2.6}$$

so that the maximum topographic slope was $45°$. Thanks to the e^{-8} term, the height of this ridge continuously approaches zero at $|x| = 4\sigma$. The vertical velocity wave fields were reconstructed from γ_p using equation (3.1.71).

3.2.4 Modal decomposition

One can recover the mode strengths $\gamma_p = |\gamma_p|e^{i\Phi_p}$ from vertical profiles of flow variables, such as w profiles obtained using PIV. We define a phase function $\hat{\Phi}_p = \Phi_p + pX + \pi/2$ that incorporates the oscillatory dependance on X, $\Re(\kappa_p X) = pX$, and the $\pi/2$ phase shift of the vertical velocity signal as described in (3.1.71). Projecting the vertical velocity profile

76

onto the sinusoidal vertical basis modes of the linear stratification yields

$$I_p \equiv \int_0^\pi w \sin pZ \, \mathrm{d}Z = \left(\frac{\pi U}{2\mu}\right) |\gamma_p| e^{-pX \, \Im(\kappa_p)} \, \Re\{\kappa_p \, e^{i(\hat{\Phi}_p - \omega_0 t)}\} \qquad (3.2.7)$$

The integral I_p can be cross-correlated with a cosine signal in order to find the modal phase. Equation (3.2.7) is multiplied by $\cos(\Theta_p - \omega_0 t)$ and the value of Θ_p that maximizes the integral

$$\frac{2}{nT} \int_0^{nT} I_p \cos(\Theta_p - \omega_0 t) \, \mathrm{d}t \,, \qquad (3.2.8)$$

is chosen, where nT is the duration of n complete wave periods associated with the fundamental frequency, ω_0. The maximizing values of Θ_p give the phases, $\hat{\Phi}_p$, for the corresponding vertical modes. Equation (3.2.7) can then be solved for $|\gamma_p|$.

Equation (3.2.8) filters out harmonic internal waves of frequencies $n\omega_0$, for integer $n > 1$, which arise at the generation site ([52], [49]) and at points of wave beam intersection or reflection ([86], [74]). Although this filter does not remove inter-harmonic internal waves, for our small-amplitude experiments these were at least an order of magnitude smaller than the harmonic frequencies, as will be discussed in section 3.3, and so did not noticeably affect the data.

Thin layers at the top and bottom of the experimental images were inaccessible because of laser sheet reflections. The standard Fourier decomposition in equation (3.2.7) cannot be applied because the trigonometric basis functions are not orthogonal over the truncated vertical domain. Consequently, non-orthogonal Fourier series integrals are employed:

$$\int_{\pi\alpha/H}^{\pi(H-\beta)/H} w \sin pZ \, \mathrm{d}Z = \sum_{m=1}^\infty \Upsilon_{pm} \Gamma_m \,. \qquad (3.2.9)$$

Here α and β account for the regions of image loss near $z = 0$ and $z = H$, respectively, and the modal matrix Υ_{pm} is

$$\Upsilon_{pm} = \int_{\pi\alpha/H}^{\pi(H-\beta)/H} \sin pZ \sin mZ \, \mathrm{d}Z \,, \qquad (3.2.10)$$

leaving

$$\Gamma_m = \frac{U}{\mu} |\gamma_m| e^{-mX \, \Im(\kappa_m)} \, \Re\{\kappa_m \, e^{i(\hat{\Phi}_m - \omega_0 t)}\} \,. \qquad (3.2.11)$$

Equation (3.2.9) represents a system of p linear equations, which can be solved for $\{|\gamma_m|, \Phi_m\}$.
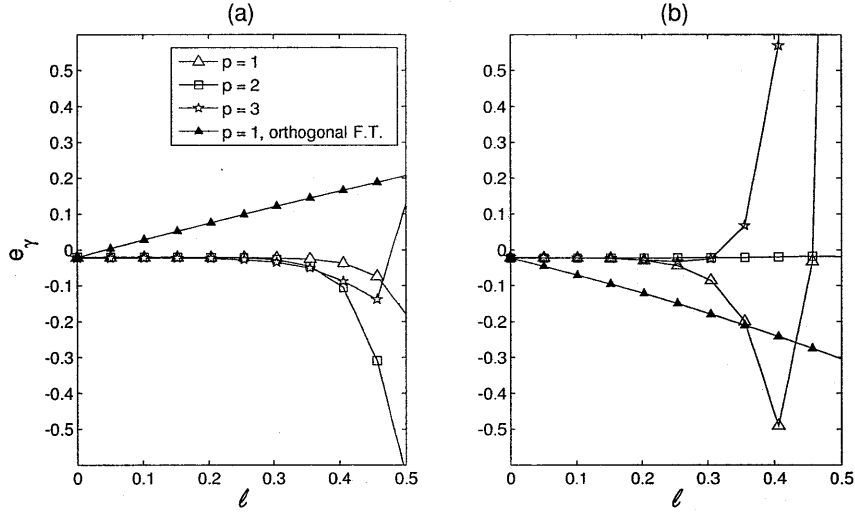
Figure 3-1: Error e_γ in $|\gamma_p|$ measurements for $p = 1$ (triangles), 2 (squares) and 3 (stars) due to image loss ℓ as a fraction of the channel depth H for representative conditions with $h_0/H = 0.497$ and $\varepsilon = 0.997$. Measurements using (a) w (vertical basis functions $\sin pZ$) and (b) u (vertical basis functions $\cos pZ$). Closed triangles correspond to the measurement error obtained for $|\gamma_1|$ if the image loss is ignored when performing the modal decomposition.

As Υ_{pm} is diagonally-dominant for reasonable choices of α and β, the infinite series in (3.2.9) was satisfactorily truncated after ten terms.

The sensitivity of the algorithm to image loss is explored in figure 3-1, which presents the error e_γ as a function of the image loss ℓ in measurements of $|\gamma_1|$, $|\gamma_2|$ and $|\gamma_3|$ from analytical wave fields cropped at the top and bottom. The error is given by

$$e_\gamma = (|\gamma_{p,\text{measured}}| - |\gamma_p|)/|\gamma_p|. \tag{3.2.12}$$

The image loss ℓ is given as a fraction of the channel depth H. Figure 3-1 also shows, for $p = 1$, the impact of ignoring image loss by disingenuously assuming $\sin pZ$ and $\sin mZ$ to be orthogonal over the truncated vertical integral, with lower and upper limits given, respectively, by $z = \pi \alpha/H$ and $z = \pi (H - \beta)/H$. The results presented here correspond to a configuration with $h_0/H = 0.497$ and $\varepsilon = 0.997$.

Contrasting the open and closed triangles in figure 3-1 indicates that employing the non-orthogonal Fourier series integral gives an excellent estimate for $|\gamma_1|$ with $e_\gamma \leq 2\%$ for

$\ell \le 20\%$, as compared to an error that increases linearly with ℓ if the orthogonal Fourier series integral is used. For the experiments of sections 3.3 and 3.4, the image loss was typically $\ell \le 4\%$. Similar comparisons can be made for $|\gamma_2|$ and $|\gamma_3|$. Comparing results for the vertical and horizontal components of velocity, it is observed that the impact of image loss is, in general, more acutely felt in the latter case. This result is to be expected from equation (3.1.71), which shows that w has $\sin(pZ)$ as its vertical basis functions, which disappear along the upper and lower boundaries. By contrast, equation (3.1.72) indicates that u has $\cos(pZ)$ as its vertical basis functions, which approach their extremal values at $z = 0, H$.

We choose to work with the vertical velocity field in estimating $\{|\gamma_p|, \Phi_p\}$ for $p = 1, 2, 3$. In principle, when laser sheet reflections are relatively small such that $\ell \lesssim 0.1$, it is observed from figure 3-1 that mode strengths can be satisfactorily resolved using either w or u. In practice, two additional physical effects observed in the laboratory have a more pronounced impact on u than w, again because of properties of the vertical basis functions. Firstly, the density gradients start diffusing at the upper and lower boundaries. Secondly, the flow must satisfy the no-slip boundary condition inside the Stokes layers at these boundaries. Supporting these comments, we observe that modal decompositions of experimental measurements of w offer more consistent results than modal decompositions of u. Since $w \to 0$ as the ray slope becomes horizontal, however, the signal-to-noise ratio was small in experiments with $\theta \lesssim 30°$, which restricted our ability to extract modal amplitudes for highly supercritical regimes.

As a standard procedure, we accepted only data for which consistent measurements of both $|\gamma_p|$ and Φ_p were obtained along the entire horizontal domain of the experiment, consistent with a mode propagating along and being only weakly damped by viscosity. Instances of inconsistent data were rare and did not arise in repeat experiments for linear internal waves and vertical modes $p = 1, 2$ and 3. On the other hand, it was difficult to obtain consistent results for $p \ge 4$ from both experiments and numerics. One reason for this is that, as discussed in section 3.1.3, viscous damping impacts high modes much more significantly than low modes. While this effect can be accounted for theoretically (e.g. by normalizing measured mode strengths by the viscous damping factor $e^{-p\Im[\kappa_p]X}$), this requires dividing by small quantities and leads to non-trivial absolute errors. In light of these observations and the conclusions of Di Lorenzo *et al.* [15] that "radiated energy is

[most] heavily concentrated" in the low vertical modes, we focused on the vertical modes $p = 1$, 2 and 3.

3.3 Direct comparison of experiments, numerics and theory

Figures 3-2(a) and (d) show, respectively, experimental velocity fields for subcritical ($\varepsilon = 0.70 \pm 0.04$) and supercritical ($\varepsilon = 1.73 \pm 0.05$) topographies with $\chi = 8.4 \times 10^{-3}$. The velocity fields are presented in the frame of reference in which the topography is stationary and the phase of tidal forcing $\Phi = 0°$, corresponding to the maximum tidal flow in the positive x-direction. Colors and arrows indicate, respectively, the magnitude and direction of the perturbation velocity field normalized by the far-field tidal velocity. Blank regions demarcate areas that were either outside of the camera's field of view or obscured by laser reflections. Figures 3-2(b) and (e) present the corresponding numerical wave fields, and figures 3-2(c) and (f) the corresponding far-field theoretical solutions (3.1.71) and (3.1.72). The experimental data was obtained in regions of constant depth away from the topography, and the analytical wave fields, which are reconstructed from the γ_p's defined for the far field, are shown for the same domain. The numerical snapshots are presented for a larger horizontal domain because the data was readily available.

For the subcritical case, illustrated in figures 3-2(a–c), away from the ridge a single dominant wave beam propagates to the right at an angle $\theta = 55° \pm 2°$. Near the ridge (figure 3-2(b)), we also see a left-propagating wave beam generated over the right-side slope. For the supercritical case illustrated in figures 3-2(d–f), a pair of internal wave beams propagate to the right and both up and down with $\theta = 30° \pm 1°$.

For both the sub- and supercritical cases, the form of the wave beams agrees for experiments, numerics and theory. The simulated wave fields are a little weaker than the experimental observations, however, and in the supercritical case the theoretical wave field is a little stronger. We attribute the latter to the fact that, despite the viscous correction of k_p, the theoretical supercritical solution generates a singular wave field at the critical slope; an aspect of the theory that is not present in the experiments or simulations. The present results are consistent with previous studies in which theory often slightly over-predicts the peak strength of wave beams as compared to experiments ([24], [89] and [73]).

In figure 3-3, we show vertical cross-sections of the vertical velocity w at locations I
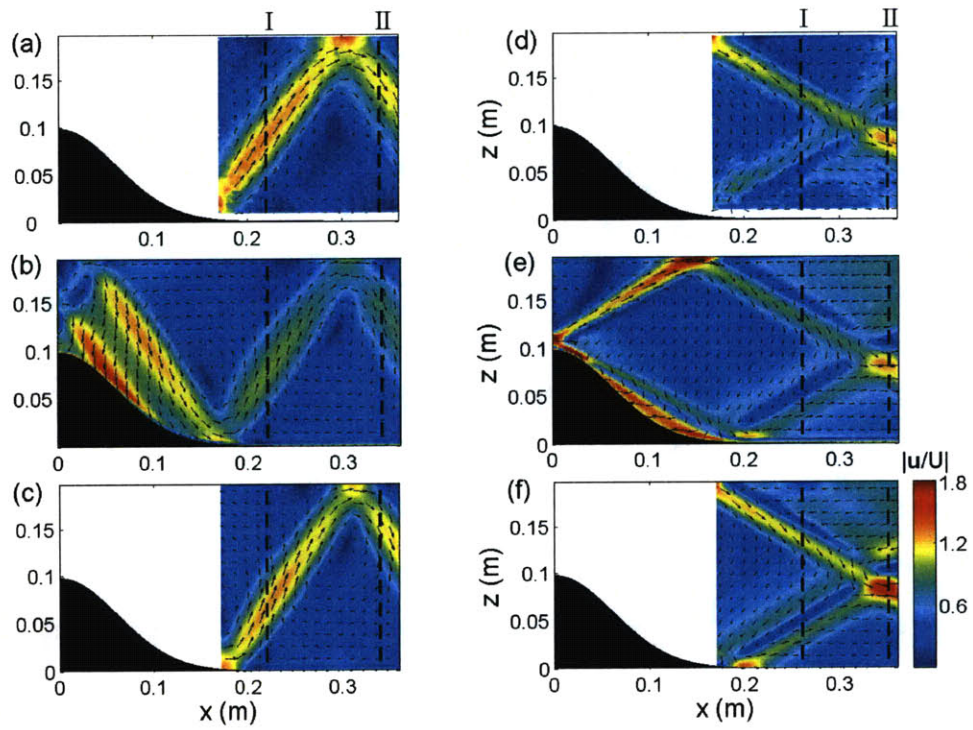
Figure 3-2: Snapshots of the velocity perturbation $\mathbf{u}/U$ to the far-field barotropic tide, with $\varepsilon = 0.70 \pm 0.04$ (a-c) and $\varepsilon = 1.73 \pm 0.05$ (d-f). Experimental, numerical and theoretical results are shown, respectively, in the top, middle and bottom rows. Colors and arrows indicate the instantaneous magnitude and direction of velocity. Locations I and II indicate vertical cross-sections where direct comparisons are made in figure 3-3.
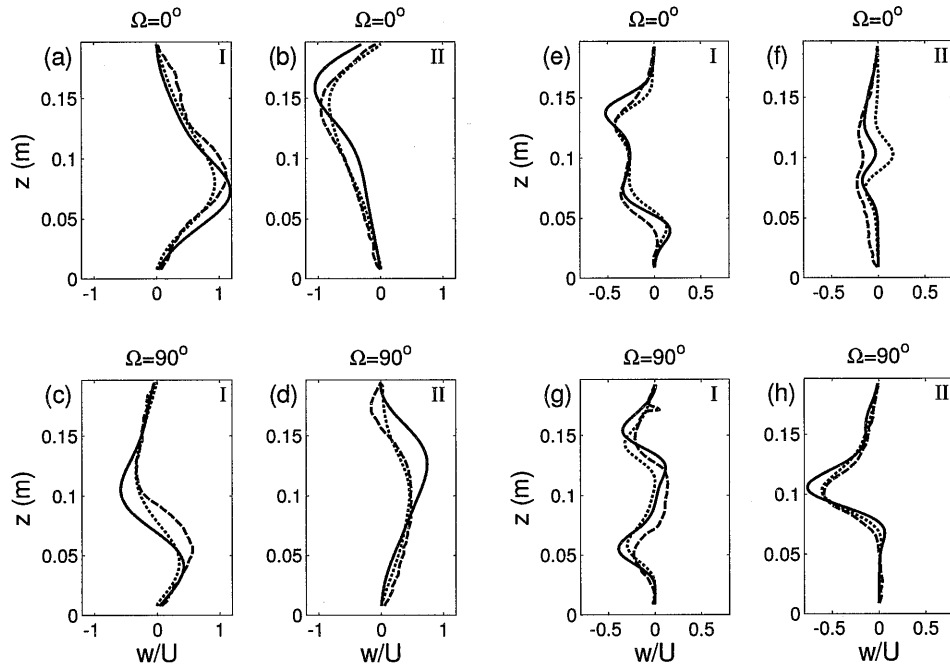
Figure 3-3: Cross-sections of the vertical velocity field, w/U, for $\varepsilon = 0.70 \pm 0.04$ (a–d) and $\varepsilon = 1.73 \pm 0.05$ (e–h). Panels in a column are taken at the same cross-section, respectively (from left to right): I and II for the subcritical wave field and I and II for the supercritical wave field. Cross-sections I and II are defined in figure 3-2. The lines correspond to the theoretical solution (solid), experimental data (dashed) and numerical data (dotted).

and II indicated in figure 3-2. These profiles are presented at two different phases of the tidal oscillation in figures 3-3(a–d) for the subcritical case; and in figures 3-3(e–h) for the supercritical case. The experimental profiles were averaged over 17 cycles to reduce the effect of experimental noise. Good agreement between the theory (solid curves), experiment (dashed curves) and numerics (dotted curves) is generally observed. The supercritical profiles, for example, are in particularly close agreement at $\Phi = 90°$ (figure 3-3(h)), with the theoretical peak a little stronger and sharper. In some other comparisons, however, the agreement is weaker. For the subcritical case at $\Phi = 90°$ (figure 3-3(c)), for example, theory predicts a strong downward flow at mid-depth, below which there is a quick reversal to an upward flow. In contrast, the experiments reveal a weaker downward flow at mid-depth, below which there is a stronger upward flow. The numerical results lie in between. Possible reasons for these discrepancies were investigated: (i) uncertainty in the phase of the experimental wave fields, which were sampled at 16 frames per cycle; and (ii) uncertainty in the criticality parameter and depth ratio of the experiments. None of these, however, could account for the observed errors. As shown in section 3.4, the discrepancies are associated with differences in the high-mode content of the wave field.

These spatial comparisons are complemented by temporal comparisons presented in figure 3-4. Figures 3-4(a–c) and (e–f) show experimental, numerical and theoretical time-series for the vertical velocity profiles at location I, for the sub- and supercritical experiments, respectively. The corresponding depth-averaged Fourier spectra of the experimental and the numerical data, obtained using either 17 or 18 tidal cycles, are presented in figures 3-4(d) and (h). Strong peaks are observed at the fundamental frequency, ω_0; where experiments and numerics agree to within 3.5% for the subcritical case and 2.7% for the supercritical case. Higher harmonics $2\omega_0$ and $3\omega_0$, which are evanescent for these experiments, are of relatively small amplitude, indicating that the wave field is dominated by waves of frequency ω_0 and can be reasonably considered linear.

3.4 Low-mode structure of the wave fields

3.4.1 Results for small excursion parameters

Figure 3-5 shows modal amplitudes and phases for $p = 1$, 2 and 3 as a function of ε for experiments (triangles) and numerics (circles). Horizontal error bars in the upper left corner
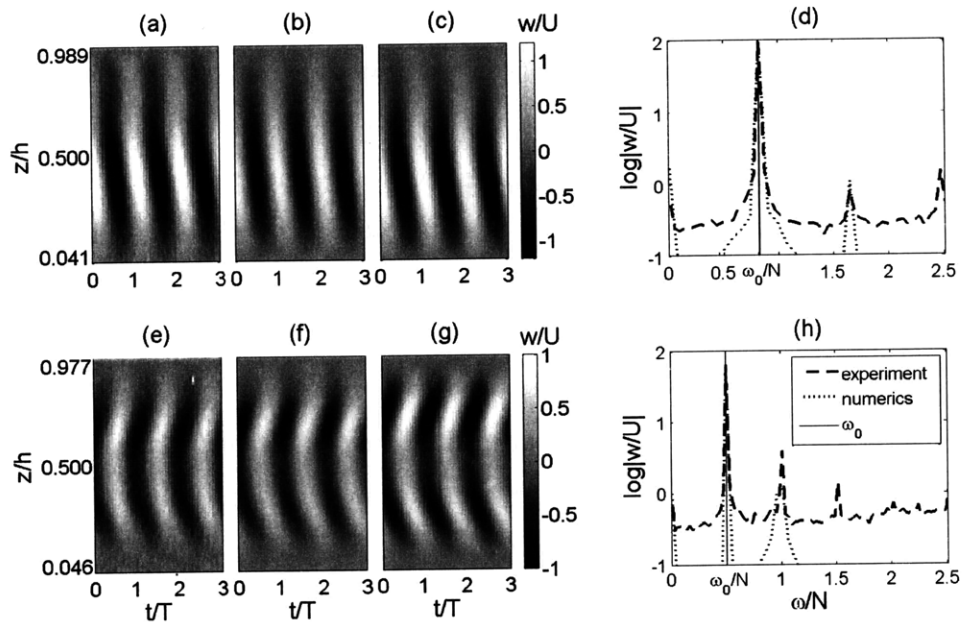
Figure 3-4: Vertical time-series and depth-averaged Fourier spectra of w/U at cross-section I (see figure 3-2). Time-series from (a) experiments, (b) simulations and (c) theory for $\varepsilon = 0.70 \pm 0.04$; and (d) corresponding depth-averaged spectra. Time-series from (e) experiments, (f) simulations and (g) theory for $\varepsilon = 1.73 \pm 0.05$; and (h) corresponding depth-averaged spectra.

reflect representative errors in ε for the laboratory experiments and vertical error bars reflect measurement variations in data obtained at 20 evenly-spaced horizontal locations (and in some cases multiple experiments), covering at least $0.10\,\mathrm{m}$ in the range $0.17\,\mathrm{m} \leq x \leq 0.36\,\mathrm{m}$. Superimposed are the theoretical solutions of Pétrélis et al. [75], the thin curves indicating the uncertainty in the depth ratio, to which supercritical modal amplitudes are quite sensitive. The theoretical curves are not, in general, smooth functions of ε because the system of linear equations resulting from the discretization of equation(3.1.30), whose solution specifies γ_p, contains a matrix that may become ill-conditioned for select choices of ε. The agreement between theory and experiment is good, almost always falling within the scale of the horizontal and vertical error bars. There is, furthermore, favorable agreement with results obtained from applying the modal decomposition algorithm to the numerical results. A couple of minor discrepancies exist: for example, Φ_1 is consistently higher for the numerical as compared to the theoretical and experimental data. On the other hand, there are cases where experiment and numerics closely agree on a result that is different from theory: for example, for $|\gamma_2|$ at the critical case $\varepsilon = 1.00 \pm 0.04$.

Figures 3-6 (a–c) respectively show the non-dimensional conversion rate given by equation (3.1.60) into mode 1 ($C_1^\star$), modes 1 and 2 ($C_{1+2}^\star$) and modes 1 though 3 ($C_{1+2+3}^\star$) as functions of ε. The energy conversion increases with ε, a trend that is supported by both the experimental (triangles) and numerical (circles) results. Most of the energy content is contained in mode 1. The agreement between measurement and theory is very good for wave fields over subcritical and critical topography, although there is a more noticeable discrepancy for the supercritical case that is associated with the differences in the amplitude of mode 1 reported in figure 3-5. Overall, the level of agreement is on a par with the analysis of Di Lorenzo et al. [15], who compared theoretical tidal conversion rates against the output of a hydrostatic Regional Ocean Modeling System (ROMS) simulation.

3.4.2 Results for large excursion parameters

While there is good agreement between experiment, theory and numerical simulation thus far, we find evidence of nonlinear effects even for small excursion parameters ($\chi \leq 1.68 \times 10^{-2}$). The frequency spectra in figures 3-4(d) and (h), for example, show higher-harmonics that are not accounted for by a linear model. Therefore, the excursion parameter was systematically increased by an order of magnitude or more to enhance nonlinearity in the

85
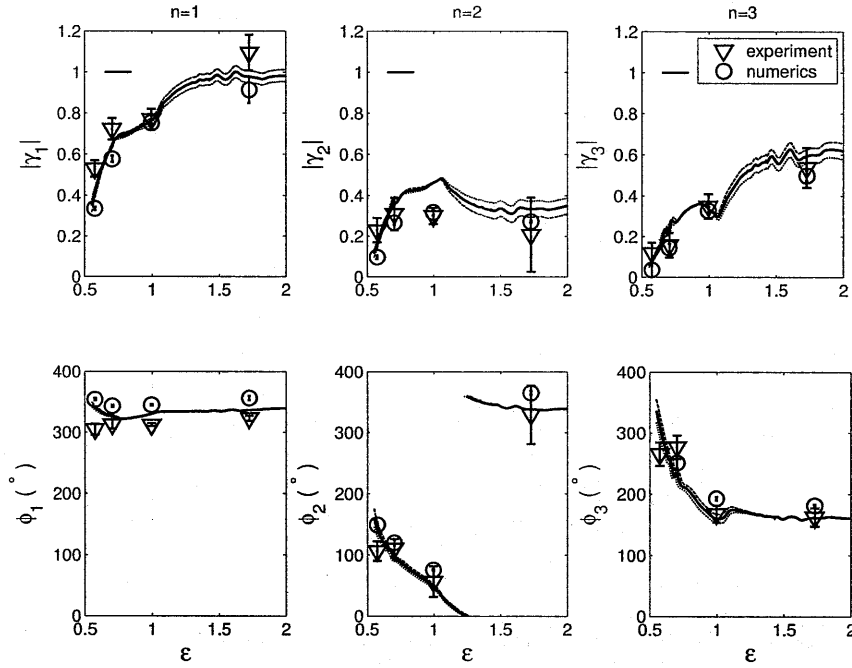
Figure 3-5: Modal amplitudes and phases for $p = 1, 2$ and 3 with $h_0/H = 0.50 \pm 0.01$ and $\chi \leq 1.68 \times 10^{-2}$. The theoretical solution is given by the dotted ($h_0/H = 0.49$), solid ($h_0/H = 0.50$) and dashed ($h_0/H = 0.51$) lines. The horizontal lines shown in the upper left hand corner of the top three panels indicate typical errors in ε.
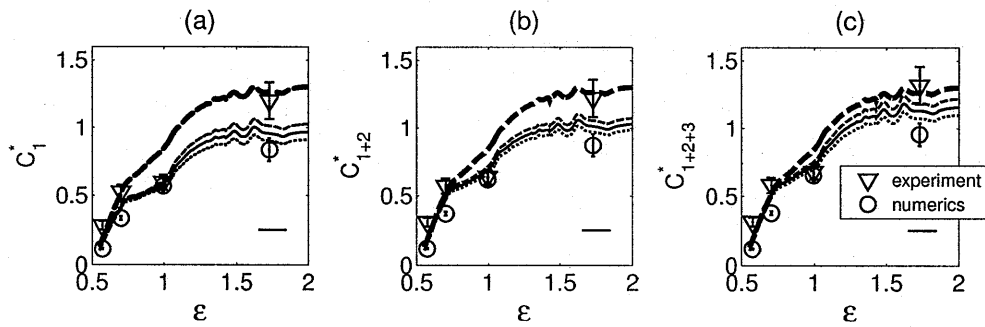
Figure 3-6: Non-dimensional conversion rate into low modes: (a) mode 1 ($C_1^\star$), (b) modes 1 and 2 ($C_{1+2}^\star$) and (c) modes 1 through 3 ($C_{1+2+3}^\star$) versus ε. The thin lines correspond to the model solution with $h_0/H = 0.49$ (dotted), $h_0/H = 0.50$ (solid) and $h_0/H = 0.51$ (dashed). The thick dashed line (which is identical in the three panels) shows the approximate total predicted energy conversion rate for $h_0/H = 0.50$, obtained by truncating the sum in equation (3.1.60) after 20 terms. Data points and error bars are as indicated in figure 3-5.
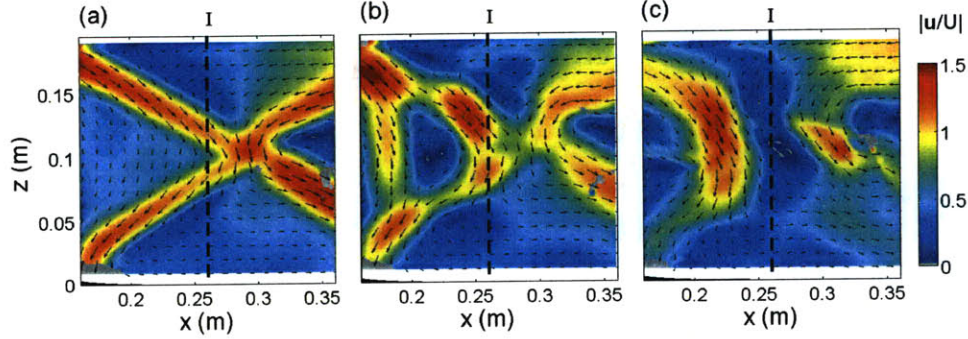
Figure 3-7: Experimental snapshots of the velocity perturbation $|\mathbf{u}/U|$ for $\varepsilon = 1.73 \pm 0.05$ and (a) $\chi = 0.042$, (b) $\chi = 0.084$, (c) $\chi = 0.147$.

experiments and simulations, in order to studied the impact on the radiated modal structure. Starting with $\chi = 0.0084$, for subcritical topography the excursion was increased to $\chi = 0.084$; and for supercritical topography the excursion was increased to $\chi = 0.168$. For these larger values of χ, the coherent far-field wave-beam pattern broke down, as shown in figure 3-7.

The signature of this nonlinear activity can be seen in the frequency content of the radiated wave field. Figure 3-8 presents depth-averaged Fourier spectra of the experimental and numerical vertical velocity fields at location I. For $\chi = 0.0084$, harmonic peaks are over an order of magnitude smaller than the peaks at the fundamental frequency. For $\chi = 0.084$, the relative magnitude of harmonic peaks increases significantly; for instance, the power at the first harmonic becomes almost half of the power at the fundamental frequency for the supercritical experiment. Note that all the harmonics are either evanescent or at best vertically propagating (i.e. the first harmonic for $\varepsilon = 1.73 \pm 0.05$), so they are confined to the neighborhood where they are generated. The spectra shown in figure 3-8, therefore, do not contain harmonics directly excited by the topography [10], but instead generated through nonlinearities, most likely at nearby wave beam reflections or crossings [86], [74], [52], [47]. The relative amplitude of the inter-harmonic content also increases with χ, although it remains weaker than the harmonic peaks. An interesting feature in the spectra of the numerical subcritical wave field is the presence of well defined sub- and inter-harmonic peaks. The sum of the frequencies of the two sub-harmonic peaks is equal to the fundamental frequency; and the frequencies of the inter-harmonic peaks are equal to either
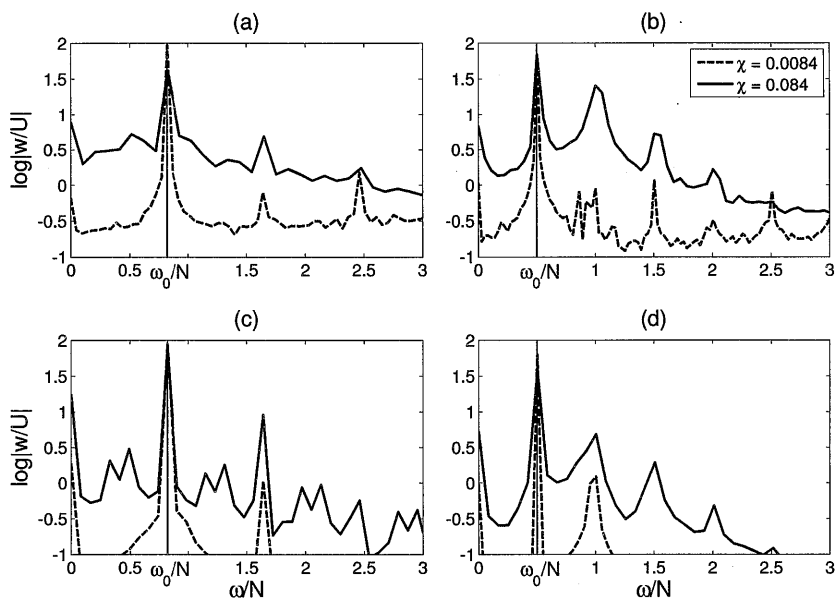
Figure 3-8: Depth-averaged Fourier spectra of w at location I in experiments with (a) $\varepsilon = 0.70 \pm 0.04$ and (b) $\varepsilon = 1.73 \pm 0.05$; results for the corresponding simulations are presented in (c) and (d). The lines show spectra for $\chi = 0.0084$ (dashed) and $\chi = 0.084$ (solid); as well as the location of ω_0/N (thin solid).

the fundamental or a harmonic frequency plus the frequency of one of the sub-harmonic peaks. Korobov and Lamb [47] also report on such 'self-similar' spectra, and attribute the sub-harmonic peaks to a sub-harmonic parametric instability and the inter-harmonic peaks to wave-wave interactions. These peaks are not present in the experimental data, however, which contains a smoother distribution of inter-harmonic content. However, the amplitude of the inter-harmonic content in the experiments is comparable to the amplitudes of the sub-harmonic peaks in the numerical wave field, suggesting that the signal to noise ratio for these intermediate frequencies is too low to confidently discuss the inter-harmonic frequency content of the experimental wave fields.

Figure 3-9 presents modal decomposition amplitude and phase results for the sub- and supercritical topography as a function of χ. We first consider the supercritical results in figures 3-9(b) and (d). Even up to the largest excursion parameter, the modal decomposition method measured a consistent mode-1 structure across the interrogation region from both experimental and numerical data, as indicated by the small error bars. There is a small decrease of $|\gamma_1|$ with χ (at most 10%, but typically a lot less) for excursion parameters
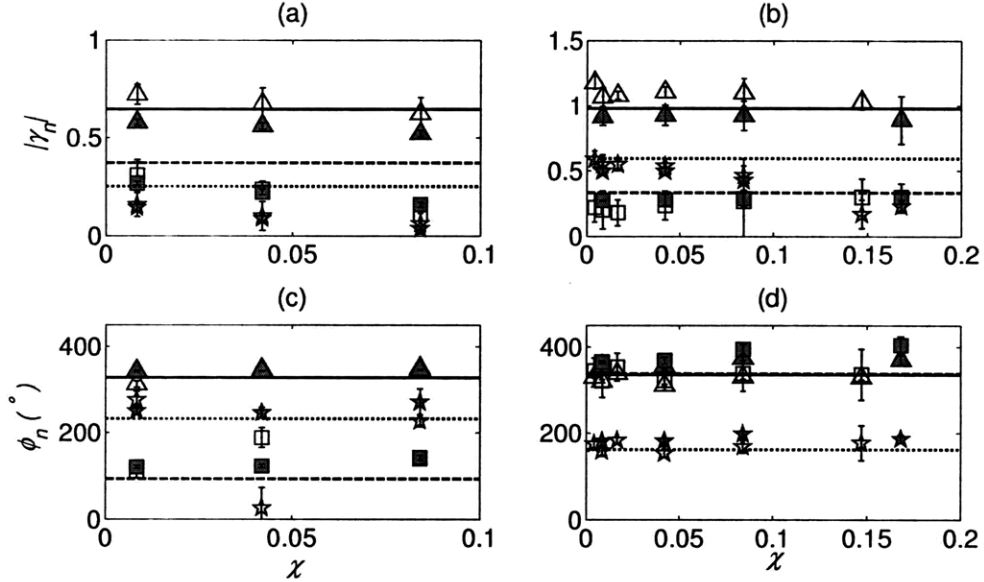
Figure 3-9: Variation of the modal decomposition results with χ for (a,c) $\varepsilon = 0.70 \pm 0.04$ and (b,d) $\varepsilon = 1.73 \pm 0.05$. Data point markers are as follows: $|\gamma_1|$, triangles; $|\gamma_2|$, squares; and $|\gamma_3|$, stars. Open and closed data points show experimental and numerical results, respectively. Horizontal lines show linear theoretical estimates for modes 1 (solid), 2 (dashed) and 3 (dotted).

approaching $\chi = 0.168$. The mode-1 phase, Φ_1, is also hardly affected. We were also able to reliably measure amplitudes and phases for modes 2 and 3. As with mode 1, an order of magnitude increase in χ yields little change in $|\gamma_2|$ or Φ_2. There is a more substantial variation ($\sim 50\%$) in $|\gamma_3|$, but $|\Phi_3|$ is not noticeably affected.

Results for subcritical topography, presented in figures 3-9(a) and (c), reveal a slightly more noticeable effect on $|\gamma_1|$; but even so, this decreases by only 10% in simulations and 15% in experiments. The measured amplitudes $|\gamma_2|$ and $|\gamma_3|$ also monotonically decrease with increasing excursion parameter. As with the supercritical results, for both experiments and numerical simulations the mode-1 phase is weakly influenced by the increasing excursion parameter, and agrees well with theory. There is some scatter in the phase measurements of modes 2 and 3 for $\chi = 0.042$. We repeated this particular experiment and observed the same result, showing it was robust, although notably different from numerics.

3.5 Discussion and contributions

This work constitutes the first laboratory investigations of internal tide generation by a two-dimensional ridge in a finite-depth and continuously-stratified ocean. As part of the investigation, a method was developed and implemented to extract modal amplitudes from experimental data, accounting for practical difficulties such as incomplete information in the vertical domain. This modal decomposition is a useful tool for characterizing the structure of an internal tide, and furthermore provides a means for estimating the linear energy flux. The results presented in section 3.3 and section 3.4.1 demonstrate good agreement between experiments, numerics and linear theory for the low-mode structure of internal tides generated by sub- and supercritical topography in the limit of a small excursion parameter.

For this geometry with a tall ridge, the wave field was dominated by mode 1. For a uniform stratification, mode 1 is associated with large spatial scales that are less vulnerable to small-scale instabilities. Therefore, for intermediate excursions up to 15%, the conversion rate was not strongly affected by the onset of nonlinearities. These results support the use of linear models for predicting tidal conversion rates even in transitional regimes with finite excursion parameter up to 15%, providing a useful guide for ocean modeling.

Small discrepancies do arise even in the linear regime, however. These are manifest as weak harmonics in the frequency spectra, and more obviously in comparisons of vertical velocity profiles, in figure 3-3. These discrepancies cannot be accounted for by the small uncertainties in the experimental parameters; this was checked by computing the analytical solution for values of ε and h_0/H within error ranges. The modal decomposition results reveal that the observed discrepancies are not associated with the low modes, for which there is agreement between experiment, theory and numerics. One conclusion, therefore, is that there is a mismatch of measured and predicted modes for $p \geq 4$, which are the modes responsible for the fine scale features of wave beams. This issue is difficult to probe in experiments because significant viscous damping of high modes prevents us from reliably extracting the corresponding modal amplitudes. Moreover, in critical and supercritical regimes linear theory is singular, which is unphysical. One remaining issue is the absence of a no-slip boundary condition in the analytical model. Although the effect of the viscous boundary should be constrained to an $O(1)$ mm thin layer at the boundaries, the fact that experimental profiles are in slightly closer agreement with the numerical profiles, which

account for one no-slip boundary (at the topography), suggests that viscous boundaries may somehow affect the higher modes throughout the domain. This would contribute to the discrepancies between the experimental and the analytical wave fields. We note that these small discrepancies in the comparisons have a minimal effect on the measured and predicted energy flux for the canonical topographic configuration considered (as shown in figure 3-6), consistent with observations by Di Lorenzo et al. [15] and Pétrélis et al. [75] that the high modes do not significantly impact the energy flux away from topography, which is dominated by the low modes, and principally by mode 1.

As the excursion increases to 15% of the width of the ridge, the coherent wave beam structure ultimately disappears. This is accompanied by a noticeable increase in the harmonic and inter-harmonic content of the wave field. Remarkably, this nonlinear activity has little impact on the amplitude and phase of the radiated mode-1 tide. There is a more noticeable effect for mode 2 and even more so for mode 3; namely, a steeper decrease in modal amplitude with excursion parameter, and some scatter in the phase of the subcritical experiments. This suggests that nonlinear processes first influence the medium-scale dynamics associated with the finer vertical scales of modes 2 and 3. All modal amplitudes decrease with increasing χ, indicating that the relative energy radiated by the internal tide at the fundamental frequency is reduced.

Since mode 1 transports most of the energy away from the topography, and its relative amplitude is little affected by increasing χ, we conclude that the energy radiated away from the topography in these experiments is not significantly influenced by nonlinear processes. This new insight reveals that the linear theory of Pétrélis et al. [75] reasonably predicts tidal conversion even for finite excursion parameters where nonlinearities start to become evident, and is useful for the parametrization of internal tide generation by topography with large depth ratios, such as Hawaii. On the other hand, for a small and narrow topographic features the internal tide response is dominated by higher modes, as reported by Legg and Huijts [52]. As such, in this "low-narrow" regime, we expect the influence of nonlinearities to be felt at comparably smaller excursion parameters.

There are, of course, differences between our experiments and the ocean; which must be considered when trying to extrapolate these results. For practical reasons we did not incorporate background rotation into the experiments, which usually plays a minimal role for most ocean generation problems, except near-critical latitudes where the parametric

subharmonic instability may be a first-order part of the response. We also accounted for the impact of viscous dissipation in the laboratory, which was negligible ($\sim 1\%$) for mode 1. Other notable differences, however, merit further discussion. One concerns the fact that higher harmonics in our system are either vertically-propagating or evanescent and therefore do not transport energy away from their point of generation. In contrast, in the ocean there is a multitude of propagating higher harmonics. We were unable to access this regime in our experiments due mainly to signal-to-noise issues at low beam angles. The lack of propagating harmonics in the experiments has the benefit, however, of being able to clearly identify whether the harmonics observed are generated directly by the topography [10], [49], or by wave-wave interactions away from the topography [74], [52]. We found significant harmonic content of the wave field that could only have been generated in the far field.

The investigation reported in this chapter concerns internal tide generation by a single, symmetric ridge in uniform stratification. This configuration provides a basis for the more general problem of tall ridges in the ocean, which can be of arbitrary shape and which exist in non-uniform stratifications. The next chapter builds on the analytical solution that has been used up to this point and generalizes it for topography of arbitrary shape and non-uniform stratifications.

Chapter 4

Double ridges

The linear theory of chapter 3 is extended here for internal tide generation by 2-D asymmetric and multiple ridges in non-uniform stratifications, which can represent internal tide generation sites in the ocean much more closely. First, an investigation using idealized topography is performed to show that the asymmetry and structure of a radiated tide can be very sensitive to the geometry of the site. Thereafter, the Hawaiian and the Luzon Strait ridges are used as case studies for realistic isolated and double-ridge systems. In order to do so, the modified linear theory is applied to 2-D cross-sections of the bathymetry using smoothed versions of the local stratification.

In section 4.1 the WKB approximation is reviewed, the Green function solution of chapter 3 is modified, and the numerical implementation of the solution is presented. The results of the modified theory are compared with previous analytical solutions in the respective parameter regimes in which these solutions are valid. Section 4.2 presents results for idealized 2-D topography in uniform stratifications, and section 4.3 presents results for 2-D cross-sections of the ridges at Hawaii and at the Luzon Strait, and furthermore compares these results to field observations and the predictions of ocean models. Section 4.4 is a discussion of the results of this investigation.

4.1 Modified linear theory

The theory of chapter 3 is modified such that it can be used directly with complicated topography and stratification data from real ocean situations. The WKB approximation is implemented to tackle non-uniform stratifications following Llewellyn Smith and Young [54]

and [55]. The other main modification concerns the definition of the boundary condition. The distribution of sources that model the presence of the topography is expressed as a function of the horizontal coordinate, $\gamma(X)$, as opposed to the vertical distribution $\gamma(Z)$, as was done in chapter 3. This approach was also used by Balmforth and Peacock [7], but in conjunction with assumptions of symmetry or periodicity that are not used here. Using $\gamma(X)$ allows a lot more flexibility in solving the problem of internal tide generation by rough, asymmetric topography and multiple ridge systems.

4.1.1 WKB approximation

This discussion of the application of the WKB approximation to internal wave propagation in non-uniform stratifications follows the notes of Gerkema [26]. We seek a propagating wave solution to the internal tide equation in a non-uniform stratification $N(z)$. The governing equation (1.2.33) for $\phi(x, z)$ now has a non-constant coefficient:

$$\left(\frac{N(z)^2 - \omega_0^2}{\omega_0^2 - f^2}\right) \frac{\partial^2 \phi}{\partial x^2} - \frac{\partial^2 \phi}{\partial z^2} = 0. \tag{4.1.1}$$

Assuming that the internal wavelength also varies in z, such that the form of the solution is most generally

$$\phi(x, z) = \phi_0 e^{i(kx + M(z))}, \tag{4.1.2}$$

and substituting (4.1.2) into (4.1.1), yields

$$M'(z)^2 - iM''(z) = k^2 \frac{N(z)^2 - \omega_0^2}{\omega_0^2 - f^2}. \tag{4.1.3}$$

We can define the local vertical wave number

$$m(z) \equiv M'(z). \tag{4.1.4}$$

In the case of a uniform stratification, the internal wave dispersion relation (1.2.31) determines the form of the vertical wave number m via

$$m^2 = k^2 \frac{N^2 - \omega_0^2}{\omega_0^2 - f^2}, \tag{4.1.5}$$

which is analogous to the right-hand side of equation (4.1.3). We can define $q(z)$ such that

$$q(z)^2 = k^2 \frac{N(z)^2 - \omega_0^2}{\omega_0^2 - f^2}, \tag{4.1.6}$$

which converges to m when N is constant. Therefore, for a slowly varying stratification, we assume that

$$m(z)^2 \approx q(z)^2. \tag{4.1.7}$$

By equation (4.1.3), the assumption in (4.1.7) is valid if $iM'' \ll M'^2$.

The first order approximation to $M(z)$:

$$M_1'(z)^2 \approx q(z)^2, \tag{4.1.8}$$

gives

$$M_1(z) \approx \int_0^z q(z_1) d(z_1). \tag{4.1.9}$$

The second order approximation is

$$M_2'(z)^2 \approx q(z)^2 + iM_1''(z) = q^2 + iq', \tag{4.1.10}$$

so

$$M_2'(z) \approx \pm q(1 \pm i \frac{q'}{q^2})^{1/2}. \tag{4.1.11}$$

Assuming that for a slowly varying stratification $q' \ll q^2$, then

$$M_2'(z) \approx \pm q \pm i \frac{q'}{2q}. \tag{4.1.12}$$

Integrating yields

$$M_2(z) \approx \pm \int_0^z q(z_1) d(z_1) + \frac{i}{2} \ln q. \tag{4.1.13}$$

The approximate WKB solution (4.1.2) can now be written as

$$\phi(x, z) \approx \frac{e^{ikx}}{\sqrt{q(z)}} \left[K_- e^{-i \int_0^z q(z_1) dz_1} + K_+ e^{i \int_0^z q(z_1) dz_1} \right], \tag{4.1.14}$$

where K_- and K_+ are arbitrary constant coefficients.

The main assumption, which was applied to obtain equation (4.1.12), is that $q' \ll q^2$.

(The other assumption used, $iM'' \ll M'^2$, is equivalent to $q' \ll q^2$ for the first order expression for M.) From equation (4.1.6), the left-hand side of the inequality is proportional to the variation of the stratification, $N'(z)$, and the right-hand side is inversely proportional to the vertical internal wavelength, with N as the constant of proportionality:

$$N' \ll Nq. \qquad (4.1.15)$$

This is most accurate for high mode numbers, but is qualitatively correct even for the longest wavelength solutions [54].

4.1.2 Green function solution

We define a new equation for the Green function,

$$\left(\frac{N(z)^2 - \omega_0^2}{\omega_0^2 - f^2} \right) G_{xx} - G_{zz} = \delta(x - x')\delta(z - z'), \qquad (4.1.16)$$

subject to the radiation condition in x, such that internal waves propagate away from x', and to homogeneous boundary conditions in z:

$$G(x, x'; 0, z') = G(x, x'; H, z') = 0. \qquad (4.1.17)$$

The WKB solution (4.1.14) solves equation (4.1.16) away from the singularity at (x', z'), so the approximate Green function is:

$$G(|x - x'|; z, z') \approx \frac{1}{\sqrt{q(z)}} e^{ik|x-x'|} \left[K_-(z')e^{-i\int_0^z dz_1 q(z_1)} + K_+(z')e^{i\int_0^z dz_1 q(z_1)} \right]. \qquad (4.1.18)$$

Making equation (4.1.18) an explicit function of $|x - x'|$ ensures that the radiation condition is satisfied because, as is discussed for equation (3.1.13), the waves associated with this spatial structure always propagate away from x'.

We first impose the boundary conditions (4.1.17), which determine that

$$K^- = -K^+ \qquad (4.1.19)$$

96

and

$$\sin \left(\int_0^H q(z_1)dz_1 \right) = 0. \tag{4.1.20}$$

Equation (4.1.20) suggests that the wave field has a modal structure. In particular, one can define a parameter

$$\bar{N} = \frac{1}{H} \int_0^H \sqrt{N(z)^2 - \omega_0^2}dz \tag{4.1.21}$$

such that the argument of (4.1.20) is

$$\int_0^H q(z_1)dz_1 = \frac{kH\bar{N}}{\sqrt{\omega_0^2 - f^2}}, \tag{4.1.22}$$

and, since

$$\sin \left(\frac{kH\bar{N}}{\sqrt{\omega_0^2 - f^2}} \right) = 0 \tag{4.1.23}$$

is true if

$$\frac{kH\bar{N}}{\sqrt{\omega_0^2 - f^2}} = n\pi \tag{4.1.24}$$

for some integer n, then the possible horizontal wave numbers are discrete:

$$k = k_n = \frac{n\pi\sqrt{\omega_0^2 - f^2}}{H\bar{N}}. \tag{4.1.25}$$

Before incorporating equation (4.1.25) into the expression for the Green function, it is convenient to simplify the z-dependance of equation (4.1.18). We define a stretched vertical coordinate

$$Z(z) = \frac{\pi}{H\bar{N}} \int_0^z \sqrt{N(z_1)^2 - \omega_0^2}dz_1, \tag{4.1.26}$$

so that

$$\int_0^z q(z_1)dz_1 = \frac{k_n}{\sqrt{\omega_0^2 - f^2}} \int_0^z \sqrt{N(z_1)^2 - \omega_0^2}dz_1 = nZ, \tag{4.1.27}$$

and the z-dependant quantity

$$\mathcal{N}(z) = \frac{1}{\bar{N}} \sqrt{N(z)^2 - \omega_0^2}. \tag{4.1.28}$$

The corresponding dimensionless horizontal coordinate is

$$X = \frac{x\pi}{\mu H}, \tag{4.1.29}$$

97

where

$$\mu = \frac{\bar{N}}{\sqrt{\omega_0^2 - f^2}}.$$

(4.1.30)

However, we refrain from expressing the Green function solely in terms of X and Z until we have found an expression for $K_n(z')$ in the solution (4.1.18). In terms of the quantities defined above, the Green function becomes

$$G(|x - x'|; z, z') = \sum_{n=1}^{\infty} \sqrt{\frac{H}{n\pi}} e^{\frac{in\pi}{\mu H}|x-x'|} K_n(z') \frac{\sin nZ(z)}{\sqrt{\mathcal{N}(z)}}.$$

(4.1.31)

In the presence of a non-uniform stratification, the shape of the nth vertical mode is no longer a perfect sinusoid, but rather

$$\frac{\sin nZ(z)}{\sqrt{\mathcal{N}(z)}}.$$

(4.1.32)

We use this observation with the additional condition that the Green function must satisfy equation (4.1.16) around the singularity at (x', z') to find $K_n(z')$. Projecting (4.1.16) onto the vertical modes,

$$\int_0^H (4.1.16) \times \frac{\sin pZ(z)}{\sqrt{\mathcal{N}(z)}} dz,$$

(4.1.33)

yields

$$\int_0^H dz \sum_{n=1}^{\infty} K_n(z') \sqrt{\frac{H}{n\pi}} \frac{\sin nZ(z) \sin pZ(z)}{\mathcal{N}(z)} \frac{N(z)^2 - \omega_0^2}{\omega_0^2 - f^2} \frac{\partial^2}{\partial x^2} \left(e^{\frac{in\pi}{\mu H}|x-x'|} \right)$$

$$- \int_0^H dz \sum_{n=1}^{\infty} K_n(z') \sqrt{\frac{H}{n\pi}} e^{\frac{in\pi}{\mu H}|x-x'|} \frac{\sin pZ(z)}{\sqrt{\mathcal{N}(z)}} \frac{\partial^2}{\partial z^2} \left(\frac{\sin nZ(z)}{\sqrt{\mathcal{N}(z)}} \right)$$

$$= \partial(x - x') \frac{\sin pZ(z')}{\sqrt{\mathcal{N}(z')}}$$

(4.1.34)

.

Equation (4.1.34) is then integrated across the singularity at x', i.e.

$$\int_{x'-\varepsilon}^{x'+\varepsilon} (4.1.34) dx.$$

(4.1.35)

In the limit $\varepsilon \to 0$, the integral of the second term on the left-hand side of (4.1.34) approaches zero. For the remaining term, the order of integration and summation is exchanged and

$\mathcal{N}(z)$ is expressed in terms of $N(z)$:

$$\frac{\bar{N}}{\omega_0^2 - f^2} \sum_{n=1}^{\infty} K_n(z') \sqrt{\frac{H}{n\pi}} \int_0^H \sin nZ(z) \sin pZ(z) \sqrt{N(z)^2 - \omega_0^2} dz \frac{\partial}{\partial x} \left(e^{\frac{in\pi\omega_0}{HN}|x-x'|} \right) \Big|_{x'-\varepsilon}^{x'+\varepsilon}$$

$$= \frac{\sin pZ(z')}{\sqrt{\mathcal{N}(z')}}. \tag{4.1.36}$$

We proceed to evaluate:

$$\lim_{\varepsilon \to 0} \left[\frac{\partial}{\partial x} \left(e^{\frac{in\pi}{\mu H}|x-x'|} \right) \Big|_{x'-\varepsilon}^{x'+\varepsilon} \right] = \frac{in\pi}{\mu H} \mathrm{sign}(x - x') \lim_{\varepsilon \to 0} \left[e^{\frac{in\pi}{\mu H}|x-x'|} \Big|_{x'-\varepsilon}^{x'+\varepsilon} \right]$$

$$= \frac{in\pi}{\mu H} \lim_{\varepsilon \to 0} \left[e^{\frac{in\pi}{\mu H}\varepsilon} - -e^{-\frac{in\pi}{\mu H}\varepsilon} \right]$$

$$= \frac{2in\pi}{\mu H}. \tag{4.1.37}$$

Finally, we change the integration variable from z to Z using the derivative of the definition (4.1.26):

$$dz = \frac{H\bar{N}dZ}{\pi\sqrt{N(z)^2 - \omega_0^2}}. \tag{4.1.38}$$

Thus, (4.1.36) becomes

$$2i\mu \sum_{n=1}^{\infty} \sqrt{\frac{nH}{\pi}} K_n(z') \int_0^\pi dZ \sin nZ(z) \sin pZ(z) = \frac{\sin pZ(z')}{\sqrt{\mathcal{N}(z')}}. \tag{4.1.39}$$

The integral is non-zero only when $n = p$, so

$$2i\mu \sqrt{\frac{pH}{\pi}} K_p(z') \frac{\pi}{2} = \frac{\sin pZ(z')}{\sqrt{\mathcal{N}(z')}}, \tag{4.1.40}$$

and finally

$$K_p(z') = \frac{-i}{\mu\sqrt{p\pi H}} \frac{\sin pZ(z')}{\sqrt{\mathcal{N}(z')}}. \tag{4.1.41}$$

The functional form of $K_p(z')$ can now be substituted into equation (4.1.31) and the Green function expressed in terms of the dimensionless X and Z:

$$G(|X - X'|; Z, Z') = \sum_{p=1}^{\infty} \frac{\sin pZ'}{\sqrt{\mathcal{N}(R(Z'))}} \frac{\sin pZ}{\sqrt{\mathcal{N}(R(Z))}} e^{ip|X-X'|}, \tag{4.1.42}$$

where $z = R(Z)$, such that R inverts the nonlinear mapping in (4.1.26). A distribution of singularities $\gamma(X)$ along the non-dimensional topography $\hat{h}(X) = \pi h(x)/H$ is used to

account for internal tide generation. The wave field is represented by

$$\phi(X, Z) = \frac{H}{\pi} \int_{-a}^{b} \gamma(X')G(|X - X'|; Z, \hat{h}(X'))dX', \qquad (4.1.43)$$

where it is assumed that the topography is of arbitrary shape within $X \in [-a, b]$ and of zero height elsewhere. Note that the constant factor of $K_p(Z')$ in (4.1.41) is implicitly accounted for in $\gamma(X)$. The solution (4.1.43) differs from that of Pétrélis $et\ al.$ [75] as it considers a horizontally, rather than vertically, distributed array of sources (i.e. $\gamma(X)$ instead of $\gamma(Z)$), which is the key to straightforwardly handling problems with complicated topography. The desired quantity $\gamma(X)$ is found by imposing the bottom boundary condition (1.2.36) and solving the following integral equation numerically, as outlined in section 4.1.4:

$$h(X) = \frac{H}{\pi} \int_{-a}^{b} \gamma(X')G(|X - X'|; \hat{h}(X), \hat{h}(X'))dX'. \qquad (4.1.44)$$

In the far field, where $X < -a$ or $X > b$, one can define:

$$\gamma_p^{\pm} = \frac{1}{\pi} \int_{-a}^{b} \gamma(X') \frac{\sin(p\hat{h}(X'))}{\sqrt{\mathcal{N}(h(X'))}} e^{\mp ipX'} dX', \qquad (4.1.45)$$

where

$$\hat{h}(X') = \frac{\pi}{H\bar{N}} \int_{0}^{h(X)} \sqrt{N(z_1)^2 - \omega_0^2} dz_1, \qquad (4.1.46)$$

and the superscript of $\gamma_p^{\pm}$ indicates left- ('−') and right- ('+') going waves, respectively. A modal form is given for the far field solution by expressing (4.1.43) in terms of $\gamma_p^{\pm}$:

$$\phi^{\pm}(X, Z) = \frac{H}{\pi} \sum_{p=1}^{\infty} \frac{\gamma_p^{\pm}}{p} \frac{\sin pZ}{\sqrt{\mathcal{N}(R(Z))}} e^{\pm ipX}. \qquad (4.1.47)$$

4.1.3   Conversion rate

The conversion rate C is evaluated using the equivalent expression for the depth-integrated radiated energy flux introduced in chapter 3 (equation (3.1.56)):

$$C = \int_{0}^{H} <p_z\psi> dz = -i\rho_* U^2 \int_{0}^{H} \frac{N(z)^2 - \omega_0^2}{4\omega_0} (\phi\phi_x^* - \phi^*\phi_x) dz. \qquad (4.1.48)$$

Substituting the expression for ϕ in terms of γ_p from (4.1.47) into (4.1.48) yields two terms in the integrand:

$$C = \frac{-i\rho_* U^2}{4\omega_0} \int_0^H \left(\frac{iH}{\mu\pi} \right) (I_1(z) + I_2(z)) \, dz, \qquad (4.1.49)$$

where

$$I_1(z) = (N(z)^2 - \omega_0^2) \sum_{p=1}^{\infty} \sum_{q=1}^{\infty} \frac{\gamma_p \gamma_q^*}{p} \frac{\sin pZ(z) \sin qZ(z)}{\mathcal{N}(z)} e^{i(q-p)\frac{x\pi}{\mu H}} \qquad (4.1.50)$$

and

$$I_2(z) = (N(z)^2 - \omega_0^2) \sum_{p=1}^{\infty} \sum_{q=1}^{\infty} \frac{\gamma_p^* \gamma_q}{q} \frac{\sin pZ(z) \sin qZ(z)}{\mathcal{N}(z)} e^{-i(q-p)\frac{x\pi}{\mu H}}. \qquad (4.1.51)$$

Exchanging the order of integration and summation reveals that the same integration is performed for both terms. In particular, having expressed $\mathcal{N}(z)$ in terms of $N(z)$, the integral of (4.1.51) is:

$$\bar{N} \int_0^H \frac{(N(z)^2 - \omega_0^2) \sin pZ \sin qZ}{\sqrt{N(z)^2 - \omega_0^2}} \, dz. \qquad (4.1.52)$$

Changing the integration variable to Z, as was done earlier, cancels out the $\sqrt{N(z)^2 - \omega_0^2}$ term in (4.1.52) and the integral becomes

$$\frac{H\bar{N}^2}{\pi} \int_0^\pi \sin pZ \sin qZ \, dZ = \frac{H\bar{N}^2 \delta_{p,q}}{2}. \qquad (4.1.53)$$

The terms I_1 and I_2 become

$$I_1 = I_2 = \frac{H\bar{N}^2}{2} \sum_{p=1}^{\infty} \frac{|\gamma_p|^2}{p}, \qquad (4.1.54)$$

and finally

$$C^{\pm} = \pm \frac{\rho_* U^2 H^2 \bar{N}^2}{4\pi\mu\omega} \sum_p^{\infty} \frac{|\gamma_p^{\pm}|^2}{p} = \pm \frac{\rho_* U^2 H^2 \bar{N}^2}{4\pi\mu\omega} C_*^{\pm}, \qquad (4.1.55)$$

where $C_*^{\pm} = \sum_p^{\infty} |\gamma_p^{\pm}|^2/p$ is the non-dimensional conversion rate. A related quantity that is used in the upcoming discussion is the fraction of the far-field conversion in the first p modes:

$$F_p^{\pm} = \frac{1}{C_{\pm}^*} \sum_{n=1}^{p} \frac{|\gamma_n^{\pm}|^2}{n}. \qquad (4.1.56)$$

101

4.1.4 Implementation

For the investigation in the following sections, equation (4.1.44) was solved numerically in MATLAB in a manner similar to the approach in the appendix of by Pétrélis et al. [75]. Substituting (4.1.42) and (4.1.43) into the boundary condition (4.1.44) and exchanging the order of summation and integration yields:

$$\frac{\pi h(X)}{H} = \sum_{p=1}^{\infty} \frac{1}{p\pi} \frac{\sin\left(p\hat{h}(X)\right)}{\sqrt{\mathcal{N}(h(X))}} \int_{-a}^{b} \gamma(X') \frac{\sin\left(p\hat{h}(X')\right)}{\sqrt{\mathcal{N}(h(X'))}} e^{ip|X-X'|} dX'. \tag{4.1.57}$$

To solve (4.1.57) for $\gamma(X)$, the domain $X \in [-a : b]$ is discretized into $K-1$ intervals so that $X_1 = -a$ and $X_K = b$. Functions of X are approximated as constants over the small intervals $\Delta X = X_{n+1} - X_n$, such that:

$$\int_{X_n}^{X_{n+1}} h(X) dX = h_{n+1/2} \Delta X \tag{4.1.58}$$

and

$$\int_{X_n}^{X_{n+1}} \gamma(X) dX = \gamma_{n+1/2} \Delta X, \tag{4.1.59}$$

where the notation $n + 1/2$ indicates a mid-point value. Therefore, integrating (4.1.57) in an interval $[x_n : x_{n+1}]$ yields:

$$\frac{\pi h_{n+1/2}}{H} \Delta X \approx \sum_{p=1}^{\infty} \frac{1}{p\pi} \int_{X_n}^{X_{n+1}} \int_{-a}^{b} \frac{\sin\left(p\hat{h}(X)\right)}{\sqrt{\mathcal{N}(h(X))}} \frac{\sin\left(p\hat{h}(X')\right)}{\sqrt{\mathcal{N}(h(X'))}} e^{ip|X-X'|} \gamma(X') dX' dX. \tag{4.1.60}$$

The inner integral can be written as a sum of integrals over each discrete interval:

$$\frac{\pi h_{n+1/2}}{H} \Delta X \approx \sum_{p=1}^{\infty} \frac{1}{p\pi} \int_{X_n}^{X_{n+1}} \sum_{j=1}^{K-1} \gamma_{j+1/2} \int_{X_j}^{X_{j+1}} \frac{\sin\left(p\hat{h}(X)\right)}{\sqrt{\mathcal{N}(h(X))}} \frac{\sin\left(p\hat{h}(X')\right)}{\sqrt{\mathcal{N}(h(X'))}} e^{ip|X-X'|} dX dX', \tag{4.1.61}$$

and this can be expressed compactly as a linear problem

$$\frac{\pi h_{n+1/2}}{H} \Delta X = \sum_{j=1}^{K-1} M_{nj} \gamma_{j+1/2}, \tag{4.1.62}$$

102

where

$$M_{nj} = \sum_{p=1}^{\infty} \frac{1}{p\pi} \int_{X_n}^{X_{n+1}} \int_{X_j}^{X_{j+1}} \frac{\sin(p\hat{h}(X))}{\sqrt{\mathcal{N}(h(X))}} \frac{\sin(p\hat{h}(X'))}{\sqrt{\mathcal{N}(h(X'))}} e^{ip|X-X'|} dX dX'. \qquad (4.1.63)$$

The task of evaluating M_{nj} can be simplified. Firstly, the matrix M is symmetric,

$$M_{nj} = M_{jn}. \qquad (4.1.64)$$

Secondly, for $X > X'$, M_{nj} can be re-written as

$$M_{nj} = \sum_{p=1}^{\infty} \frac{1}{p\pi} \int_{X_n}^{X_{n+1}} \frac{\sin(p\hat{h}(X))}{\sqrt{\mathcal{N}(h(X))}} e^{ipX} dX \int_{X_j}^{X_{j+1}} \frac{\sin(p\hat{h}(X'))}{\sqrt{\mathcal{N}(h(X'))}} e^{-ipX'} dX'. \qquad (4.1.65)$$

Defining

$$U_n(p) = \int_{X_n}^{X_{n+1}} \frac{\sin(p\hat{h}(X'))}{\sqrt{\mathcal{N}(h(X'))}} e^{ipX'} dX', \qquad (4.1.66)$$

then, for $n \geq j + 1$,

$$M_{nj} = \frac{1}{\pi} \sum_{p=1}^{\infty} \frac{U_n(p) U_j^*(p)}{p}. \qquad (4.1.67)$$

Similarly, for $X < X'$ (i.e. $n + 1 \leq j$)

$$M_{nj} = \frac{1}{\pi} \sum_{p=1}^{\infty} \frac{U_n^*(p) U_j(p)}{p}. \qquad (4.1.68)$$

Therefore, evaluating $U_n(p)$ is enough to evaluate M_{nj} for $n \neq m$. In practice, the summation in equations (4.1.67) and (4.1.68) is truncated at some large value $p = P$. The expression for M_{nn} is more complicated, and it is found using symbolic math in MATLAB. For convenience, we first define the slope $s = d\hat{h}/dX$, and the following variables:

$$t_1 = 2p\hat{h}_{1/2} + ps_{1/2}\Delta X, \qquad (4.1.69)$$

and

$$t_2 = ps_{1/2}\Delta X - 2p\hat{h}_{1/2}, \qquad (4.1.70)$$

where the subscript $1/2$ is used as short-hand notation for $n + 1/2$. The diagonal elements

103

of the matrix can be found using

$$M_{nn} = \sum_{p=1}^{\infty} \frac{2(1 - s_{1/2}^2)^2}{p^3 \pi \mathcal{N}(h_{1/2}) s_{1/2}} [A + B + C + D + E], \qquad (4.1.71)$$

where

$$A = 2s_{1/2} \left[ip\Delta X (1 - s_{1/2}^2) + 1 + s_{1/2}^2 \right], \qquad (4.1.72)$$

$$B = \left[i \sin t_1 + s_{1/2} \cos t_1 \right] (1 - s_{1/2}^2), \qquad (4.1.73)$$

$$C = 4is_{1/2}^2 e^{ip\Delta X} \sin(ps_{1/2}\Delta X), \qquad (4.1.74)$$

$$D = 2s_{1/2} e^{ip\Delta X} \left[\cos(2p\hat{h}_{1/2})(1 - s_{1/2}^2) - (1 + s_{1/2}^2) \cos(ps_{1/2}\Delta X) \right] \qquad (4.1.75)$$

and

$$E = \left[i \sin t_2 + s_{1/2} \cos t_2 \right] (s_{1/2}^2 - 1). \qquad (4.1.76)$$

The parameters K and P, which determine the numerical resolution of the solution, are chosen to ensure that the solution converges. Convergence is taken to be satisfactory when there is a negligible difference in $\gamma(X)$ as K and P are doubled.

4.1.5 Comparisons with previous solutions

Numerous checks were performed to confirm that the approach and numerical solution method previously presented were in agreement with existing solutions of internal tide generation over topography that have been developed previously for specific parameter regimes, including sub- and supercritical topography, semi-infinite and finite-depth channels, and uniform as well as weakly non-uniform stratifications.

Figure 4-1 shows a comparison to the solution of Pétrélis *et al.* [75] for sub- and supercritical, isolated symmetric Gaussian ridges in a finite-depth channel. The first comparison concerns the internal tide generated over a Gaussian ridge with a maximum slope of 45° and a depth ratio $h/H = 0.5$, which is the same configuration used in the investigations of chapter 3. Internal wave beams propagate at $\theta = 60°$ to the horizontal, corresponding to a criticality parameter $\varepsilon = 0.58$. Figures 4-1(a) and (b) present snapshots of the normalized vertical velocity fields w/U at a phase $\Phi = 0$ and evaluated assuming a distribution of sources $\gamma(X)$ and $\gamma(Z)$, respectively. The Green functions were evaluated by summing 25

modes in equations (4.1.42) and (3.1.26). (Note that, for a constant stratification N, the expression for the Green function in (4.1.42) converges to the Green function in (3.1.26)). The wave fields are qualitatively and quantitatively very similar away from the topography, but the left-propagating wave beam generated over the right slope of the topography is only present in figure 4-1(a), because only this solution accounts for both right- and left-propagating internal tides. Figure 4-1(e) shows the corresponding vertical velocity profiles away from the topography, at $x = 4\sigma$, where the differences between the two curves are limited to small fluctuations. The second comparison with the solution of Pétrélis et al. [75] concerns a taller and more supercritical topography with $h/H = 0.75$ and $\varepsilon = 4.38$. Figures 4-1(c) and (d) present snapshots of w/U evaluated using $\gamma(X)$ and $\gamma(Z)$, respectively, and figure 4-1(f) shows the corresponding vertical velocity profiles at $x = 4\sigma$. The differences are again negligible.

Figure 4-2 presents a comparison to the solution of Balmforth et al. [6] for a subcritical double ridge in a semi-infinite domain. The approach of Balmforth et al. [6] uses a Fourier series representation for the internal tide:

$$\phi(X, Z)e^{-i\omega_0 t} = \sum_{n=-\infty}^{\infty} \phi_n e^{inX - i|n|Z - i\omega_0 t}, \qquad (4.1.77)$$

and solves the following equation, which is obtained by imposing the inviscid bottom boundary condition:

$$\hat{h}(X) = \sum_{n=-\infty}^{\infty} \phi_n e^{inX - i|n|\varepsilon \hat{h}}. \qquad (4.1.78)$$

Equation (4.1.78) is simplified if the dimensionless topography $\hat{h}(X)$ is also represented as a Fourier series. This solution accounts for both right- and left-propagating internal tides and the interactions with neighboring subcritical topography. The topography in the comparison of figure 4-2 is composed of two identical subcritical Gaussian ridges with criticality $\varepsilon = 0.17$ and peaks separated by a distance $L = 6\sigma$. Figures 4-2(a) and (b) present snapshots of w/U at $\Phi = 0$, evaluated using the Green function solution and the Fourier series solution, respectively. Figure 4-2(c) shows the corresponding profiles at $x = 6\sigma$, and the curves are almost identical.

Lastly, the new solution method also compares well with the Green function solution of Llewellyn Smith and Young [55] for a knife-edge topography in a finite-depth channel and
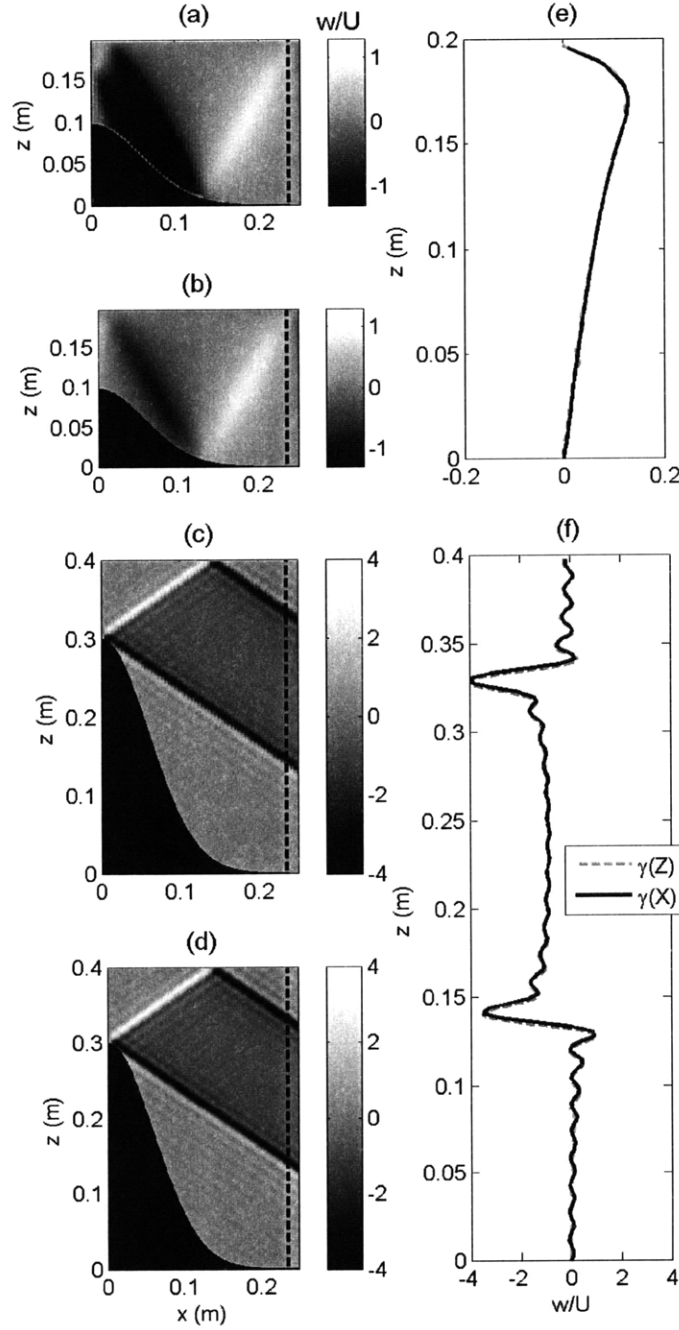
Figure 4-1: Comparisons of w/U for sub- and super-critical internal tides generated by a single Gaussian ridge using the internal tide solution presented in section 4.1 (using $\gamma(X)$) and the solution of Pétrélis *et al.* [75] (using $\gamma(Z)$). Snapshots at $\Phi = 0$ for a configuration with $h/H_0 = 0.5$ and $\varepsilon = 0.58$ evaluated using (a) $\gamma(X)$ and (b) $\gamma(Z)$. Snapshots at $\Phi = 0$ for a configuration with $h/H_0 = 0.75$ and $\varepsilon = 0.75$ evaluated using (c) $\gamma(X)$ and (d) $\gamma(Z)$. Vertical profiles at $x = 4\sigma$ for the (e) subcritical and (f) supercritical configurations.

106
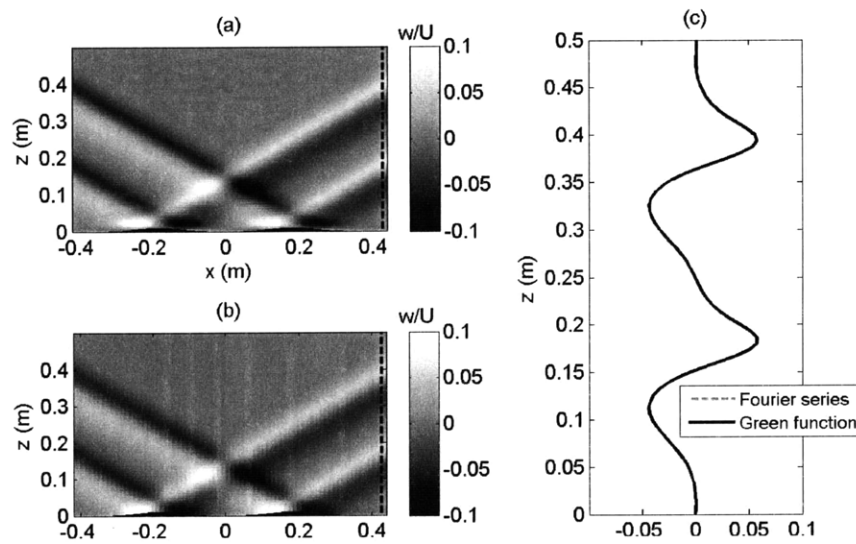
Figure 4-2: Comparisons of w/U for internal tides generated by two identical subcritical double Gaussian ridges using the internal tide solution presented in section 4.1 (using a Green function) and the solution of Balmforth *et al.* [6] (using a Fourier series). The ridges are $L = 6\sigma$ apart and have criticalities $\varepsilon = 0.17$. Snapshots at $\Phi = 0$ using (a) the Green function solution and (b) a Fourier series solution, and (c) comparison of the respective vertical profiles at $x = 7\sigma$.
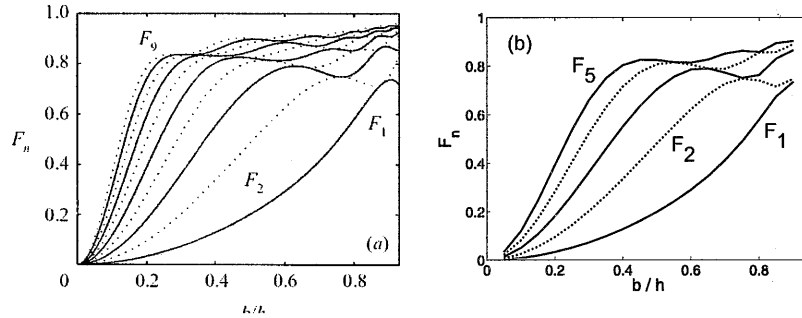
Figure 4-3: Comparisons of F_p for a knife-edge topography in an exponential stratification fit to WOD data obtained using (a) the solution of [55] (panel (a) is reproduced from figure 7 in the cited paper) and (b) the internal tide solution presented in section 4.1. The nomenclature is from [55]: b/h is the depth ratio. The lines represent increasing values of p.

in non-uniform stratification, which incorporates the WKB approximation. Figure 4-3(a), which is reproduced from figure 7 of [55], presents the low-mode structure of the far-field conversion rate F_p for modes $p = 1$ through 10 as a function of depth ratio h_0/H, for a knife-edge in a physical domain that is representative of the site of the Keana Ridge in Hawaii. The channel depth is set to $H = 4806\,\mathrm{m}$ and

$$N(z) = 0.5 + 0.001(e^{8.74z/4806} - 1)\,\mathrm{cph}, \qquad (4.1.79)$$

which is an exponential fit to a stratification from the Hawaii Ocean Time-series (HOT) database. Figure 4-3(b) shows the corresponding F_p for modes $p = 1$ through 5 evaluated using equations (4.1.55) and (4.1.56) for a narrow Gaussian ridge with $4\sigma = 3939\,\mathrm{m}$ and the same depth ratio, forcing and stratification used in the calculations of [55]. Both figures show the same trends in the modal distribution of the conversion rate, with mode 1 having an increasing contribution for increasing depth ratios, up to about 70% for $h_0/H = 0.9$. Both figures also show periodicity in the relative contribution of modes 2 to 4 for $h_0/H > 0.4$ such that, for specific values of h_0/H, the contribution of one of the higher low modes is exactly zero. Note that the good agreement in this comparisons attests to the correct implementation of the WKB approximation, rather than justify the use of the WKB assumption.

108

4.2   Results for idealized topography in uniform stratification

Having tested the approach of section 4.1, it is first applied to idealized Gaussian ridges in uniform stratifications to understand the implications of internal tide generation over asymmetric and aperiodic topography. Note that the added complexity of internal tide generation in non-uniform stratifications, when the WKB approximation is used, can be mapped onto equivalent problems in a uniform stratification. Therefore, the insights from the following idealized study are directly applicable to the problems in non-uniform stratification that are tackled in section 4.3 using the WKB approximation.

4.2.1   Isolated asymmetric ridges

We begin by considering an asymmetric Gaussian ridge:

$$h_G(x) = \frac{h_0}{1 - e^{-8}} \begin{cases} \exp\left(-\frac{x^2}{2\sigma_l^2}\right) - e^{-8} & -4\sigma_l \leq \ x \ \leq 0, \\ \exp\left(-\frac{x^2}{2\sigma_r^2}\right) - e^{-8} & 0 < \ x \ \leq 4\sigma_r, \\ 0 & x < -4\sigma_l \ \ , \ \ x > 4\sigma_r \end{cases} \qquad (4.2.1)$$

where h_0 is the maximum height, and $2\sigma_l$ and $2\sigma_r$ are the characteristic widths of the left and right sides of the ridge, respectively. The factor $1 - e^{-8}$ ensures that the topography smoothly goes to zero height at $4\sigma_l$ and at $4\sigma_r$, that is, at either side of the ridge. Since the slopes are different, the criticality on the left side of the ridge,

$$\varepsilon_l = \max\left(h_G' \in [x = -4\sigma_l : 0]\right)/\tan\theta, \qquad (4.2.2)$$

differs from that on the right,

$$\varepsilon_r = \max\left(\left|h_G' \in [x = 0 : 4\sigma_r]\right|\right)/\tan\theta. \qquad (4.2.3)$$

Figures 4-4(a) and (b), respectively, present snapshots of the normalized horizontal velocity u/U for wave fields generated by an asymmetric Gaussian ridge with depth ratio $h_0/H = 0.5$, $\varepsilon_r = 0.75$ and $\varepsilon_l = 0.5$ and 1.5. In figure 4-4(a), both sides of the ridge are subcritical, and thus the left- and right-going wave fields both possess a single beam propagating away from the side of the ridge facing away from the direction of propagation. The beam propagating to the left, which is generated on the steeper right slope, is sharper,
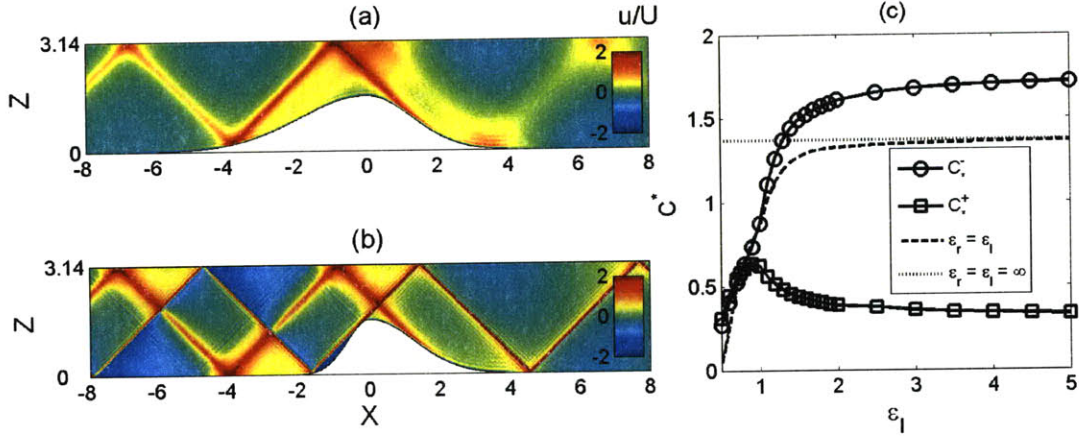
Figure 4-4: Snapshots of u/U for internal tides generated by asymmetric Gaussian ridges with $h_0/H = 0.5$, $\varepsilon_r = 0.75$ and (a) $\varepsilon_l = 0.5$ and (b) $\varepsilon_l = 1.5$. (c) Non-dimensional conversion rate $C_*^{\pm}$ as a function of ε_l for $\varepsilon_r = 0.75$, for a symmetric ridge ($\varepsilon_r = \varepsilon_l$), and for a knife-edge ($\varepsilon_r = \varepsilon_l \to \infty$).

containing finer vertical structure and a larger peak amplitude. In figure 4-4(b), the left side of the ridge is supercritical. Two wave beams are generated at the upper critical point of this slope, one radiating up and right and the other radiating down and left, causing the far field structure to be markedly different to the right and left of the ridge. In the right far-field there is a single sharp right-propagating beam, whereas in the left far-field there are two left-propagating wave beams, the sharper beam originating from the left side of the ridge and the broader beam coming from the right side. Formally there is a singularity in the wave field associated with the sharp beams originating from the critical slope. In practice, this has been circumvented by plotting the wave field using a sum of only the first 50 modes, which was sufficient for convergence.

Figure 4-4(c) presents the dimensionless conversion rate $C_*^{\pm}$ for the wave fields in figures 4-4(a) and (b) as a function of ε_l, which was varied by decreasing σ_l while keeping all other parameters constant. The conversion rate to the left, C_*^-, increases rapidly and monotonically with ε_l for $\varepsilon_l < 1.5$, with a notable rise in the rate of increase at criticality. The rate of ascent then diminishes for $\varepsilon_l > 1.5$, and by $\varepsilon_l \geq 5$ the conversion rate is essentially constant. The value of C_*^+ also initially increases with criticality for $\varepsilon_l < 1$. For $\varepsilon_l > 1$, however, there is initially a sharp decrease in C_*^+, beyond which the conversion

rate eventually settles to a constant value. The decrease in rightward energy flux coincides with the appearance of the second leftward propagating wave beam from the left-hand slope for $\varepsilon_l \geq 1$, and the same trend at criticality was consistently observed for both sub- and supercritical values of ε_r. Also included in figure 4-4(c) is the conversion rate associated with either left- or rightward energy flux for a symmetric ridge ($\varepsilon_r = \varepsilon_l$), which approaches the limiting value of a knife edge for $\varepsilon \geq 5$. This limiting value is actually less than that of C_*^-, revealing that the directional conversion rate of an asymmetric ridge can exceed that of a sharper symmetric ridge. However, the total conversion rate of the asymmetric ridge, this being the sum of left- and right-going energy fluxes, is lower than that of the knife edge, which is twice the value presented in figure 4-4(c).

Figure 4-5 presents F_p as a function of ε_l as ε_l is increased by decreasing σ_l. Although $F_p^{\pm}$ are dominated by mode 1, which always carries more than 60% of the energy flux, the modal content propagating to the left and right are quite different. Furthermore, as ε_l transitions from sub- to supercritical, there are sharp changes in the modal structure in both directions, coinciding with the appearance of the new left-going wave beam. For the left-going wave field, the relative contribution of mode 1 increases and mode 2 becomes much less significant than mode 3. Conversely, for the right-going wave field the contribution from mode 1 drops sharply around criticality, and the higher modes become much more significant.

4.2.2 Double ridges

For a double-ridge system we consider the sum of two Gaussian ridges $h_D(x) = h_{1G}(x) + h_{2G}(x)$, where

$$
\begin{aligned}
h_{1G}(x) &= \frac{h_1}{1-e^{-8}} \left[\exp\left(-\frac{(x+L/2)^2}{2\sigma_1^2} \right) - e^{-8} \right], \quad -L/2 - 4\sigma_1 < x < -L/2 + 4\sigma_1, \\
h_{2G}(x) &= \frac{h_2}{1-e^{-8}} \left[\exp\left(-\frac{(x-L/2)^2}{2\sigma_2^2} \right) - e^{-8} \right], \quad L/2 - 4\sigma_2 < x < L/2 + 4\sigma_2,
\end{aligned}
\tag{4.2.4}
$$

and h_D=0 elsewhere. Here, L is the separation between the two ridge peaks and $4\sigma_1$ and $4\sigma_2$ are the characteristic width of the left and right ridges, respectively.

For a pair of subcritical Gaussian ridges, the internal tide radiated by one of the ridges interferes with that radiated by the other, and is also scattered by the neighboring ridge, but it cannot be reflected back. Figures 4-6(a) and (b) present u/U for wave fields generated

111
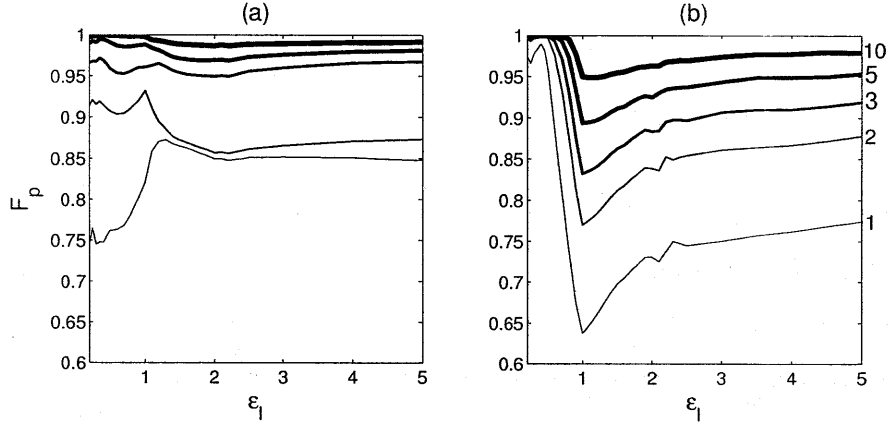
Figure 4-5: Fraction F_p of the far-field conversion in the first p modes to the (a) left and (b) right of the asymmetric ridge in figure 4-4(a). Results are shown for $p = 1, 2, 3, 5$ and 10, with the value of p increasing with line thickness, and also indicated on the right side of (b).

by two identical, subcritical Gaussian ridges with $h_1/H = h_2/H = 0.5$, $\varepsilon_1 = \varepsilon_2 = 0.75$ and $L/\sigma = 8.2$ and $L/\sigma = 11.2$, respectively, where $\sigma_1 = \sigma_2 = \sigma$. The radiated wave field is substantially different for the two scenarios. A single strong wave beam radiates to each side for $L/\sigma = 8.2$ (figure 4-6(a)). In contrast, for $L/\sigma = 11.2$ two weak beams radiate away in each direction, and there is intense activity between the ridges (figure 4-6(b)).

Figure 4-6(c) presents the conversion rate at either side C_*, evaluated using the first 50 modes, as a function of L/σ. For comparison, the conversion rate for a single ridge is also included in this figure. The first maximum in the periodic sequence is for $L/\sigma = 8.2$, which corresponds to constructive interference of the wave fields generated by the two ridges. For this scenario, presented in figure 4-6(a), one can follow the rightward propagating wave beam originating on the outside of the left ridge to the inside of the right ridge, where it reflects in-phase with the locally-generated rightward propagating wave beam. In contrast, for $L/\sigma = 11.2$ the wave beams generated on the outside of each ridge destructively interfere outside the confines of the ridges, as shown in figure 4-6(b), corresponding to a minimum in the periodic sequence of C_*. This periodic sequence of constructive and destructive interference has been previously reported in systems with periodic topography in infinitely-deep oceans ([67] and [7]), and we find similar trends if other parameters, such as h/H, are systematically varied.

112
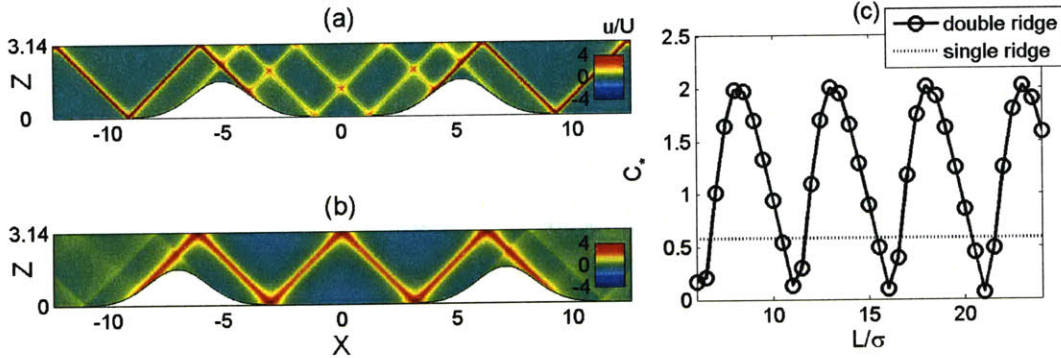
Figure 4-6: Snapshots of u/U for internal tides generated by two identical Gaussian ridges with $h_1/H = h_2/H = 0.5$, $\varepsilon_1 = \varepsilon_2 = 0.75$, and (a) $L/\sigma = 8.2$ and (b) $L/\sigma = 11.2$. (c) Non-dimensional conversion rate C_* as a function of L/σ. The dotted line shows C_* for a single ridge.

If the ridges in a double-ridge system differ in shape, it is reasonable to expect the radiated internal tide to be asymmetric. As an example, the normalized horizontal velocity fields for a pair of Gaussian ridges with $h_1/H = h_2/H = 0.5$, $L/\sigma_2 = 8.2$, $\varepsilon_2 = 0.75$ and $\varepsilon_1 = 0.5$ and 1.5 are presented in figures 4-7(a) and (b), respectively, the criticality ε_1 being changed by virtue of changing σ_1. When both ridges are subcritical the left- and right-going fields are qualitatively similar, as shown in figure 4-7(a). However, when the left ridge is supercritical, as in figure 4-7(b), a distinct asymmetry is apparent. The far-field internal tide is dominated in both directions by the sharp wave beams generated at the supercritical ridge. The asymmetry arises because the rightward supercritical wave beams reflect at different locations on the subcritical ridge, and therefore come closer to one another. Another contributing factor to the asymmetry, albeit a weaker one, is the initially leftward propagating wave beam from the subcritical ridge being reflected back to the right by the supercritical slope it encounters on its path.

As is the case for a symmetric double ridge (figure 4-6), the nature of the radiated tide for an asymmetric double-ridge system depends sensitively on the ridge geometry. Figure 4-7(b) shows a noticeably stronger tide than figure 4-7(c), yet the only difference between the two is a change in L/σ_2 from 8.2 to 10. This relatively small change, however,

113

has important geometric consequences. In contrast to the wave field in figure 4-7(b), for example, the leftward propagating wave beam originating outer slope of the right ridge in figure 4-7(c) no longer encounters the left ridge, significantly altering the wave structure in the left far-field.

To further demonstrate the impact of geometric asymmetry on the radiated internal tide, figure 4-7(d) presents $C_*^{\pm}$, evaluated using 50 modes, as a function of ε_1, where ε_1 is changed by either decreasing σ_1 (as in figures 4-7(a) and (b)) or increasing h_1. Although asymmetry in the conversion rate is most obvious when the left ridge is supercritical, there is even some asymmetry when both ridges are subcritical. Note that the results for increasing values of h_1 are truncated at $\varepsilon_1 = 1.4$ since C_* diverges as h_1/H approaches 1. One may be inclined to assume that C_*^+ will always exceed C_*^- for the configuration presented in figure 4-7, as the supercritical ridge can reflect energy from the subcritical ridge back to the right. This is not always so, however, as exemplified by the stronger energy flux towards the left for the configuration in figure 4-7(c), which is indicated in figure 4-7(d).

Figure 4-8 presents F_p for the wave field radiated by the double ridge system in figure 4-7(a) as ε_1 is increased by decreasing σ_1. The radiated modal structure to left and right is qualitatively and quantitatively very similar for $\varepsilon_1 \leq 1$, which is expected since the far-field structure in each direction comprises two subcritical wave beams of like amplitude. For $\varepsilon \simeq 1$ the relative contribution of mode 1 dips to less than half for the left-going wave field, but peaks for the right-going wave field. For $\varepsilon_1 > 1$, however, this trend is reversed, and a notable feature is that mode 2 contributes far more significantly to the rightward than to the leftward energy flux.

4.3 Results for realistic topography in varying stratification

We proceed to investigate more realistic single and double ridges in non-uniform stratifications, using the Hawaiian and Luzon ridges as examples. These studies are idealized as they assume 2-D flow for cross-sections of the ridges, and they employ the WKB approximation to account for a non-uniform background stratification, which is least accurate for the lowest mode. Nevertheless, this is a significant advance on previous analytical studies that are not amenable to realistic topography and stratification. The predictions of the analytical model for these two geographical locations are compared here with the results of relevant
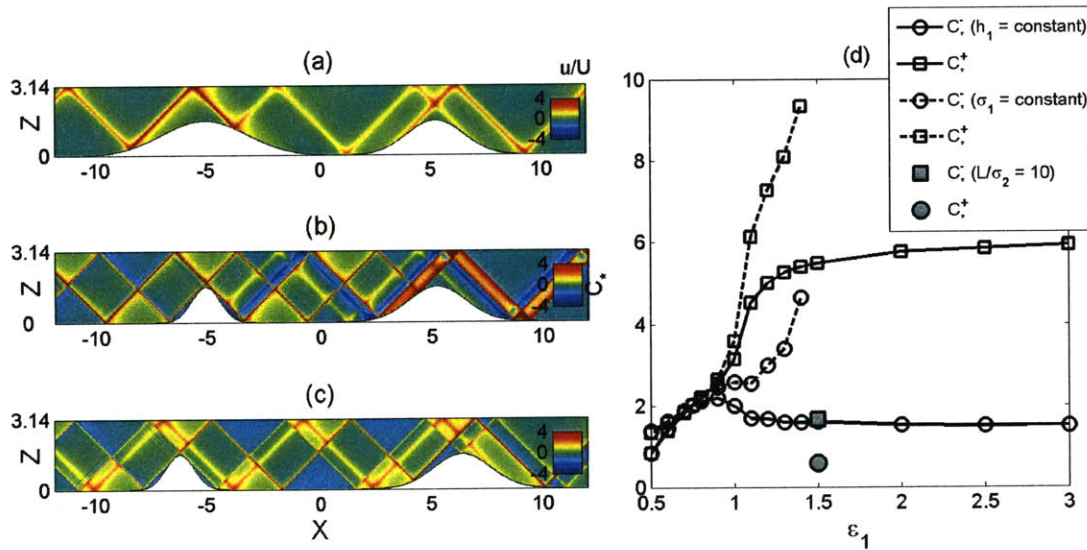
Figure 4-7: Snapshots of u/U for internal tides generated by a double ridge with $h_1/H = h_2/H = 0.5$, $\varepsilon_2 = 0.75$, $L/\sigma_2 = 8.2$ and (a) $\varepsilon_1 = 0.5$, and (b) $\varepsilon_1 = 1.5$. (c) The same as (b) except $L/\sigma_2 = 10$. (d) $C_*^{\pm}$ as a function of ε_1, where ε_1 is varied by changing σ_1 (solid lines) and h_1 (dashed lines).
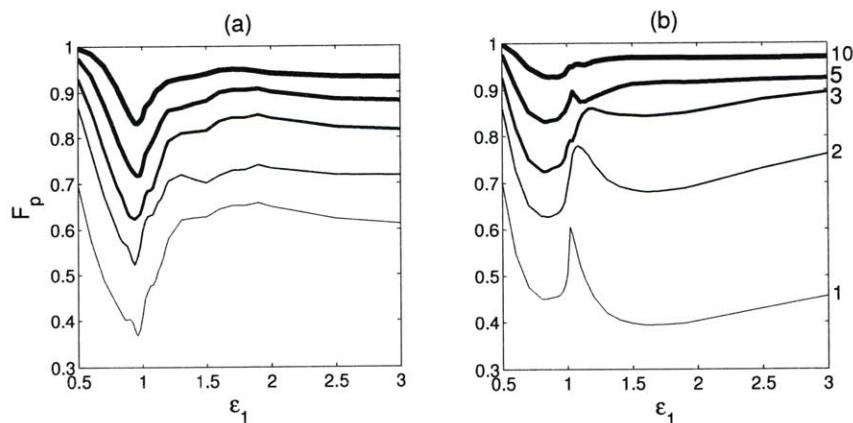
Figure 4-8: Fraction F_p of the far-field conversion in the first $p = 1, 2, 3, 5$ and 10 modes to the (a) left and (b) right of the double ridge.

numerical simulations and field data.

4.3.1 Hawaiian ridge

Figures 4-9(a) and (b) show the bathymetry of the ridge between French Frigate Shoals (FFS) and Brooks Banks, and of Keana Ridge (KR) in the Kauai Channel, respectively. The bathymetry data for FFS was obtained from the latest satellite-derived marine topography release SRTM30_PLUS [9], and the bathymetry data for KR was obtained from multibeam data compiled by the Hawaiian Mapping Research Group [33]. Internal tide generation was modeled at 6 evenly-spaced, 120 km-long cross-sections at FFS, and 10 evenly-spaced, 140 km-long cross-sections at KR. For each cross-section, $h(x)$ was obtained by fitting the bathymetry every 1.4 km with a spline and interpolating to obtain a smooth shape sampled every 70 m. The same sample stratification $N(z)$ was used for both locations, since there is not much spatial variability in the averaged stratifications for FFS and KR [46]. The stratification, presented in figure 4-9(c), was obtained from an average of thirty 1100 m-deep CTD casts in the Hawaiian Ocean Time-series (HOT) database [34] taken at 24-hour intervals during September 2000 at the Kauai Channel. The profile for the upper 100 m is an interpolated spline of the HOT stratification, while for the bottom 4900 m it is an exponential fitted to match the values of the measured stratification at depths of 100 m, 300 m and 1050 m:

$$N(z < -100\,\text{m}) = 3.043 \times 10^{-4} + 0.0161 e^{z/389} \quad \text{rad/s}, \tag{4.3.1}$$

where $z = 0$ is the ocean surface.

The 2-D, far-field conversion rate $C^{\pm}$, where the subscript '-' indicates southwest and '+' indicates northeast, was calculated for each cross-section in figure 4-9(a) using 100 modes, with $\bar{\rho} = 1010$ kg m^{-3} and H, μ and $\bar{N}$ evaluated at each cross-section using $\omega = 1.4 \times 10^{-4}$ rad/s and $f = 5 \times 10^{-5}$ rad/s. For the purpose of this study, a reasonable value of the far-field barotropic velocity was taken to be $U = 2$ cm/s, which lies between the smaller value of $U = 1$ cm/s used in numerical and analytical studies [61], [55]; and $U = 3 - 4$ cm/s reported in field studies [84], [51]. Since the magnitude of C scales with U^2 (equation (4.1.55)), this introduces significant uncertainty into the predicted conversion rates, which can therefore only be roughly estimated.
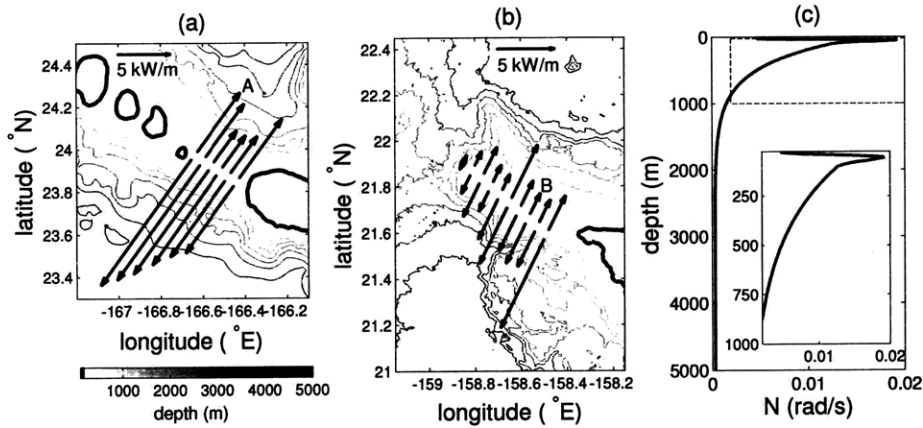
Figure 4-9: Bathymetry of (a) the ridge at French Frigate Shoals (FFS) and (b) the Keana Ridge (KR) in the Kauai Channel. The vectors in (a) and (b) are proportional to the two-dimensional conversion rate evaluated at 6 cross-sections of FFS and 10 cross-sections of KR. The stratification presented in (c) is from averaged HOT CTD casts, with a zoom-in of the stratification in the upper 1000 m (inset).

The values of $C^{\pm}$, represented by the vectors on figures 4-9(a) and (b), vary from 3.7 kW/m to 14.6 kW/m at FFS and from 0.2 kW/m to 8.5 kW/m at KR. At KR, the maximum conversion rate occurs at the southeastern end of the ridge, where the depth ratio approaches 0.9. Further southeast $h_0/H > 0.9$, so we expect flow to be three-dimensional, preferring to go around rather than over the ridge, and two-dimensional linear theory is unlikely to provide a reasonable estimate of the tidal conversion. The magnitudes of the predicted conversion rates at both FFS and KR are in good agreement with the results of 3-D numerical simulations by Merrifield and Holloway [61] which predict depth-integrated energy fluxes of approximately 15 kW/m southward and 10 kW/m northward of FFS, and approximately 10 kW/m southward and 8 kW/m northward of KR. This is also consistent with field data, which yields estimates of approximately 21 kW/m southward and 7.5 kW/m northward of FFS, and approximately 17 kW/m southward of KR (Lee *et al.* [51], Nash *et al.* [64]). In making these comparisons we note that, as opposed to $C^{\pm}$ evaluated using the analytical model, which does not account for dissipation, the far-field depth-integrated horizontal energy flux of numerical and field studies does not reflect the entire barotropic to

117

baroclinic conversion. While the quantitative values of the theoretical conversion rates have inherent uncertainty, due to the quadratic dependence of C on U, an important qualitative feature that is well captured by the analytic model is the asymmetry of the energy flux from both FFS and KR. The results in figures 4-9(a) and (b) predict that for both locations the internal tide radiated to the southwest is $O(50\%)$ stronger than that to the northeast, which is a standout feature of the data from field studies and numerics (see figure 1 in [51] and figure 6 in [61]).

Figure 4-10 presents snapshots of u/U at locations A and B in figures 4-9(a) and (b), respectively. Internal wave beams propagate away from the steep slopes of the topography and are refracted by the stratification, such that, as they approach the thermocline, they become more horizontal. In cross-section A (figure 4-10(a)) the ridge has a shallow peak at a depth of 800 m, with one inflexion point on the southwest side that otherwise has a uniform steep slope, and some roughness on the northeast side associated with several points of high criticality. There are four principal wave beams generated, two on each side of the peak, and a couple of notable, but weaker, northwest propagating beams generated by the rough features on the northwest slope. Cross-section B (figure 4-10(b)) coincides with the location of field observations by Nash *et al.* [64] and Rainville and Pinkel [78]. Here the topography has steep supercritical slopes (particularly on the southwest face) and a relatively flat peak at a depth of 1000 m. A pair of wave beams, one upward and the other downward propagating, originate from each side of the peak. Nash *et al.* [64] also discerned two internal wave beams propagating southwest from the plateau, while Rainville and Pinkel (2006) reported upward barotropic to baroclinic conversion over the plateau, associated with the two upward-propagating internal wave beams generated at either flank.

For cross section A, more detailed analysis reveals that 57% of C^- is due to mode 1, which is about twice the 29% contribution of mode 2. Lee *et al.* [51] also report a highly-dominant mode 1 propagating southwest from this location. At cross-section B the theory predicts that mode 1 accounts for 48%, and mode 2 for 30%, of C^-, which is in accord with the field data of [64], who attribute $\sim 65\%$ of the southwest energy flux to mode 1 and $\sim 31\%$ to mode 2. The insert in figure 4-10(b) presents the depth-integrated, time-averaged, across-ridge energy flux as a function of cross-ridge position for transect B. This plot further clarifies the earlier statement that in the far-field C^- is on the order of 50% stronger than
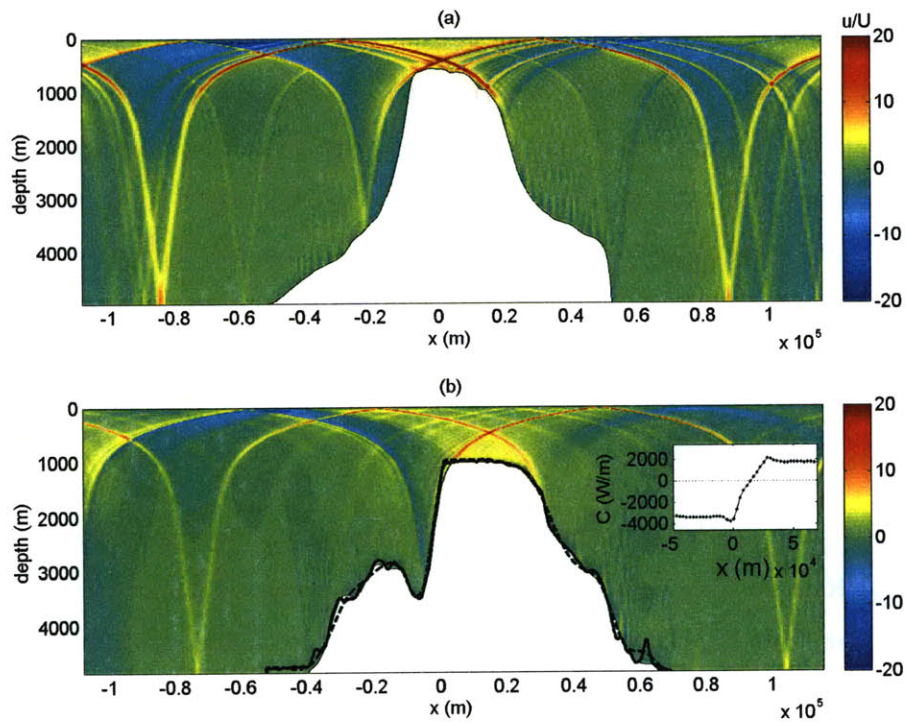
Figure 4-10: Normalized across-ridge velocity fields (u/U) generated at cross-sections (a) A and (b) B in figure 4-9. The thick lines in panel (b) indicate the raw bathymetry data (solid) and a smoothed version of the profile (dashed), and the inset presents the local depth-integrated, time-averaged, across-ridge energy flux. The horizontal coordinate is oriented in the southwest to northeast direction.

C^+. Nash *et al.* [64] found the energy flux to be zero atop much of the plateau, suggesting a standing wave pattern due to the super-position of nearly-symmetric wave beams generated at either flank of the ridge. We also find a reduced energy flux over the ridge, but only near the center of the plateau.

The aforementioned analysis was performed using a mildly-smoothed version of the original bathymetric data, indicated by the solid thin and thick black lines framing the topography in figure 4-10(b), respectively. The conversion rates calculated using the smoothed data varied by only 1% from those calculated using the raw data. The dashed black line in figure 4-10(b), however, shows a yet smoother fit to the topography: a spline being fitted every 4 km and interpolated to every 40 m. This slightly smoother representation yields a 15% greater value of C^-, although only about a 1% lower value of C^+, due to the fact that the supercritical feature on the northwest slope has been modified. This result supports the assertion of Nycander [67] that one of the greatest uncertainties in computation of internal tide generation is topographic resolution.

4.3.2 Luzon Strait ridge

Figure 4-11(a) shows the bathymetry of the Luzon Strait (LS) obtained from the ETOPO2 model of the National Geographic Data Center [65]. The two dominant features are the substantial east (Lan-Yu) ridge that extends from north to south across the entire strait, and the west (Heng-Chun) ridge that becomes much less significant at the southern end of the strait. In comparison to the sections of the Hawaiian ridge studied in the previous section, LS bathymetry is generally shallower and more intricate, making the associated barotropic flow more three-dimensional and the region less amenable to two-dimensional analytic study. Nevertheless, we follow the lead of Chao *et al.* [11] and investigate the two-dimensional cross-sections marked A, B and C in figure 4-11(a), located at 19.97° N, 21.15° N and 21.39° N, respectively, to assess the impact of the west ridge on the internal tide radiated to the west. Towards the south, where the west ridge is relatively deep, internal tide generation by the east ridge is expected to dominate. At northern locations, where the depth ratios of the west and east ridges are similar, the west ridge is expected to play a more significant role. Figure 4-11(b) shows the stratification $N(z)$ used in the model. This was obtained from an average profile of 2575m-deep CTD casts from April and July of 2007 [22] using an interpolated spline of the available stratification and, in deeper water,

120

the following exponential fit of the form used by [55] in (4.1.79):

$$N(z < -2575\,\text{m}) = \left[3.5113 + 0.0175\left(e^{\frac{8.74z}{H}} - 1\right)\right] \times 10^{-4}\text{rad/s}, \qquad (4.3.2)$$

where $z = 0$ is the ocean surface.

The two-dimensional far field conversion $C^{\pm}$, where '-' corresponds to west and '+' to east, was calculated for cross sections A, B and C using the semidiurnal tide and $U = 5\,\text{cm/s}$ [66], [11], [42]. The topography used in the calculations was found by fitting the bathymetry every 10 km with a spline and re-sampling the fit using interpolation every 100 m. Qualitatively, our results show that the internal tide radiated at cross sections A and B is significantly stronger than that radiated at cross section C. The conversion rates, which are highly influenced by the quadratic dependence of C on U, are $O(10)\,\text{kW/m}$ to $O(100)\,\text{kW/m}$, and are consistent with the numerical results of Niwa and Hibiya [66] and Jan, Lien and Ting [42]. The analytical model predicts unrealistically high energy fluxes for latitudes such as 20.5° N (the Batanes Islands) where the depth ratio of the east ridge approaches unity. These unphysical results could nevertheless be important indicators of generation hot-spots.

A snapshot of u/U for the internal tide at cross-section B is presented in figure 4-12(a). A standout feature is the strong, west-propagating wave beam produced by constructive interference of two other wave beams, one generated at each of the twin peaks of the east ridge. Figure 4-12(b) reveals that reducing the height of the west ridge by 20% causes another wave beam from the most eastern peak, which is otherwise reflected back by the supercritical slope of the west ridge, to continue to propagate west, significantly altering the character of the westward internal tide.

Figure 4-13 summarizes the effect on the westward internal tide of decreasing the height of west ridge by 20% for all three cross sections. The bar height represents the dimensionless conversion rate C_*^-, and each bar is divided into contributions from the different vertical modes. The energy flux at cross-sections A and C is dominated by mode 1, but at cross section B it is mode 2 that dominates. Reducing the height of the west ridge reduces C^- for both A and C, and dramatically so for C, but substantially increases C^- for cross-section B. Consistent with the results of [11], we therefore conclude that at the southern end of LS the west ridge plays a relatively minor role in internal tide generation due to its small size,
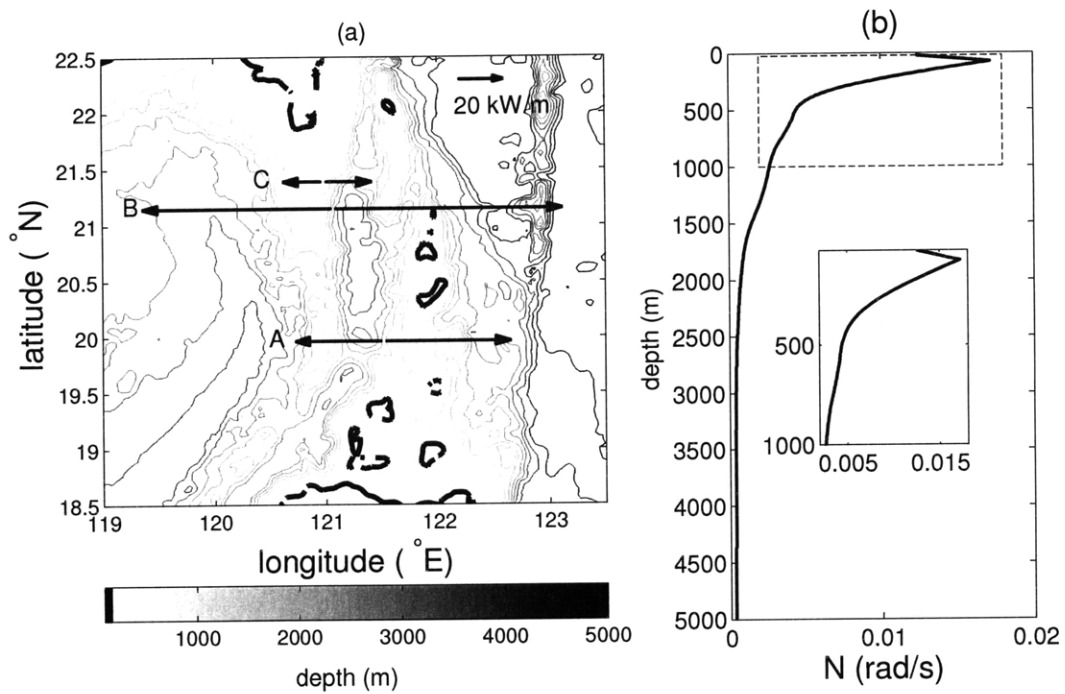
Figure 4-11: (a) Bathymetry and (b) stratification of the Luzon Strait. The vectors in (a) are proportional to the two-dimensional energy flux evaluated at 3 representative cross-sections. The stratification presented in (b) is from averaged CTD casts, with a zoom-in of the stratification in the upper 1000 m (inset).
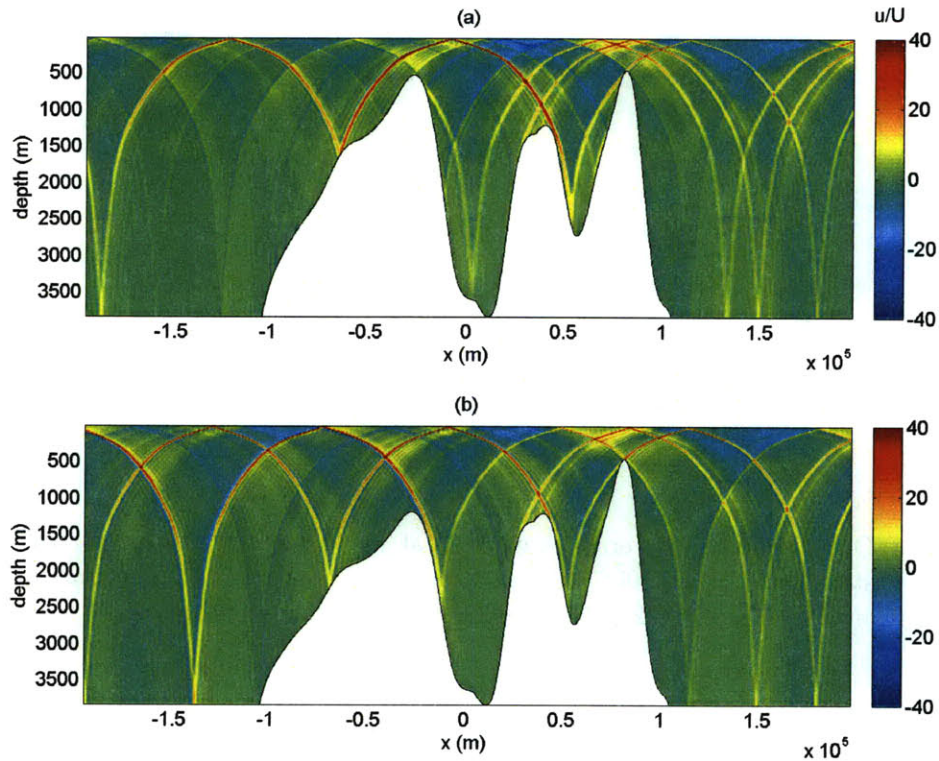
Figure 4-12: Normalized across-ridge velocity fields (u/U) generated at cross-section B with (a) full-height and (b) 80%-height versions of the west ridge. The horizontal coordinate is oriented in the west to east direction.

whereas further north its role is much more substantial. Their conclusion that at north latitudes the west ridge augments the westward internal tide seems to be too sweeping a generalization, however, as we find the opposite to be true for cross section B. Rather, the nature of the radiated internal tide depends very sensitively on the bathymetry and the stratification, and needs to be assessed on more of a case-by-case basis.

4.4   Discussion and contributions

The Green function solution to internal tide generation by topography has been generalized for arbitrary 2-D topography, and the WKB approximation has been used to account for the effects of weakly non-uniform stratification. This new analytical model has been used to investigate internal tide generation by canonical asymmetric 2-D topographies as well as
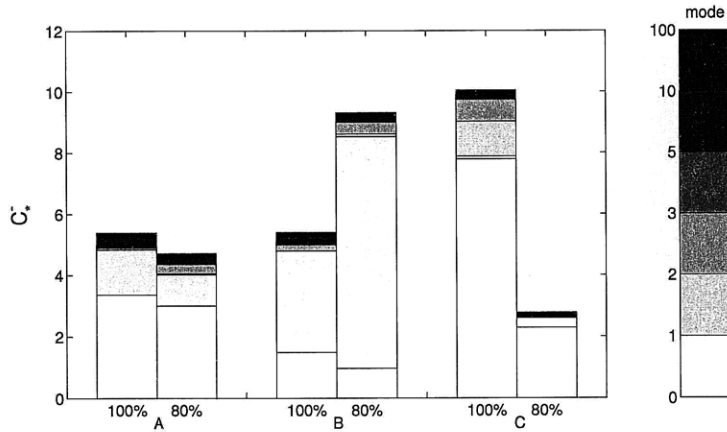
Figure 4-13: Dimensionless conversion rates C_*^- at locations A, B and C for the case in which the western ridge is at 100% and at 80% of its true height. The fraction of the conversion rate in modes $p = 1, 2, 3, 5, 10$ and $p > 10$ is indicated within each bar.

to directly investigate the 2-D internal tide generation in tall ocean ridges.

The investigation of section 4.2 confirmed that the structure of internal tides generated over asymmetric and aperiodic topography is affected by asymmetric slopes on a ridge, by internal tide interference, and by scattering at neighboring topography. These processes, and therefore the radiated internal tide, may be very sensitive to the geometric configuration of the site. This is nicely illustrated by the case study in the northern Luzon Strait. The presence of the western ridge has a dramatic effect on the internal tide radiated to the west, but whether the effect is to enhance or reduce the tide is sensitive to the location and height of the western ridge.

The analytical predictions of the internal tide radiated from Hawaii and the Luzon Strait are in good qualitative agreement with 3-D numerical models and field observations of the energy flux away from the ridge. For the case study of Hawaii, the conversion rates are within an order of magnitude of the observations, and the analytical model captured the general trends in terms of the asymmetry and the magnitude of the conversion rates at different locations along the ridge. The model also captured some detail of the relative contributions of modes 1 and 2: near the French Frigate Shoals the energy in mode 1 is significantly larger, whereas at the Keana Ridge the contributions of mode 1 and 2 are comparable.

124

The model was applied with more caution to cross-sections of the ridge at the Luzon Strait, which often surfaces as small islands and in general has more 3-D features. In fact, the conversion rates evaluated at cross-sections with large depth ratios between the Batanes Islands were excessive in comparison to predictions from previous 3-D numerical studies. This confirms the relevance of 3-D effects, such as, for example, flow going around peaks in regions where the depth ratio changes along the ridge. Nevertheless, the conversion rates predicted using the analytical model for cross-sections at several locations along the ridge are of the same order of magnitude as the depth-integrated horizontal energy flux reported in the numerical studies. The analytical model is also used successfully to assess the effect of the western ridge on the radiated internal tide, which is much more significant in the north because the western ridge is tallest here, and can be more subtle than a simple enhancement of the tide.

Overall, the model is a straightforward and computationally inexpensive tool that may be used for an initial qualitative assessment of the internal tides generated at relevant geophysical sites. The limitations of the theory should be reviewed such that future users have a sense of its applicability and the accuracy of its estimates. The theory is applicable for small excursion parameters over tall topography that is nominally 2-D. It will provide reasonable estimates for finite excursions parameters provided that mode 1 dominates the internal tide, as mode 1 is the least affected by nonlinearities, which act on short vertical length scales. Note that mode 1 tends to have a more significant contribution for tall ridges with depth ratios of $O(1)$, as discussed in chapter 3, and that the vertical scales associated with mode 1 are determined by the details of the background density stratification. The accuracy of estimates made using this linear theory is limited to the accuracy of the WKB approximation for the corresponding density stratification profile, and accuracy will also be compromised as 3-D effects or nonlinear effects start to play a role. Lastly, one further limitation of this model is that it is applied for a single frequency or constituent of the tide.

A situation that arose naturally, while investigating internal tide generation by tall double ridges in sections 4.2 and 4.3.2, was that internal wave beams may encounter the supercritical slopes of neighboring topography and reflect back upstream. This situation suggests the possibility of internal wave rays bouncing back and forth and ultimately being trapped in the valley of a double ridge. If the geometry is right, it is possible that internal wave rays converge into closed trajectories between the two ridges. Attractive orbits of

internal wave rays are also called internal wave attractors and have only been studied previously in closed basins (by Maas *et al.* [56], Hazelwinkel *et al.* [35] and Grisouard *et al.* [31]). These considerations motivate the investigations of chapter 5.

Chapter 5

Internal tide attractors

Internal wave attractors are said to exist when an internal wave ray converges towards a closed trajectory [57], which is geometrically possible in the valley between two neighboring supercritical ridges [87]. This chapter investigates internal tide generation scenarios in double ridges where internal wave attractors exist. An approach using a one-dimensional (1-D) checkerboard map [8] is developed and used to identify the existence and stability of attractive closed trajectories for internal wave rays as a function of the double-ridge configuration. Furthermore, dissipation is incorporated into the Green function method of chapter 4 so that the focusing of energy in an internal tide attractor may be balanced by dissipation and a time-periodic internal tide solution can exist. An internal wave attractor is reproduced in a laboratory experiment and the results are compared with the predictions of the modified theory.

In section 5.1, a 1-D checkerboard map of subsequent upward reflections of internal wave rays in double-ridge geometries is constructed and used to assess the existence and stability of simple closed orbits. In section 5.2, the Green function method is applied to the dissipative internal tide problem, and a perturbative approach is used to handle physical viscosity. The theory is shown to converge for a configuration with an attractive orbit. This is followed, in section 5.3, by a comparison between theory and a laboratory experiment for double-ridge configurations with and without an attractor. The contributions of this work are discussed in section 5.4.

5.1 Finding internal wave attractors

The first task at hand is to determine whether a closed trajectory exists inside a double ridge system for rays that propagate satisfying the internal wave dispersion relation. Here we consider the problem of rays that propagate in straight lines since, as discussed in chapter 4, a system with a weakly non-uniform stratification can be mapped onto this scenario via the WKB approximation. The study in this chapter is furthermore limited to orbits that are not self-intersecting, consisting of just four reflections: three off the topography and one off the free surface. More complicated orbits with multiple surface reflections are also possible in between double ridges, but these are harder to study in the laboratory and less likely to persist as a coherent structure in nature. Once the existence of a closed trajectory has been determined, the 1-D map is used to determine whether this trajectory is stable or unstable (i.e. locally attracting or repelling to nearby rays).

5.1.1 Checkerboard maps

An asymmetric double Gaussian ridge, presented in figure 5.1.1, is used as an illustrative example to investigate internal tide attractors. The topography,

$$h(x) = h_1 \exp\left[-\frac{(x+L/2)^2}{2\sigma^2}\right] + h_2 \exp\left[-\frac{(x-L/2)^2}{2\sigma_1^2}\right], \tag{5.1.1}$$

has two peaks of different heights $h_1 = 0.113\,\text{m}$ and $h_2 = 0.225\,\text{m}$ and the same characteristic width $4\sigma = 0.104\,\text{m}$, separated by a distance $L = 0.302\,\text{m}$ apart and in a channel of depth $H = 0.296\,\text{m}$. These parameters represent the configuration used in the laboratory experiments described in section 5.3. For a closed trajectory to exist between the two ridges, a minimum requirement is that both inner slopes are supercritical. The points where the topography is exactly critical are represented by the points labeled n_1 to n_8 in figure 5.1.1. Internal wave rays in a simple closed trajectory that is not self-intersecting must reflect once on each of the supercritical slopes $[n_3 : n_4]$ and $[n_5 : n_6]$ in order to change direction back towards the valley. Furthermore, a subcritical reflection must occur in the valley such that downward internal wave rays can reflect back upward. That is, we require that $n_4 < n_5$. Shadow points, labeled m_1 to m_4 in figure 5.1.1, indicate the projection of an internal wave ray from a critical point to the topography. Of the subcritical reflections in the valley, only those within the shadow regions $[n_3 : m_2]$ and $[m_3 : n_6]$ will continue toward a reflection
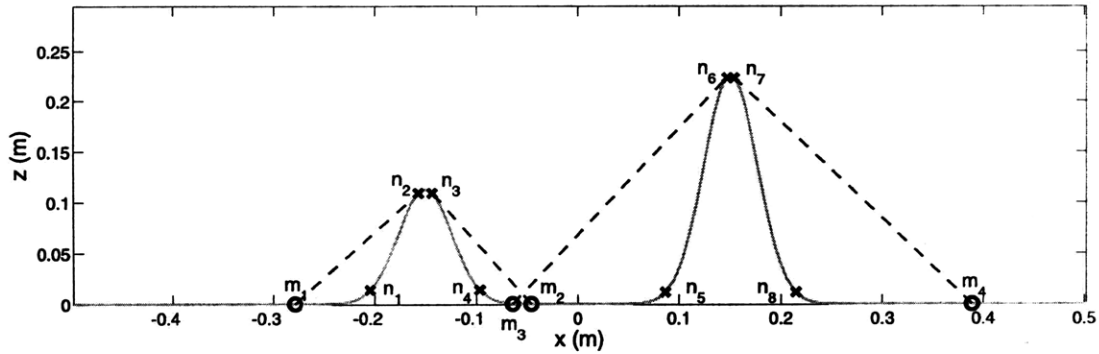
Figure 5-1: Schematic of a double Gaussian ridge indicating the location of the critical points $n_1 - n_8$ and the shadow points $m_1 - m_4$.

on the adjacent supercritical slopes $[n_3 : n_4]$ and $[n_5 : n_6]$ (for rays going clockwise and anticlockwise, respectively). Therefore, another condition for the existence of simple closed trajectories is that the shadow regions intersect in the valley, i.e. $m_3 < m_2$.

If an internal wave ray is in a closed orbit, it returns to the same $x-$location on the topography, x_a. Therefore, a useful tool to study the path of internal wave rays between the ridges is a 1-D map, $x_{n+1} = f(x_n)$, that maps subsequent $x-$locations of reflections from the topography. In constructing this map, care must be taken to account for the possibility of rays switching between downward and upward-propagating at subcritical slopes and at the surface, and between leftward and rightward-propagating at supercritical slopes. To simplify this task, we construct a graph that maps up-going rays to up-going rays, implicitly accounting for any reflections that produce a down-going ray, while explicitly accounting for reflections at supercritical slopes that switch between left- and right-going rays.

Figure 5-2 presents the 1-D map for the double Gaussian ridge in (5.1.1) with internal wave rays propagating at different angles with respect to the horizontal, $\theta = 54.9°$ and $\theta = 47.1°$. The function fzero in MATLAB was used to determine the subsequent $x-$locations of the intersection of internal wave rays with the topography. These $x-$locations are charted on the map using all four quadrants to account for rays that propagate to the right and to the left after a reflection on the topography, thereby incorporating switching at supercritical slopes. The domains $-2l < x^* < 0$ and $0 < x^* < 2l$ are used to represent left- and right-going rays, respectively, where the physical locations x of rightward reflections are

mapped into $x^* = x + l$, and the locations of leftward reflections are mapped onto $x^* = x - l$. In figure 5-2,

$$l = 2L + 2.5H/\tan\theta \qquad (5.1.2)$$

to show the effect of a complete transition between two upward reflections in the far field $|x| > 2L$, where the topography is flat and the horizontal distance traveled between consecutive upward reflections is $2H/\tan\theta$.

The trajectory of an internal wave ray is shown in figures 5-2(a) and (b) for $\theta = 54.9°$ and $\theta = 47.1°$, respectively, and the corresponding physical ray path is plotted in the inset in each figure. In figure 5-2(a), the example ray is initially right-propagating and originates at the physical location 1, which is represented by the point 1^+ on the map. The first upward reflection occurs at point 2, before the ray reaches the domain of the topography, corresponding to the point 2^+ on the map. Next, the ray encounters a subcritical region at point 3 in the valley of the two ridges, and continues to propagate to the right as it reflects upward; this is represented as point 3^+ on the map. These first few, rightward reflections are represented in the first quadrant. The internal wave ray then encounters a supercritical slope at point 4 and subsequently travels leftward. To account for this, the map sends the ray from the point 4^+, via the fourth quadrant, to the point 4^- in the third quadrant. The next time the ray encounters topography as an up-going ray, after intermediate downward reflections at the surface and a supercritical slope, is at point 5 where it becomes right-going. Therefore, in the map the iteration proceeds via the second quadrant to intercept the point 5^+ in the first quadrant. In the next iteration the ray proceeds to physical point 6, which is point 6^+ in the map, and then escapes the domain of the double ridge.

An internal wave attractor exists in the configuration for $\theta = 47.1°$. The trajectory drawn in figure 5-2(b) shows a ray trapped in an orbit, switching from the first to the third quadrant as it reflects on the right-most supercritical slope in the valley and turns left, and switching back to the first quadrant upon its next upward reflection in the valley, at $x_a = -0.046\,\text{m}$.

5.1.2 Existence and stability

As suggested above, not all double ridges will sustain a closed trajectory. For a simple orbit with a single surface reflection as in figure 5-2(b), an internal wave ray returns to x_a every

130
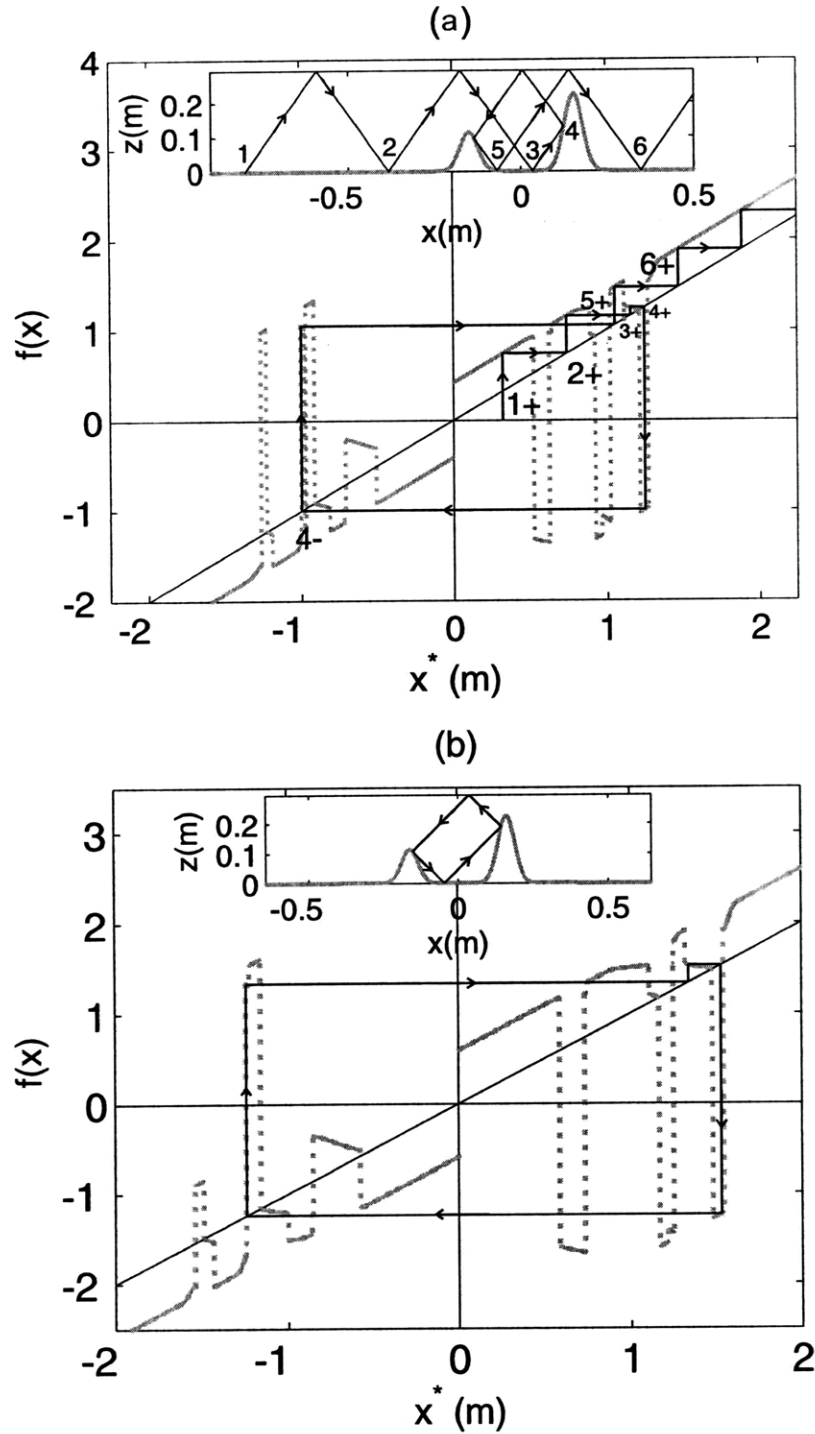
Figure 5-2: A 1-D map of upward reflections of internal wave rays from a double Gaussian ridge. An example ray path is indicated by the solid black line in each 1-D map and, within the inset, the ray path in the physical (x, z)−plane is presented. The coordinate $x^* = x \pm l$. (a) Configuration with $\theta = 54.9°$ in which internal wave rays escape, with $l = 1.12\,\text{m}$. Upward reflections on the topography occur at the points labeled 1 thorough 6. (b) Configuration with $\theta = 47.1°$ in which an internal wave attractor exists, with $l = 1.30\,\text{m}$.

131

second upward reflection. Therefore, the existence of closed trajectories as a function of geometric parameters in the configuration is determined by studying the second return map $x_{n+2} = f_2(x) = f(f(x))$.

Figure 5-3(b) shows the second return map for the orbit of figure 5-2. The configuration in which this orbit exists was found by surveying the geometry in equation (5.1.1) for different values of θ. The range of θ surveyed was chosen such that the basic geometric criteria, $n_4 < n_5$ and $m_3 < m_2$, was satisfied. For each value of θ, the domain between m_3 and m_2 was divided into suitably well resolved intervals. An internal wave ray was propagated up and to the right from the edge of each interval until its second upward reflection. If a ray returned to its departure location then the existence of a closed trajectory was established. In figure 5-3(b) the attractor exists where the map intersects the $f_2(x) = x$ line at x_a. The stability of this orbits is determined from the local slope of the second return map in the region around the attractor, $f_2'(x_a) = df_2/dx$. In particular, if $f_2'(x_a) < 1$, at each subsequent return a neighboring ray will reflect at an x–location that is closer to x_a, and thus the closed orbit is locally attractive, and therefore locally stable. Similarly, if $f_2'(x_a) > 1$, neighboring rays diverge from the closed orbit, which is therefore unstable. Note that, if a closed orbit attracts rays in clockwise paths it will equally repel rays in anticlockwise paths. The result of surveying the domain for internal wave attractors is summarized in figures 5-3(a) and (c). Figure 5-3(a) presents a bifurcation diagram that charts the existence and stability of anticlockwise orbits with decreasing θ, which arise in a saddle-node bifurcation at $\theta = 47.37°$, and the unstable orbit disappears for $\theta < 47.27°$.

The existence of internal wave attractors can similarly be studied as a function of the other configuration parameters, so there is a wealth of bifurcation sequences that can occur. However, having found a configuration which, for the correct value of θ sustains a single stable orbit with a single surface reflection, we now focus on modifying the linear theory to predict the effect of an attractor on the internal tide generated by a double ridge.

5.2 Linear theory with dissipation

The Green function solution is modified to satisfy the governing equations with a dissipative term. Otherwise, the inviscid theory fails in the presence of attractors because it offers no mechanism to balance the focusing of energy onto the attractive orbit. We first model
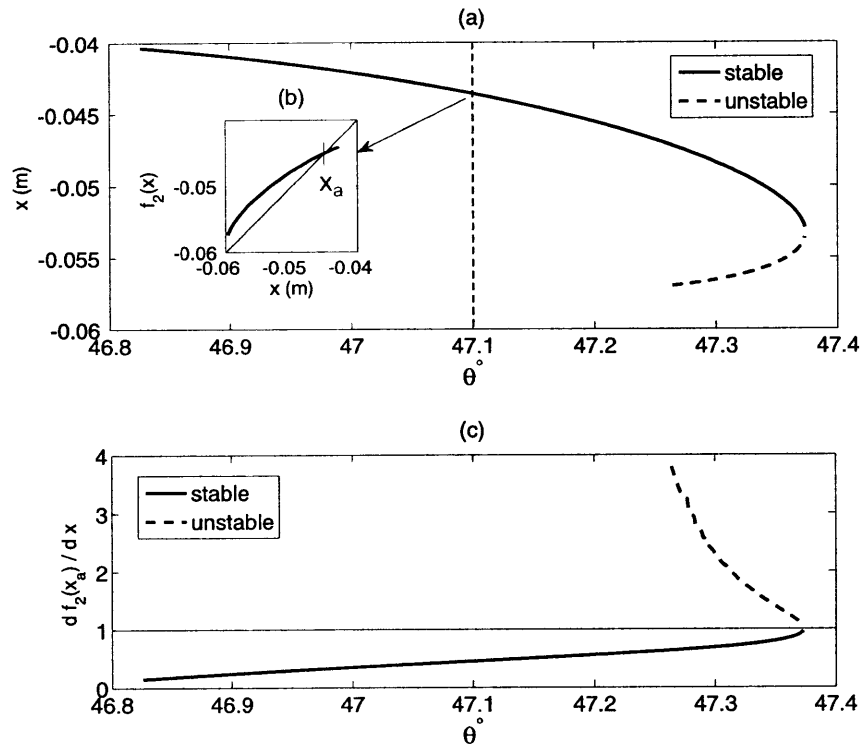
Figure 5-3: (a) Bifurcation sequence showing the pair of closed orbits arising via a saddle-node bifurcation as θ decreases. (b) Second return map for the attractor that exists when $\theta = 47.1°$, which reflects in the valley at the location indicated by the circle in (a), at $x_a = -0.046$ m. (c) Slope of the second return map as a function of θ showing stable (solid line) and unstable (dashed line) closed orbits.

dissipation with a Rayleigh friction term which, although artificial, has been used for ocean dynamics problems [27] and has the property of not changing the form of the internal wave problem. Furthermore, for the sake of comparing the analytical solution with laboratory experiments in section 5.3, one can find a solution of the form prescribed by the problem with Rayleigh friction but that approximately satisfies the fully viscous internal wave equation. This allows us to find a value for the dissipative term that is justified for the physical problem in the laboratory. Finally, since local dissipation is implied in the balance that we seek, we differentiate between the total barotropic to baroclinic conversion rate and the far-field energy flux. The solution presented here concerns a system such as is set up in the laboratory, with a uniform density stratification and with no background rotation.

5.2.1 Modification to the Green function solution

The internal tide solution of chapter 4 can be modified to solve the internal wave problem with dissipation. In a viscous fluid, the dissipative term $D\mathbf{u}$ appears on the right hand side of the momentum equation (1.2.25) to (1.2.27), where the operator is

$$D = \nu_j(-\nabla^2)^j, \tag{5.2.1}$$

with $j = 1$, and $\nu_1 = \nu$ is the kinematic viscosity of the fluid. The kinematic viscosity of salt water for the range of densities found in the experimental stratifications is $\nu = 1.07 \times 10^{-6} \pm 0.01 \, \mathrm{m^2/s}$ in the absence of background rotation. The internal wave equation (1.2.33) therefore becomes

$$\left[-\omega_0^2\left(1 + \frac{iD}{\omega_0}\right) + N^2\right]\phi_{xx} - \omega_0^2\left(1 + \frac{iD}{\omega_0}\right)\phi_{zz} = 0. \tag{5.2.2}$$

We begin by modeling dissipation as Rayleigh friction instead of physical viscosity, and set $j = 0$ in equation (5.2.1), where now ν_0 is the Rayleigh friction coefficient, and D is simply a constant in equation (5.2.2). Equation (5.2.2) can be made dimensionless using X and Z as defined in (3.1.1):

$$\mu^2\phi_{XX} - (1 + i\alpha)^2\phi_{ZZ} = 0, \tag{5.2.3}$$

134

where the inverse slope of the internal wave rays is still

$$\mu = \frac{\sqrt{N^2 - \omega_0^2}}{\omega_0}, \tag{5.2.4}$$

and, assuming that $D \ll 1$ and therefore neglecting higher order terms in D,

$$\alpha = \frac{DN^2}{2\omega_0(N^2 - \omega_0^2)}. \tag{5.2.5}$$

The modified problem for the Green function is therefore

$$G_{XX} - (1 + i\alpha)^2 G_{ZZ} = i\delta(X - X')\delta(Z - Z'), \tag{5.2.6}$$

with homogeneous boundary conditions in Z, $G(X, X'; 0, Z') = G(X, X'; \pi, Z') = 0$, and the radiation condition in X. The Green function that solves equation (5.2.6) is found following the procedure of section 3.1.1:

$$G(X, X'; Z, Z') = \sum_{p=1}^{\infty} \frac{1}{\pi p(1 + i\alpha)} \sin(pZ') \sin(pZ) e^{ip(1+i\alpha)|X-X'|}. \tag{5.2.7}$$

Except for this modified expression for the Green function, the solution to the internal tide problem expressed as a distribution of sources $\gamma(X)$ over the topography is unchanged from (4.1.43). Substituting $G(X, X'; Z, \hat{h}(X'))$ from (5.2.7) into (4.1.43) yields the solution

$$\phi(X, Z) = \frac{H}{\pi} \sum_{p=1}^{\infty} \frac{\sin pZ}{\pi p(1 + i\alpha)} \int_{-a}^{b} \gamma(X') \sin p\hat{h}(X') e^{ip(1+i\alpha)|X-X'|} dX'. \tag{5.2.8}$$

In the far field, for $X \leq -a$ and $X \geq b$,

$$\phi^{\pm}(X, Z) = \frac{H}{\pi} \sum_{p=1}^{\infty} \gamma_p^{\pm} \frac{\sin pZ}{\pi p(1 + i\alpha)} e^{\pm ip(1+i\alpha)X} dX', \tag{5.2.9}$$

indicated by the superscripts '-' and '+', respectively, where

$$\gamma_p^{\pm} = \frac{1}{\pi} \int_{-a}^{b} \gamma(X') \sin p\hat{h}(X') e^{\mp ip(1+i\alpha)X'} dX'. \tag{5.2.10}$$

The boundary condition is solved numerically for $\gamma(X)$ as discussed in section 4.1.4.

135

5.2.2 Correction for viscous dissipation

The effect of physical viscosity can be incorporated as a correction to the inviscid model as it was done in section 3.1.3. We assume the functional form of the inviscid solution (which is unchanged for Rayleigh friction) is:

$$\phi(x, z) \propto \sin\left(\frac{p\pi z}{H}\right) e^{ipq_p|x-x'|}, \tag{5.2.11}$$

and allow q_p to be complex such that the wave field may decay because of viscosity as it propagates away from x'. If the solution (5.2.11) satisfies the viscous internal wave equation, the operator in (5.2.1) becomes

$$D = -\nu p^2 \left[q_p^2 + \left(\frac{\pi}{H}\right)^2 \right]. \tag{5.2.12}$$

Substituting (5.2.11) and (5.2.12) into equation (5.2.2) yields a fourth order polynomial equation for q_p that is equivalent to equation (3.1.65) for the viscous correction $k_p = pq_p$ of chapter 3. Following the perturbative procedure of section 3.1.3, we choose the dominant root that allows the solution to decay away from x'. This root is taken to be a correction of the corresponding inviscid term to the leading order in ν:

$$q_p = \frac{\pi}{\mu H} \left[1 + \frac{i\nu}{2\omega} \left(\frac{p\pi}{H}\right)^2 \left(\frac{N^2}{N^2 - \omega^2}\right)^2 \right]. \tag{5.2.13}$$

In non-dimensional coordinates, we recover the correction

$$\kappa_p = 1 + \frac{i\nu}{2\omega} \left(\frac{p\pi}{H}\right)^2 \left(\frac{N^2}{N^2 - \omega^2}\right)^2, \tag{5.2.14}$$

such that

$$\phi(X, Z) \propto \sin pZ \, e^{ip\kappa_p X}. \tag{5.2.15}$$

By comparison with the $(1 + i\alpha)$ factor in the exponential of the solution (5.2.8), we use

$$\alpha = \alpha_p = p^2 \frac{\nu}{2\omega} \left(\frac{\pi}{H}\right)^2 \left(\frac{N^2}{N^2 - \omega^2}\right)^2 \tag{5.2.16}$$

to approximately represent viscous dissipation, and proceed to solve the internal tide problem as outlined in section 5.2.1.

5.2.3 Energetics

Since the attractor will provide a local energy sink, we seek an expression for the energy emanating from the topography. We use the expression found for the inviscid phase-averaged energy flux $< \mathbf{J} >$ in terms of the stream function ϕ that, as discussed in section 3.1.2, is valid when $< \mathbf{J} >$ is integrated over a domain that spans the topography:

$$< \mathbf{J} >= -i\rho_* U^2 \omega_0 \left[\mu^2 (\phi \phi_x^* - \phi^* \phi_x), -(\phi \phi_z^* - \phi^* \phi_z) \right] . \tag{5.2.17}$$

Note that this expression accounts for the decay in the energy flux due to dissipation, since the solution $\phi(X, Z)$ in (5.2.9) decays as it propagates away from x'.

A convenient expression for the energy flux directly over the topography is found in Echeverri, Balmforth and Peacock [19]. Applying the differential operator

$$D_{IW} = \frac{\partial^2}{\partial X^2} - (1 + i\alpha)^2 \frac{\partial^2}{\partial Z^2} \tag{5.2.18}$$

to the internal wave field $\phi(X, Z)$ from the solution (4.1.43), and using equation (5.2.6) to simplify the result, yields

$$
\begin{aligned}
\phi_{XX} - (1 + i\alpha)^2 \phi_{ZZ} &= i \int_{-a}^{b} \gamma(X') \delta(X - X') \delta[Z - \hat{h}(X')] dX' \\
&= i\gamma(X) \delta[Z - \hat{h}(X)]. \tag{5.2.19}
\end{aligned}
$$

Equation (5.2.19) is the internal wave equation forced by the sources $\gamma(X)$ distributed along the topography, and therefore captures the internal tide generation problem. An expression for the divergence of the energy flux can be obtained by applying the following operation:

$$\phi^*(5.2.19) - \phi(5.2.19)^*, \tag{5.2.20}$$

where the superscript '*' denotes a complex conjugate. This yields

$$
\begin{aligned}
(\phi^* \phi_X &- \phi \phi_X^*)_X - (1 - \alpha^2)(\phi^* \phi_Z - \phi \phi_Z^*)_Z - 2i\alpha(\phi^* \phi_Z + \phi \phi_Z^*)_Z + 4i\alpha |\phi_Z|^2 \\
&= i \left[\gamma(X) \phi^*(X, \hat{h}(X)) - \gamma^*(X) \phi(X, \hat{h}(X)) \right] \delta[Z - \hat{h}(X)]. \tag{5.2.21}
\end{aligned}
$$

Using the boundary condition (1.2.36), which in terms of the dimensionless X is

$$\phi(X, \hat{h}(X)) = \hat{h}(X), \tag{5.2.22}$$

the right hand side of equation (5.2.21) becomes

$$i\hat{h}(X)[\gamma(X) + \gamma^*(X)]\delta[Z - \hat{h}(X)] = 2i\Re[\gamma(X)]\hat{h}(X)\delta[Z - \hat{h}(X)]. \tag{5.2.23}$$

Hence,

$$\nabla \cdot \mathcal{J} = \frac{\partial \mathcal{J}_X}{\partial X} + \frac{\partial \mathcal{J}_Z}{\partial Z} = 2\Re[\gamma]H\delta(Z - H) - \mathcal{D}, \tag{5.2.24}$$

where we use a dimensionless form of the inviscid energy flux, $\mathcal{J} = (\mathcal{J}_X, \mathcal{J}_Z)$, with

$$\mathcal{J}_X = i(\phi\phi_X^* - \phi^*\phi_X) \tag{5.2.25}$$

and

$$\mathcal{J}_Z = -i(\phi\phi_Z^* - \phi^*\phi_Z). \tag{5.2.26}$$

Dissipation and the correction to the energy flux due to the dissipative term are captured by the additional term

$$\mathcal{D} = 4\alpha|\phi_Z|^2 + i\alpha^2(\phi\phi_Z^* - \phi^*\phi_Z)_Z - 2\alpha|\phi|_{ZZ}^2. \tag{5.2.27}$$

Integrating equation (5.2.24) over the region above but not including the topography, $-a \leq X \leq b$ and $\hat{h}(X) < Z \leq \pi$, the source term disappears:

$$\int_{-a}^{b}\int_{\hat{h}(X)^+}^{\pi} \nabla \cdot \mathcal{J}\,dZ\,dX = -\int_{-a}^{b}\int_{\hat{h}(X)^+}^{\pi} \mathcal{D}\,dZ\,dX, \tag{5.2.28}$$

where $Z = \hat{h}(X)^+$ is a limiting value from above. Using Green's theorem, the volume integral on the left hand side of equation (5.2.28) can be re-written as a surface integral over all the boundaries of the domain

$$\int_{0}^{\pi} \mathcal{J}_X(b, Z)dZ - \int_{0}^{\pi} \mathcal{J}_X(-a, Z)dZ - \int_{-a}^{b} [\mathcal{J}_Z(X, \hat{h}^+) - H_X\mathcal{J}_X(X, \hat{h}^+)]dX \equiv C_*^+ + C_*^- - \mathcal{T},$$
$$\tag{5.2.29}$$

where the integral of the energy flux through the surface is zero. The depth-integrated

138

energy flux at the right and left ends of the topography is equivalent to the dimensionless far-field conversion rate $C_*^{\pm}$ used in chapter 4. The remaining term, $\mathcal{T}$, represents the total energy flux emanating from immediately above the topography. The expression,

$$\mathcal{T} - C_*^- - C_*^+ = \int_{-a}^b \int_{\hat{h}(X)}^{\pi} \mathcal{D} dZ dX, \tag{5.2.30}$$

therefore corresponds to balancing the energy dissipation with the difference between the fluxes into and out of the region.

Instead of integrating over the region above the topography, we may also integrate over the domain, $-a \leq X \leq b$ and $0 \leq Z \leq \pi$. In this case, we pick up the contribution of the source, together with integrals over the region below the topography. Below the topography the solution is simply $\phi = Z$ (satisfying the only two relevant conditions, $\phi(X,0) = 0$ and $\phi(X,\hat{h}) = \hat{h}$), and, correspondingly, the integrals over $Z = 0$ and $Z = H$ vanish, leaving

$$\int_0^{\pi} \mathcal{J}_X(b,Z)dZ - \int_0^{\pi} \mathcal{J}_X(-a,Z)dZ = 2 \int_{-a}^b \Re[\gamma(X)]\hat{h}(X)dZdX - \int_{-a}^b \int_{\hat{h}(X)}^{\pi} \mathcal{D} dZ dX. \tag{5.2.31}$$

Comparing equations (5.2.30) and (5.2.31) provides the useful identity [75]

$$\mathcal{T} = \int_{-a}^b [\mathcal{J}_Z(X,\hat{h}) - \hat{h}_X \mathcal{J}_X(X,\hat{h})]dX = 2 \int_{-a}^b \Re[\gamma(X)]\hat{h}(X)dZdX. \tag{5.2.32}$$

5.2.4   The role of dissipation

The inviscid solution, which does not include a dissipative term to balance the focusing of energy when an internal wave attractor is present, does not converge as the parameters K and P (introduced in section 4.1.4) that govern the numerical resolution of the solution are increased. Incorporating the models of dissipation discussed above allows the solution to converge even in the presence of an attractor.

As an example, figure 5-4 shows existing closed orbits in a cosine-shaped double ridge of the form

$$\hat{h}(X) = \begin{cases} B\left[1 - \cos\left(\frac{2\pi X}{A}\right)\right], & |X| \leq A \\ 0, & A < |X| \leq L \end{cases} \tag{5.2.33}$$

The half-width of the ridge is $A = 1.6\pi$ and height is twice the amplitude $B = 1.15$. The closed orbits, shown in the corresponding 1-D map and in the (X,Z)-plane, are symmetric
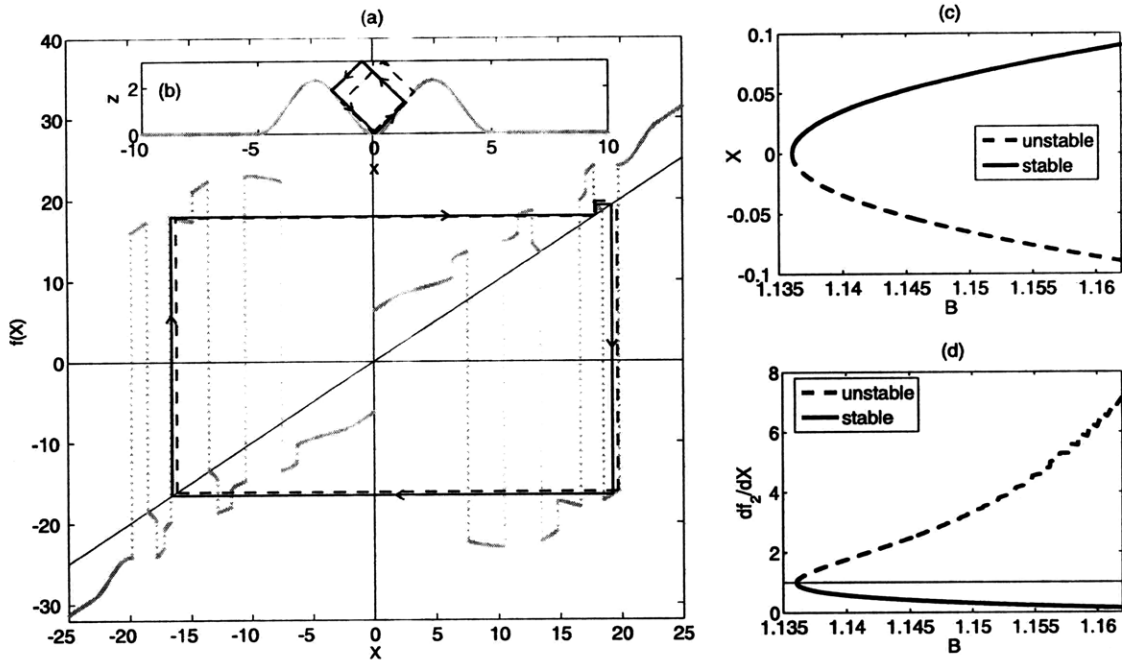
Figure 5-4: (a) 1-D map for upward reflections in a double cosine ridge with $A = 1.6\pi$ and $B = 1.15$, showing a pair of closed ray paths. (b) The corresponding close orbits in the (X, Z) domain. Bifurcation diagrams for the (c) existence and (d) stability of the closed orbits. In all figures, stability and instability are indicated by solid and dashed lines, respectively.

about $X = 0$; for rays traveling in the anticlockwise direction, the right-most one is stable and the left-most one is unstable. A similar pair of symmetric closed orbits exists for the double-cosine configuration in the range $B \sim [1.135 : 1.17]$, as illustrated in the bifurcation diagrams in figures 5-4(c) and (d).

Figure 5-5 and 5-6, which are reproduced from Echeverri et $al.$ [19], were generated by Professor Neil Balmforth to illustrate the effect of adding dissipation to the solution for the double cosine (5.2.33). Figures 5-5(a-c) present the scaled total energy flux [7],

$$M = \frac{2\mathcal{T}}{\pi B^2}, \tag{5.2.34}$$

over the double cosine ridge as a function of the cosine amplitude B, evaluated using the solution of section 5.2.1 and the dissipation parameters $\alpha = 0$, $\alpha = 10^{-3}$ and $\alpha = 10^{-7}p^2$, respectively. For the inviscid solution, which is recovered by setting $\alpha = 0$, the solution only

converges as P and K are increased outside the range in which the construction of figure 5-4 predicts that attractive closed orbits exist. This numerical result suggests that the inviscid solution does not exist in this regime. On the other hand, the solution converges even in the presence of an attractor when dissipation is modeled either as Rayleigh friction, with a small constant value of the dissipation parameter $\alpha = 10^{-3}$, or as physical viscosity with $\alpha = 10^{-7}p^2$, as shown in figures 5-5(b) and (c), respectively. This result indicates that dissipation counterbalances the energy pile-up on the attractor. Moreover, we now observe reliably a substantial enhancement in the conversion rate (by an order of magnitude) at parameter settings close to where the attractor first appears.

The effect of varying the viscosity coefficient, α, for Rayleigh friction is illustrated in figure 5-6(a). The sharpness and height of the peak in the conversion rate are influenced by the level of dissipation, although elsewhere the data collapse onto a common curve. The computations suggest that if α is sufficiently small, the conversion rate converges to a curve that is independent of the precise value of the viscosity, or indeed its form, as illustrated by the results for standard viscosity in figure 5-6(b). What remains unclear is whether the peak remains finite as $\alpha \to 0$. The convergence to a drag-independent value would be analogous to the results of the asymptotic analysis by Ogilvie [69] for inertial wave attractors.

Figure 5-6(b) presents a comparison between the total conversion rate, M, and the scaled outgoing flux, $2(C_*^+ + C_*^-)/\pi B^2$. In contrast to the total conversion rate, the outgoing flux is a much smoother function of B, and, although it is comparable to $M(A, B)$ away from the window in which the attractor exists, there is a significant difference over that window, reflecting the dissipation on the attractor. Thus, the appearance of the attractor coincides with a significant increase in energy conversion, with most of the energy focussed onto that geometrical structure, where it is dissipated.

5.3 Experimental results

An experimental study was performed to assess the ability of the modified linear theory to predict the internal tide generated by a double-ridge configuration that would sustain an internal wave attractor. As mentioned previously, the topography used for the laboratory experiments was a double Gaussian ridge of the form in (5.1.1), with peak heights $h_1 = 0.113 \pm 0.001\,\mathrm{m}$ and $h_2 = 0.225 \pm 0.001\,\mathrm{m}$, equal characteristic peak widths $4\sigma = 0.105 \pm$
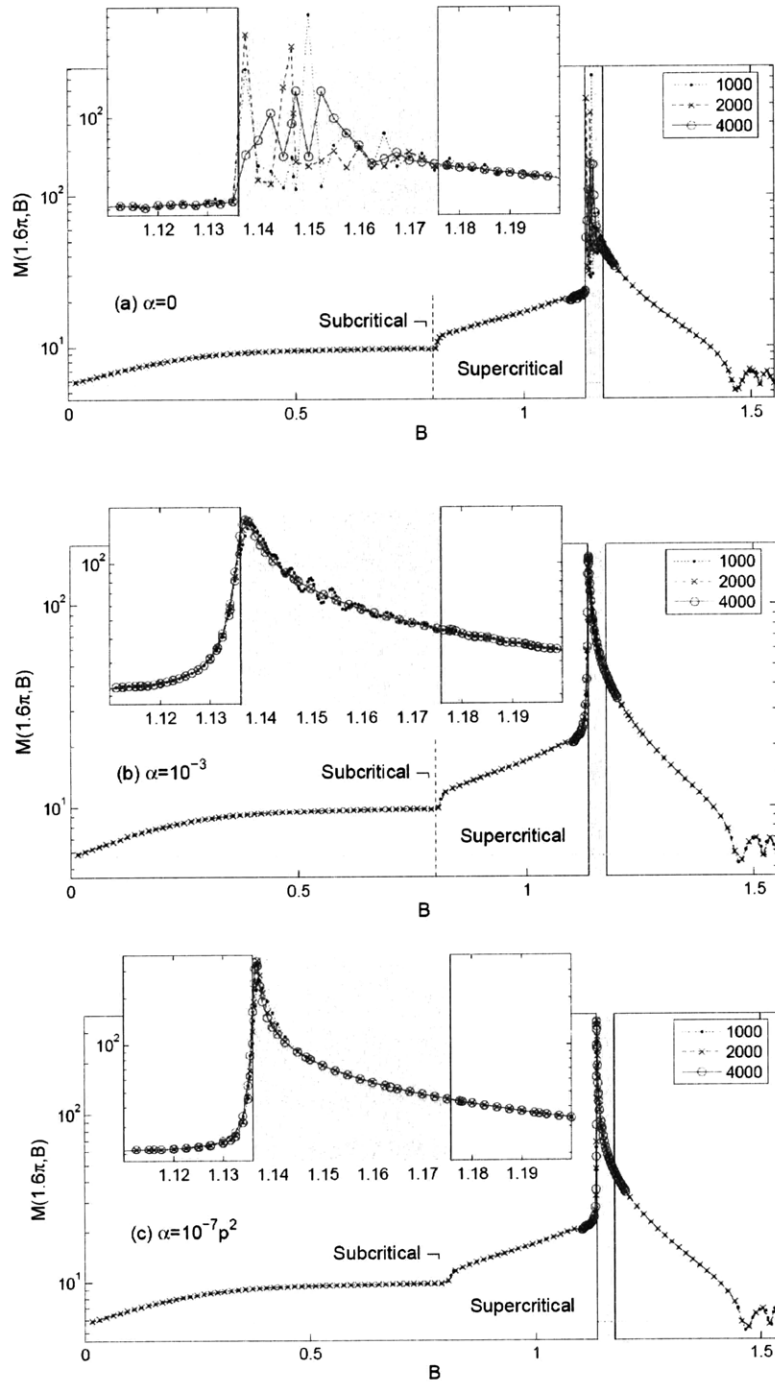
Figure 5-5: Conversion rates for $A = 1.6\pi$ and varying B for (a) α=0, (b) $\alpha = 10^{-3}$ and (c) $\alpha = 10^{-7}p^2$. An attractor appears over the range of values for B that are shaded. The results for different resolution (K and P) fail to show any sign of convergence over this range for the inviscid solution, but converge for the two different types of viscous solutions. Reproduced from [19].
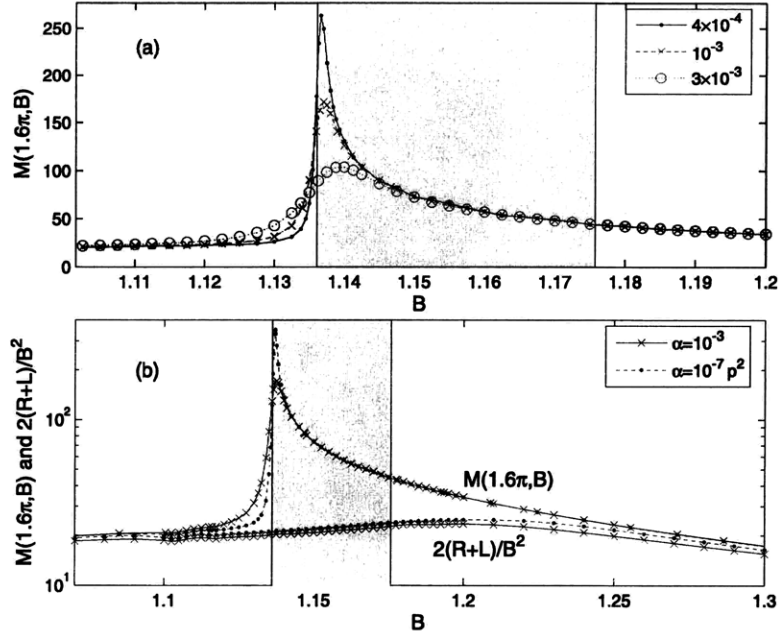
Figure 5-6: Conversion rates, $M(A, B) = 2T/\pi B^2$, for computations with $\alpha = 10^{-3}$ and $\alpha = \alpha_p = 10^{-7}p^2$. Also shown are the scaled left-right fluxes, $2(\mathcal{R} + \mathcal{L})/\pi B^2$. Reproduced from [19].

0.001 m, and a separation $L = 0.302 \pm 0.001$ m between the ridges. The stratification was linear with $N = 1.01 \pm 0.01$ rad/s and the channel depth far away from the ridge was $H = 0.296 \pm 0.001$ m. To generate a linear internal wave field with no initialization transients, the motion of the topography was ramped-up to a sinusoid over five periods of oscillation, as specified by equation (2.1.5), to a maximum amplitude of oscillation $A = 5 \times 10^{-4}$ m. The only parameter that was varied during these experiments was the frequency of oscillation, ω_0, which was selected such that the wave beams propagated at angles to the horizontal $\theta = 29.4 \pm 0.9°$, $\theta = 47.1 \pm 0.8°$ and $\theta = 54.9 \pm 1.3°$. For $\theta = 47.1°$ there is one stable orbit for internal wave rays, as indicated in figure 5-3. For all the experiments presented here, both ridges were supercritical and the excursion parameter was small: $\chi = A/2\sigma = 2 \times 10^{-2}$.

The internal wave field was measured using PIV. The field of view spanned the area between the two ridges $x = [-14.7 : 14.7]$ cm, with small bands of image loss on the tank wall and over the topography, which were typically ~ 5 mm-wide, due to laser sheet scattering. For the experiment with $\theta = 47.1°$, however, the unresolved band was ~ 1 cm wide because the velocity vectors close to internal wave reflections on the topography were too large to

143
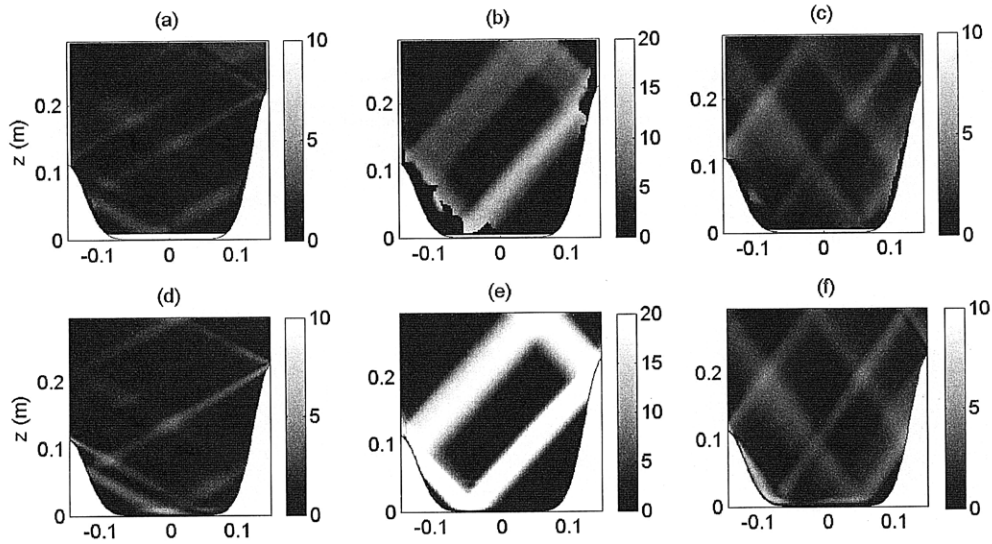
Figure 5-7: Experimental and theoretical snapshots of the velocity magnitude between the ridges. (a)-(c) present experimental results for $\theta = 29.4°, 47.1°, 54.9°$ respectively, and (d)-(f) are the corresponding viscous theoretical results.

be resolved by the PIV algorithm for the specific spatial and temporal resolution, which was chosen to capture the complete region between the ridges and several periods of tidal forcing. The experiment was run for approximately 20 periods before recording a movie for 16 to 18 periods at 16 frames per period of oscillation. The periodicity of the wave fields captured confirmed that a steady state was achieved.

Snapshots of the relative magnitude of the perturbation velocity in experiments, $|\mathbf{u}|/U$, are presented in figures 5-7(a), (b) and (c) for $\theta = 29.4 \pm 0.9°, 47.1 \pm 0.8°$ and $54.9 \pm 1.3°$, respectively. The corresponding viscous analytical results are presented in figures 5-7(d), (e) and (f). A very clean experimental wave field was produced for both the smallest and largest propagation angles, with velocity magnitudes comparable to the tidal forcing, and excellent qualitative agreement between experiment and theory. For $\theta = 47.1°$, there was a dramatic increase in the strength of the internal tide between the ridges, with vertical velocities more than 15 times stronger than the barotropic tidal forcing, corresponding to the existence of the internal wave attractor. The intensity of the wave field between the ridges overwhelms all other features in the wave field.

A quantitative comparison of experimental and theoretical results is presented in figure 5-8, which presents the amplitude envelope of the relative vertical velocity, w/U, for the vertical cross section at $x = 0.05$ m. For $\theta = 29.4°$ and $54.9°$ there is very close quantitative

144
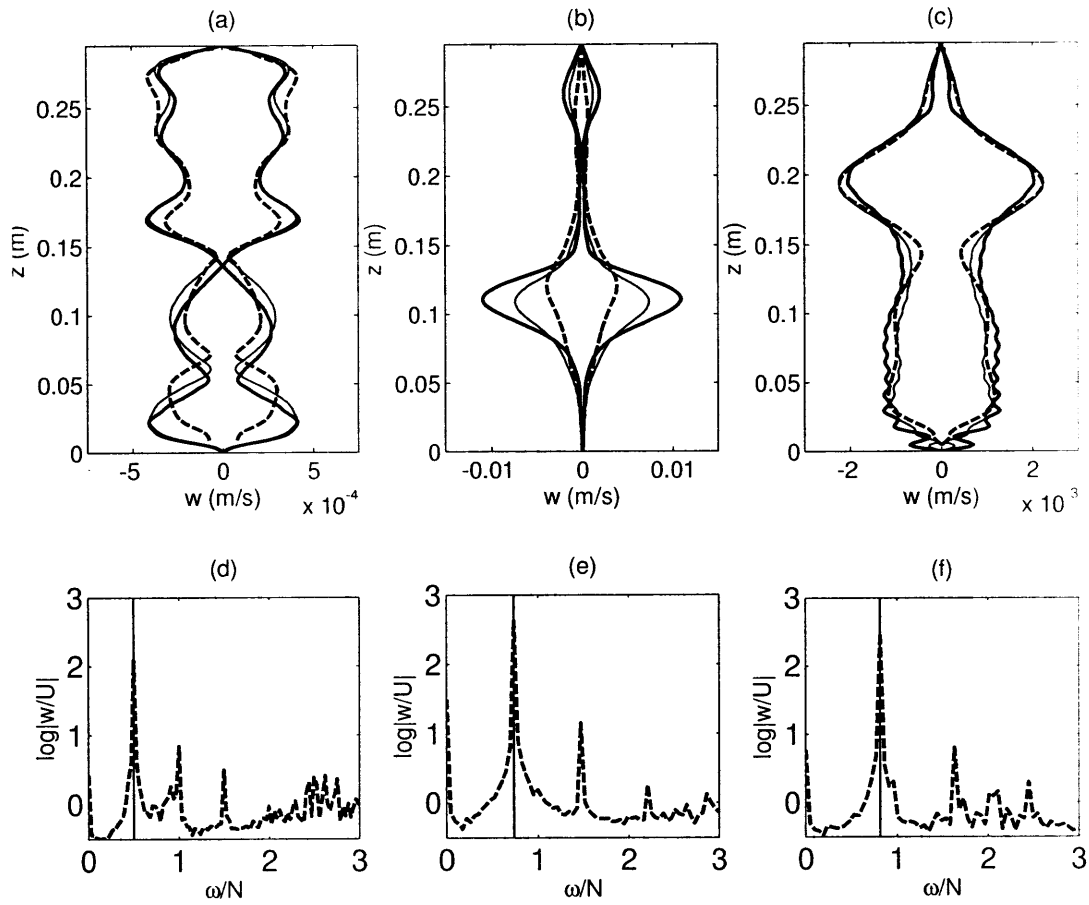
Figure 5-8: (a) and (b) Comparisons of experimental and theoretical vertical velocity profiles envelopes at $x = 0.05\,\mathrm{m}$ for (a,d) $\theta = 29.4°$, (b,e) $47.1°$, and (c,f) $54.9°$. (d–f) Depth averaged frequency spectrum between the ridges.

agreement. For $\theta = 47.1°$, when the attractor is present, the agreement is still very good but theory over predicts the strength of the wave field by about a factor of two to three. The fine dashed lines in these plots indicate the variability of the analytical solution within experimental error. These errors have little impact in the absence of an attractor, but in the presence of an attractor even a small uncertainty in the governing parameters produces substantial changes in the prediction. The corresponding depth-averaged frequency spectra for these vertical profiles is presented in figures 5-8(d) to (f). All the wave fields show a dominant peak at the forcing frequency and first and second harmonic peaks always at least an order of magnitude lower.

Overall, the level of agreement between experiment and theory is remarkably good given that viscosity has only been introduced into the theory in a perturbative manner that ignores viscous boundary layers over the topography, which will almost certainly impact the beam structure to some extent. Furthermore, the analytical model is linear whereas a wave field as strong as that in figure 5-7(b) is likely to introduce nonlinearity. Thus, the perturbative, linear theory is doing a remarkably good job in this challenging regime.

5.4 Discussion and contributions

The present study investigates internal tide generation at tall double ridges as a situation in nature where internal wave attractors may appear. We have presented an analytical model for internal wave attractors that accounts for the necessary balance between energy focusing and dissipation on an attractor. The experiments performed confirm that internal tide energy can be focused by an internal wave attractor in a double-ridge configuration, and also serve to test the analytical model.

This study differs from previous studies of attractors ([56], [35], [31]) as it considers an open domain where it is possible for internal wave rays to escape, so a method was developed to assess the existence and stability of attractors in double ridge systems as a function of the geometric configuration parameters. Using ray tracing, 1-D maps of subsequent internal wave ray reflections on the topography were constructed. For example, the 1-D maps were used here to find, for a simple geometric configuration, the angle of propagation at which a single stable orbit with a single surface reflection would occur. This streamlined scenario was easy to investigate in the laboratory. The method can be used on other double ridges to survey other geometric parameters, and there is a rich parameter space in which attractors may arise. For the other example presented here with a double cosine ridge, as the height of the topography increases a pair of orbits arise that are symmetric about $x = 0$ and have opposite attraction characteristics for rays propagating in a given direction around the valley.

In the presence of an attractor, the inviscid Green function solution method of internal tide generation fails to converge because the continual focusing of energy onto the attractor ensures no time-periodic solution exists. We found that incorporating a viscous correction into this method enabled convergence to a solution. Given the assumptions of linearity and

weak viscosity, remarkably good agreement was obtained between experiment and theory for an internal wave attractor between an asymmetric pair of Gaussian ridges.

There is widespread interest in ascertaining whether internal wave attractors are robust enough to exist in geophysical systems, where they are compromised by competing physical processes. A prior field study of the Mozambique channel, for example, found no evidence of an attractor [59]. While the chances of the existence of geophysical attractors are perhaps slim, the double ridge configuration offers one of the most plausible scenarios. An example is the Luzon ridge, where preliminary ray studies using field data suggest the existence of attracting closed ray paths along a substantial northern portion of the ridge [87].

Chapter 6

Conclusions

The work presented in this thesis addresses the generation of internal tides by tall submarine ridges, which are significant sources of baroclinic energy in the ocean, using a combined analytical and experimental approach, together with comparisons to numerical and field studies. An existing Green function solution method to internal tide generation by topography was first assessed through an experimental investigation, for which the experimental apparatus was designed and constructed, and through comparisons with numerics. Thereafter, this Green function method was advanced to address more complicated topography and non-uniform stratifications. The predictions of this new theory were successfully compared with field data and the results of numerical simulations. These studies furthermore revealed the possibility of the existence of internal wave attractors for double ridge systems. A one-dimensional map was developed to allow quick determination of the existence and stability of such attractors, the Green function method was modified to be able to predict the strength of attractors, and the results were successfully compared with a laboratory experiment. Overall, the thesis has developed and tested an analytical approach that can tackle arbitrary two-dimensional topography in non-uniform stratifications, which is a significant advancement of the state-of-the-art.

The pre-existing analytical method focused on symmetric 2-D ridges, with monotonic slopes but otherwise arbitrary height and shape [75], but its predictions had never been confirmed by experimental investigations. The set-up designed to perform this investigation comprised a large wave tank with a mechanism to guide internal wave reflections away from the experimental section. The tank can be filled with arbitrary density stratification profiles,

149

and a precise calibration and measurement procedure was developed to monitor the density profiles using a conductivity and temperature probe. Topographic models of arbitrary cross-sectional shapes were cut out of rigid foam using a hot wire, then mounted inside the tank and oscillated on the horizontal plane with prescribed motion using a computer controlled traverse. A particle image velocimetry system was set-up to visualize the wave fields.

In comparing experiment and theory, a modal decomposition method was developed to characterize the far field modal structure of experimental wave fields, which furthermore provides a way to readily evaluate the barotropic to baroclinic conversion rate. The results of the investigation revealed that theory provides an accurate description of the low-mode structure of the internal tide radiated from a single, tall topographic feature. For such configurations the low modes carry most of the baroclinic energy away from the generation site. Remarkably, the experiments revealed that theory provides reasonable results for the low modes even in finite excursion regimes, suggesting that linear generation models may be used for tidal conversion estimates even in weakly nonlinear regimes. The higher modes, however, were more noticeably affected by small scale structures introduced by nonlinearity, in which case linear theory no longer provides an accurate prediction.

Having confirmed the ability of the Green function solution to reliably predict internal tide generation, this analytical approach was then advanced to address arbitrarily-shaped 2-D topography in non-uniform stratifications, in an effort to provide estimates of internal tide generation by topography more akin to realistic ocean situations. First, this modified approach was used to investigate generation over idealized topography in uniform stratification, considering asymmetric isolated ridges and different configurations of double ridges. These studies revealed that the structure and asymmetry of internal tides can be very sensitive to the topographic configuration, particularly around criticality. It was found that asymmetry in the radiated tide is dramatic for an isolated ridge with one subcritical and one supercritical slope, since subcritical internal wave beams can only propagate over the top of a ridge, whereas two wave beams emerge from supercritical slopes, one going in each direction. For double ridge configurations, internal wave scattering by neighboring topography and local interference of internal wave fields play an important role in the structure and asymmetry of the radiated tide. Interference can be particularly important when the path of internal wave rays coincides in one direction but not in the other, leading to highly-asymmetric far-field internal tides. Whether the effect is to enhance or reduce the far-field

tide is very sensitive to the configuration.

With the additional implementation of the WKB approximation, the advanced Green function solution can be applied to realistic ocean situations. This approach was tested for 2-D cross-sections of the Hawaiian and Luzon ridges, using stratification profiles fitted to field data from the respective sites. Overall, there was good qualitative and quantitative agreement with numerical observations and field studies. For the Hawaiian cross-sections, the estimated 2-D conversion rates were close to the results of 3-D numerical studies and estimates from field measurements, although the ability to make a very close comparison is tempered by a very sensitive (quadratic) dependence of the tidal conversion rate on the barotropic tidal velocity. Perhaps of most significance is that the analytical model captures the observed asymmetries of the baroclinic tide, which is stronger towards the south, as well as the relative amount of baroclinic energy carried by the first two modes. For the cross-sections of the Luzon ridge, the analytical model agreed with the predictions of a high-resolution numerical simulation in regards to the importance of the western ridge. It was determined that the western ridge plays a minor role at the southern part of the strait, where it is deeper, and a more significant role at the north, where it is taller. These studies furthermore reveal that, depending on the local configuration of the western ridge, the effect can be either to enhance or reduce the westward internal tide. The general conclusion of these case studies is that the analytical model, which is simple and computationally inexpensive, can be applied directly to real ocean ridges to obtain a reasonable assessment of internal tide generation.

In supercritical double ridge systems internal wave rays can be reflected several times in the valley between the ridges, and may converge into a closed orbit and thus remain trapped in the valley. An internal wave attractor is said to exist in this case. These structures have only previously been reported for closed experimental geometries, and never for a realistic ocean scenario. In the last part of this thesis, a one-dimensional map of an internal wave beam return to the topography was developed to determine the existence and stability of internal wave limit cycles in double-ridge systems. Furthermore, the Green function analysis was modified with a viscous correction so that the solution, which blows up in the presence of an attractor in an inviscid fluid, converges in configurations with internal wave attractors. This viscous approach reveals that, in the presence of an attractor, a significant fraction of the baroclinic energy can be dissipated locally, and that the maximum amplitude of the

wave field is somewhat independent of the level of dissipation. The analytical approach was tested through a direct comparison with a laboratory experiment using an asymmetric pair of Gaussian ridges. In the absence of an attractor there was excellent agreement (within experimental error) between experiment and theory. In the presence of an attractor, theory over-predicted the strength of the wave field by a factor of two or three, which is remarkably close agreement given that the model assumes a linear wave field yet the velocity perturbation seen in the laboratory is more than ten times greater than the barotropic velocity. An important open question is whether internal wave attractors can exist in the ocean. In nature, several processes may work against internal wave attractors, such as intense dissipation near the ocean surface, and the three-dimensional and transient nature of the environment.

The analytical models considered in this thesis have limitations that must be recognized. The models assume linearity, two-dimensionality, and a weakly varying stratification associated with the WKB approximation. Our studies therefore exclude mechanisms of barotropic to baroclinic energy transfer that require long excursions, such as lee waves or internal wave generation in periodic flows with Froude numbers near one. Furthermore, the assertion of the theory being reasonable at finite excursion parameters is accurate for topography with intermediate depth ratios, for which low modes dominate the flow. The assumption of two-dimensionality is not unreasonable, as the strongest sites of internal tide generation in the ocean are elongated ridges, which are reasonably 2-D. Three-dimensional effects, however, can enhance or reduce the strength of the internal tide, for instance if flow is accelerated through a saddle-point or if it is allowed to flow around rather than over a peak, respectively. Lastly, we are not accounting for higher order effects due to internal wave ray interactions with rapid changes in the stratification.

Overall, this work provides the first substantial experimental tests of models of internal tide generation, as well as advancing the state-of-the-art of internal tide modeling to address realistic topography and stratifications. A motivation for this work was to contribute to the understanding of the origin of internal solitary waves in the South China sea. The analytical method is a useful tool for predicting the generation of baroclinic energy at the Luzon Strait that propagates to the west and ultimately evolves into solitons, in particular to account for the effect of the topography being a double ridge. Further studies to complete the picture of internal tide generation at the Luzon Strait should address other important factors at

the site, such as asymmetric forcing, the intrusion of the Kuroshio, and possible 3-D effects or trans-critical flows at saddle points, for example between the Batanes Islands.

The broader problem of internal tide generation is also wanting of more development. Although tall ridges are efficient sites of internal tide generation, recent calculations using linear models suggest that a lot of barotropic to baroclinic conversion occurs over small 3-D topographic features that are not well resolved. These studies warn that the linear models used tend to overestimate the conversion rates where the small features are supercritical [68]. Today, our understanding of the geographic distribution of internal tides will be improved with better bathymetric resolution together with reliable models of internal tide generation by small 3-D supercritical features. As the understanding improves, it will illuminate the many open questions of the dissipation of internal tides: where this occurs and how it contributes to ocean mixing.

Appendix A

Procedure to fill non-uniform stratifications in the laboratory

Non-uniform stratifications can be filled in the laboratory, as described in section 2.1.2. For this purpose, the system of equations (2.1.1) to (2.1.3) must be solved for the flow rate $f_2(t)$ that is required between the salt-water reservoir and the mixed water reservoir (tank 2). A Cole-Palmer Masterflex peristaltic pump is computer-controlled to transfer water between the reservoirs at the specified flow rate.

Equations (2.1.2) and (2.1.3) can be combined into a single differential equation for $f_2(t)$, which is discretized and solved numerically using an ODE solver in MATLAB [32]. The MATLAB script allows the user to input the desired density profile $\rho(z)$ and to specify the amount of discretization in the form of the number of discrete density layers that make up the final stratification. The user must also input the initial conditions for filling ($\rho_2(0)$, $V_2(0)$ and ρ_3) and the geometry of the tank A. Finally, the script converts the output $f_2(t)$ into voltages using the voltage to flow rate calibration of the pumps, and outputs a file that contains the corresponding array of voltages. This file is read by the VI that controls the pump during filling. The pump is connected via an RS-232 connection to a computer running a LabVIEW virtual instrument (VI) that constantly outputs a voltage in the range 0–5 V that is proportional to the desired flow rate.

Appendix B

Selected MATLAB routines

The following routines are used to evaluate the internal tide using the Green function method at cross-sections of realistic topographies in section 4.3. Section B.1 includes the routine gammas.m, which is used to solve for the distribution of sources $\gamma(X)$ along the topography $h(X)$. Sections B.2 and B.3 include, respectively, the routines conversion.m and modes.m, which are used to evaluate the modal structure and the directional conversion rates of the corresponding internal tides.

B.1   Distribution of sources $\gamma(X)$

```
%% gammas.m
% Paula Echeverri 2009.04.21 (final version)
%
% This code evaluates the distribution of sources gamma(X) to model the
% topography in problems of internal tides generation by
% realistic 2D topography in weakly non-uniform stratification solved using
% the Green function method.
%
% gammas.m solves a linear problem (n equations) for gamma_(j+1/2)
% (gg below) corresponding to the weights of Green function representation
% of the solution. The linear problem is derived by applying the boundary
% condition to the Green function representation of the solution. The
% Green function is derived using the WKB approximation.
```

```
%
% User provides:
% 1. mat file with stratification data:
%    'dre' depth (m)
%    'Nre' buoyancy frequency (rad/s).
% 2. mat file with bathymetry data
%    'etare' distance across (m)
%    'hre' depth (m)
% (note: hre is depth data, therefore zero at the ocean surface
%    and negative downward)
% 3. 'omega' tidal frequency (rad/s)
% 4. 'f' Coriolis frequency (rad/s)
% 5. 'exptname' string to use as a descriptive experiment name
%
% Code outputs:
% 1. mat file with the name (and file path) specified in the variable
%    exptname.  The file contains a structure called 'solution' containing
%    the following variables:
%    'gammas', distribution of sources gamma(X) along the topography
%    'xdomain', dimensionless X domain
%    'Del', size of horizontal internal
%    'nz', vertical resolution
%    'topography', mid-interval value of topography as a function of X
%    'stretch', stretched shape of the topography
%    'Nbar', depth-averaged buoyancy frequency
%    'Ho', ocean depth
%    'omega', omega,
%    'N', buoyancy frequency profile
%    'cN_HH', boundary value of curly N (evaluated at the topography)


global pp Ho Nbar omega N
```

```matlab
%% physical configuration
% topography data
%number = int2str(180);
topography = ['geodata\new_luzon', number, '.mat'];
load(topography)
x_topo = etare;
h_topo = hre - min(hre);
dh_topo = dhre;


% stratification data
load('geodata\NLuzon3')
N_strat = Nre;
D_strat = dre;


% physical geometry
Ho = -min(hre); %(m) ocean depth
b1 = max(h_topo) - min(h_topo);  %(m) height of the bump
omega = 1.4e-004; % (rad/s) tidal frequency M2
f = 5e-005; % (rad/s) Coriolis frequency


% flip stratification data
ii = find(abs(D_strat+Ho) == min(abs(D_strat+Ho)));
No = fliplr(N_strat(1:ii));
do = fliplr(D_strat(1:ii)+Ho);
N = No;


%% numerical resolution
% (here determined by the resolution of the topography data that is provided)
nn = length(x_topo);
pp = nn;
```

```matlab
exptname = ['luzon', number, '_N3_b1H', num2str(100*b1/Ho, '%03.0f'), ...
    '_nn', num2str(nn), '_pp', num2str(pp)]


%% nondimensionalizations
% evaluate relevant parameters: depth averaged N and slope parameter mu
z = do;
nz = length(do);
Delz = z(2) - z(1);
Nbar = sum(sqrt(N.^2 - omega^2))*Delz/Ho;   % depth averaged buoyancy frequency N
mu = Nbar/sqrt(omega^2 - f^2);              % slope parameter mu
    % note: as presented here these are nonhydrostatic and include
    % background rotation


% horizontal coordinate X
X = x_topo*pi/mu/Ho;   % x_n
Del=diff(X);
XX=X(1:end - 1) + Del/2;    % mid-interval values x_(n + 1/2)


% topography
hh_topo = (h_topo(1:end-1) + h_topo(2:end))/2;
        % first find dimensional mid-interval values h_(n+1/2)
dhh_topo = (dh_topo(1:end-1) + dh_topo(2:end))/2;
        % (for topographic height (h) and slope (dh))


Z_t   = Ztfunk(h_topo,z,Delz,0) ;        % stretch h_n into its non-dimensional form
ZZ_t  = Ztfunk(hh_topo,z,Delz,0) ;       % same for h_(n+1/2)
dZZ_t = Ztfunk(dhh_topo,z,Delz,1) ;      % same for (d/dX)(h_(n + 1/2))


%% boundary conditions
% find indices of z at the height of the topography
hhi = zeros(1,length(hh_topo));
for j = 1:length(hh_topo)
```

```matlab
        hhi(j) = find(min(abs(z-hh_topo(j))) == abs(z-hh_topo(j)));
end


% evaluate variables at the height of the topography
N_HH = N(hhi);
cN_HH = (1/Nbar)*sqrt(N_HH.^2 - omega^2);    % cN is  'curly N',
                                             % a new variable defined
                                             % to simplify the WKB solution


%% Solve matrix problem implied by the bottom boundary condition
M=gtfunk(ZZ_t, dZZ_t,cN_HH,X(1:end-1),Del);  % M_nj
LHS = Del.*hh_topo;                          % h^hat(x)*Delta_x
gg = M\LHS';        % gamma^hat ( i.e. gamma^hat_(j+1/2) = gamma^hat(x_(j+1/2)) )


%% Plot and save
figure(100)
% plot dimensionless topography
subplot(2,1,1)
plot(X,Z_t)
ylabel('Z_t(X)')
ylim([0 pi])
% plot gammas
subplot(2,1,2)
plot(XX,real(gg),XX,imag(gg))
xlabel('X')
ylabel('\gamma(X)')
legend('Re(\gamma)','Im(\gamma)')


solution = struct('gammas', gg, 'xdomain', XX, 'Del', Del, 'nz', nz, ...
    'topography', hh_topo, 'stretch', ZZ_t, 'Nbar', Nbar,'Ho', Ho, ...
    'omega', omega, 'N', N, 'cN_HH', cN_HH);
save(['gammas\', exptname], 'solution')
```

% The following functions are used to evaluate the matrix M_nj in gammas.m.

% Mtfunk is called explicitly from gammas.m, and the other supporting

% functions are called from Mtfunk.

% (In order for the latter to run properly they must be saved as

% independent m files with their corresponding function names.)


```
function gg=Mtfunk(HH,HHp,cNN,x,Del)
% inputs: HH (H_(n + 1/2)), HHp (dH_(n + 1/2)), x, Del (diff(x))
% outputs: M_nj (called G in tPLY.m; called gg below and called w_nk in
% Petrelis)
global  pp

nr=max(size(x));
pmax = pp;
U=zeros(pmax,nr);
Uc=zeros(pmax,nr);
J=zeros(size(x));

% find the integrand U
for p=1:pmax % sum over p from fourier series representation of Green function
    U(p,:)=utfunk(p,HH,HHp, cNN,x,Del)/sqrt(pi*p);
    Uc(p,:)=utfunl(p,HH,HHp,cNN,x,Del)/sqrt(pi*p);
    J=J+jtfunk(p,HH,HHp,cNN,x,Del)/pi/p;
end

gg=zeros(nr,nr);
for m=1:nr %evaluate each element of M_nj
    for n=m+1:nr
        gg(m,n)=sum(Uc(:,m).*U(:,n));
        gg(n,m)=gg(m,n);
    end
    gg(m,m)=J(m);
```

```
end


end


%%%%%%%%%%%%%%%%%%%%%%%%%%%%%%%%%%%%%%
function uu=utfunl(p,HH,HHp,cNN,x,Del)


% intermediate variables
t1=p*HH+p/2*HHp.*Del;
t2=p/2*HHp.*Del-p*HH;


% conjugate of the integrand of the linear matrix M_nj
uu = (1./sqrt(cNN)).*conj(((i*sin(t1)-HHp.*cos(t1))+...
     exp(-i*p*Del).*(i*sin(t2)+HHp.*cos(t2)))./...
        (HHp.^2-1)/p.*exp(i*p*x));
end


%%%%%%%%%%%%%%%%%%%%%%%%%%%%%%%%%%%%%%
function uu=utfunk(p,HH,HHp,cNN,x,Del)


% intermediate variables
t1=p*HH+p/2*HHp.*Del;
t2=p/2*HHp.*Del-p*HH;


% integrand of the linear matrix M_nj
% (this expression is obtained using MAPLE)
uu = (1./sqrt(cNN)).*((i*sin(t1)-HHp.*cos(t1))+...
     exp(-i*p*Del).*(i*sin(t2)+HHp.*cos(t2)))./...
        (HHp.^2-1)./p.*exp(i*p*x);
end


%%%%%%%%%%%%%%%%%%%%%%%%%%%%%%%%%%%%%%
```

```
function jj=jtfunk(p,HH,HHp,cNN,x,Del)


% intermediate variables
t1=2*p*HH+p*HHp.*Del;
t2=p*HHp.*Del-2*p*HH;


% integrand of the linear matrix M_nn
% (this expression is obtained using MAPLE)
jj = (1./cNN).*(2*HHp.*(i*p*Del.*(A^2-HHp.^2)*A+A^2+HHp.^2)-...
      (i*sin(t1)*A+HHp.*cos(t1)).*(A^2-HHp.^2)+...
      4*i*HHp.^2.*exp(i*p*Del*A).*sin(p*HHp.*Del)*A+...
      2*HHp.*exp(i*p*Del*A).*(cos(2*p*HH).*(A^2-HHp.^2)-...
                              (A^2+HHp.^2).*cos(p*HHp.*Del))+...
      (i*sin(t2)*A+HHp.*cos(t2)).*(HHp.^2-A^2))/...
        p^2/2./HHp./(A^2-HHp.^2).^2;
end
```

B.2 Conversion rate

```
%% conversion.m
% Paula Echeverri 2008.11.17
%
% conversion.m uses gamma_(j+1/2) (gg below), which are found using
% gammas.m, to evaluate the directional conversion rate


%% parameters
%computational parameters
nm = 100;   % number of modes in reconstructed solution


% physical parameters
f = 5e-005;
t = 0;


%% gammas
load 'gammas\luzon1014_b1H089_inv_nn2100_pp2100'


gg = solution.gammas;
xx = solution.xdomain;
Del = solution.Del;
nz  = solution.nz;
hh = solution.topography;
HH = solution.stretch;
cN_HH = solution.cN_HH;
N  = solution.N;
Nbar  = solution.Nbar;
Ho = solution.Ho;
omega  = solution.omega;


mu = Nbar/sqrt(omega^2 - f^2);
```

```matlab
nr = length(xx);

%% conversion rate
conv=0;
conv_r=0;
conv_l=0;


gamma_r = zeros(1,nm);
gamma_l = zeros(1,nm);


%% Right-ward depth-averaged flux
for p = 1:nm
    for xp=1:nr % for each x
        gamma_r(p) = gamma_r(p) + (1/Ho) * (sin(p*HH(xp)) ./ sqrt(cN_HH(xp)) ) ...
            .* exp(-i*p*xx(xp)) .*gg(xp) .* Del(xp);
        gamma_l(p) = gamma_l(p) + (1/Ho) * (sin(p*HH(xp)) ./ sqrt(cN_HH(xp)) ) ...
            .* exp( i*p*xx(xp)) .*gg(xp) .* Del(xp);
    end
    conv_r=conv_r+abs(gamma_r(p))^2/p;
    conv_l=conv_l+abs(gamma_l(p))^2/p;
end


[conv_l conv_r]
```

B.3 Modal structure

```
%% modes.m
% Paula Echeverri 2008.01.12
%
% modes.m uses gamma_(j+1/2) (gg below), which are found using
% gammas.m, to evaluate and plot the mode strengths.
%
% User provides:
% 'solution' from gammas
% 'nm'


%% parameters
%computational parameters
nm = 10;    % number of modes in reconstructed solution


% physical parameters
f = 5e-005;


%% gammas
load 'gammas\luzon1014_b1H089_inv_nn2100_pp2100'


gg = solution.gammas;
xx = solution.xdomain;
Del = solution.Del;
nz  = solution.nz;
hh = solution.topography;
HH = solution.stretch;
cN_HH = solution.cN_HH;
N  = solution.N;
Nbar  = solution.Nbar;
Ho = solution.Ho;
```

```matlab
omega  = solution.omega;

mu = Nbar/sqrt(omega^2 - f^2);
nr = length(xx);

%% mode strengths
gamma_r = zeros(1,nm);
gamma_l = zeros(1,nm);

for p = 1:nm
    for xp=1:nr % for each x
        gamma_r(p) = gamma_r(p) + (1/Ho) * (sin(p*HH(xp)) ./ sqrt(cN_HH(xp)) ) ...
            .* exp(-i*p*xx(xp)) .*gg(xp) .* Del(xp);
        gamma_l(p) = gamma_l(p) + (1/Ho) * (sin(p*HH(xp)) ./ sqrt(cN_HH(xp)) ) ...
            .* exp( i*p*xx(xp)) .*gg(xp) .* Del(xp);
    end
end

%% plot
figure,
subplot(1,2,2)
plot(1:nm, abs(gamma_r(1:nm)), 'y-*')
xlabel('mode number')
ylabel('|\gamma_n|')
title('rightward wave field')

subplot(1,2,1)
plot(1:nm, abs(gamma_l(1:nm)), '-*')
xlabel('mode number')
ylabel('|\gamma_n|')
title('leftward wave field')
```

Bibliography

[1] *Jane's Defence Weekly*, 2(15), October 1984.

[2] Seed particles for PIV and LDV, TSI Inc., 2006.

[3] J. R. Apel, J. R. Holbrook, A. K. Liu, and J. J. Tsai. The Sulu Sea internal soliton experiment. *J. Phys. Oceanogr.*, 15:1625–1651, 1985.

[4] P. G. Baines. The generation of internal tides by flat-bump topography. *Deep Sea Res.*, 20:179–205, 1973.

[5] P. G. Baines. *Topographic Effects in Stratified Flows*. Cambridge University Press, Cambridge, England, 1995.

[6] N. J. Balmforth, G. R. Ierley, and W. R. Young. Tidal conversion by subcritical topography. *J. Phys. Oceanogr.*, 32:2900–2914, 2002.

[7] N. J. Balmforth and T. Peacock. Tidal conversion by supercritical topography. *J. Phys. Oceanogr.*, 2009. In press.

[8] N. J. Balmforth, E. A. Spiegel, and C. Tresser. Checkerboard maps. *Chaos*, 5(1), 1995.

[9] J. J. Becker, D. T. Sandwell, W. H. F. Smith, J. Braud, B. Binder, J. Depner, D. Fabre, J. Factor, S. Ingalls, S-H. Kim, R. Ladner, K. Marks, S. Nelson, A. Pharaoh, G. Sharman, R. Trimmer, J. vonRosenburg, and G. Wallace. Global bathymetry and elevation data at 30 arc seconds resolution: SRTM30_PLUS, revised for marine geodesy. *Mar. Geod.*, 2009. In press.

[10] T. H. Bell. Lee waves in stratified flows with simple harmonic time dependence. *J. Fluid Mech.*, 67:705–722, 1975.

[11] S. Y. Chao, D. S. Ko, R. C. Lien, and P. T. Shaw. Assessing the west ridge of Luzon Strait as an internal wave mediator. *J. Oceanogr.*, 63:897–911, 2007.

[12] L. H. N. Cooper. Internal waves and upwelling of oceanic water from mid-depths on to a continental shelf. *Nature*, 159:579–580, 1947.

[13] S. B. Dalziel, M. Carr, J. K. Sveen, and P. A. Davies. Simulataneous synthetic schlieren and PIV measurements for internal solitary waves. *Meas. Sci. Technol.*, 18:533–547, 2007.

[14] S. B. Dalziel, G. O. Hughes, and B. R. Sutherland. Whole field density measurements. *Exp. Fluids*, 28:322–335, 2000.

[15] E. Di Lorenzo, W. R. Young, and S. G. Llewellyn Smith. Numerical and analytical estimates of M2 tidal conversion at steep oceanic ridges. *J. Phys. Oceanogr.*, 36:1072–1084, 2006.

[16] T. Duda, J. F. Lynch, J. D. Irish, R. C. Beardsley, S. R. Ramp, C. S. Chiu, T. Y. Tang, and Y. J. Yang. Internal tide and nonlinear internal wave behavior at the continental slope in the northern South China Sea. *IEEE J. Oceanic Eng.*, 29(4):1105–1130, 2004.

[17] P. Echeverri. Experimental investigation of internal tide generation by two-dimensional topography using synthetic schlieren. Master's thesis, Massachusetts Institute of Technology, 2006.

[18] P. Echeverri, M. R. Flynn, K. B. Winters, and T. Peacock. Low-mode internal tide generation by topography: An experimental and numerical investigation. *J. Fluid Mech.*, 2009. In press.

[19] P. Echeverri, T. Yokossi, N. J. Balmforth, and T. Peacock. Internal tide attractors in double ridges. *J. Fluid Mech.*, 2009. Submitted.

[20] G. D. Egbert and R. D. Ray. Significant dissipation of tidal energy in the deep ocean inferred from satellite altimeter data. *Nature*, 405:775–778, 2000.

[21] V. W. Ekman. Internal waves in the sea. *Letters to the Editor. Nature.*, 155, 1945.

[22] D. M. Farmer, Q. Li, and J.Park. Internal wave observations in the South China Sea: the role of rotation and nonlinearity. *Atmos. Ocean.* Submitted.

[23] S. Flatté, editor. *Sound Propagation Through a Fluctuating Ocean*. Cambridge Univ. Press, Cambridge, UK, 1979.

[24] M. R. Flynn, K. Onu, and B. R. Sutherland. Internal wave generation by a vertically oscillating sphere. *J. Fluid Mech.*, 494:65–93, 2003.

[25] C. Garrett and E. Kunze. Internal tide generation in the deep ocean. *Annu. Rev. Fluid Mech.*, 39:57–87, 2007.

[26] T. Gerkema and J.T.F. Zimmerman. *An Introduction to Internal Waves*. Lecture Notes, http://www.nioz.nl/nioz_nl/68993cc95adf64e0b49212da8c6e3ab0.php.

[27] A. E. Gill. *Atmosphere-Ocean dynamics*. Academic Press, San Diego, CA, USA, 1982.

[28] Global Ocean Associates. An atlas of oceanic internal solitary waves. Prepared for Office of Naval Research, Code 322 PO., February 1989.

[29] S. D. Griffiths and R. H. J. Grimshaw. Internal tide generation at the continental shelf modeled using a modal decomposition: Two-dimensional results. *J. Phys. Oceanogr.*, 37:428–451, 2007.

[30] R. H. J. Grimshaw. Wave action and wave-mean flow interaction, with application to stratified shear flows. *Ann. Rev. Fluid Mech.*, 16:11–44, 1984.

[31] N. Grisouard, C. Staquet, and I. Pairaud. Numerical simulation of a two-dimensional internal wave attractor. *J. Fluid Mech.*, 614:1–14, 2008.

[32] V. S. Harris. Creation of nonlinear density gradients for use in internal wave research. Undergraduate Thesis, Massachusetts Institute of Technology, 2007.

[33] Hawaii Mapping Research Group. Main Hawaiian Islands multibeam synthesis, April 2009. http://www.soest.hawaii.edu/HMRG/Multibeam/index.php.

[34] Hawaiian Ocean Time-series, April 2009. http://hahana.soest.hawaii.edu/hot/hot_jgofs.html.

[35] J. Hazewinkel, P. Van Breevoort, S. B. Dalziel, and L. R. M. Maas. Observations on the wavenumber spectrum and evolution of an internal wave attractor. *J. Fluid Mech.*, 598:373–382, 2008.

[36] K. R. Helfrich and W. K. Melville. Long nonlinear internal waves. *Annu. Rev. Fluid Mech.*, 38:395–425, 2006.

[37] T. Hibiya. Generation mechanism of internal waves by a vertically sheared tidal flow over a sill. *J. Geophys. Res.*, 95(C4):1757–1764,, 1990.

[38] D. F. Hill. General density gradients in general domains: The "two-tank" method revisited. *Exp. Fluids*, 32:434–440, 2002.

[39] D. A. Horn, J. Imberger, and G. N. Ivey. The degeneration of large-scale interfacial gravity waves in lakes. *J. Fluid Mech.*, 434:181–207, 2001.

[40] D. G. Hurley and G. Keady. The generation of internal waves by vibrating elliptic cylinders. Part 2: Approximate viscous solution. *J. Fluid Mech.*, 351:119–138, 1997.

[41] G.N. Ivey, K.B. Winters, and J.R. Koseff. Density stratification, turbulence, but how much mixing? *Annu. Rev. Fluid Mech.*, 40:169–184, 2008.

[42] S. Jan, R. C. Lien, and C. H. Ting. Numerical study of baroclinic tides in Luzon Strait. *J. Oceanogr.*, 64:789–802, 2008.

[43] T. M. S. Johnston and M. A. Merrifield. Internal tide scattering at seamounts, ridges, and islands. *J. Geophys. Res.*, 108(C6), 2003.

[44] R. I. Joseph. Solitary waves in a finite depth fluid. *J. Phys. A: Math. Gen.*, 10:L225–L227, 1977.

[45] S. Khatiwala. Generation of internal tides in an ocean of finite depth: Analytical and numerical calculations. *Deep Sea Res., Part I*, 50:3–21, 2003.

[46] J. M. Klymak, J. M. Moum, J. D. Nash, E. Kunze, J. B. Girton, G. S. Carter, C. M. Lee, T. B. Sanford, and M. C. Gregg. An estimate of tidal energy lost to turbulence at the Hawaiian ridge. *J. Phys. Oceanogr.*, 36:1148–1164, 2006.

[47] A. S. Korobov and K. G. Lamb. Interharmonics in internal gravity waves generated by tide-topography interaction. *J. Fluid Mech.*, 611:61–95, 2008.

[48] E. Kunze and S. G. Llewellyn Smith. The role of small-scale topography in turbulent mixing of the global ocean. *Oceanography*, 17:55–64, 2004.

171

[49] K. G. Lamb. Nonlinear interaction among internal wave beams generated by tidal flow over supercritical topography. *Geophys. Res. Lett.*, 31:L09313, 2004.

[50] P. H. LeBlond and L. A. Mysak. *Waves in the Ocean*. Elsevier Scientific Pub. Co., New York, NY, USA, 1978.

[51] C. M. Lee, E. Kunze, T. B. Sanford, J. D. Nash, M. A. Merrifield, and P. E. Holloway. Internal tides and turbulence along the 3000-m isobath of the Hawaiian ridge. *J. Phys. Oceanogr.*, 36:1165–1183, 2006.

[52] S. Legg and K. M. H. Huijts. Preliminary simulations of internal waves and mixing generated by finite amplitude tidal flow over isolated topography. *Deep Sea Res. II*, 53:140–156, 2006.

[53] A. K. Liu, S. R. Ramp, Y. Zhao, and T. Y. Tang. A case study of internal solitary wave propagation during ASIAEX 2001. *IEEE J. Oceanic Eng.*, 29(4):1144–1156, 2004.

[54] S. G. Llewellyn Smith and W. R. Young. Conversion of the barotropic tide. *J. Phys. Oceanogr.*, 32:1554–1566, 2002.

[55] S. G. Llewellyn Smith and W. R. Young. Tidal conversion at a very steep ridge. *J. Fluid Mech.*, 495:175–191, 2003.

[56] L. R. M. Maas, D. Benielli, J. Sommeria, and F. P. A. Lam. Observation of an internal wave attractor in a confined stably-stratified fluid. *Nature*, 388:557–561, 1997.

[57] L. R. M. Maas and F. P. A. Lam. Geometric focusing of internal waves. *J. Fluid Mech.*, 300:1–41, 1995.

[58] J. A. MacKinnon and K. B. Winters. Subtropical catastrophe: Significant loss of low-mode tidal energy at 28.9°. *Geophys. Res. Lett.*, 32:L15605, 2005.

[59] A. M. M. Manders, L. R. M. Maas, and T. Gerkema. Observations of internal tides in the Mozambique channel. *J. Geophys. Res.*, 109:C12034, 2004.

[60] T. Maxworthy. A note on the internal solitary waves produced by tidal flow over a three-dimensional ridge. *J. Geophys. Res.*, 84:338–346, 1979.

[61] M. A. Merrifield and P. E. Holloway. Model estimates of M2 internal tide energetics at the Hawaiian ridge. *J. Geophys. Res.*, 107(C8), 2002.

[62] W. H. Munk and C. Wunsch. Abyssal recipes II: Energetics of tidal and wind mixing. *Deep Sea Res.*, 45:1977–2010, 1998.

[63] F. Nansen. *The Norwegian North Polar Expedition, 1893-1896: Scientific Results*. Longmans, Green and co., 1906.

[64] J. D. Nash, E. Kunze, C. M. Lee, and T. B. Sanford. Structure of the baroclinic tide generated at Kaena Ridge, Hawaii. *J. Phys. Oceanogr.*, 36:1123–1135, 2006.

[65] National Geophysical Data Center, National Oceanic and Atmospheric Administration, U.S. Department of Commerce. 2-minute gridded global relief data (ETOPO2v2), 2006. http://www.ngdc.noaa.gov/mgg/fliers/06mgg01.html.

[66] Y. Niwa and T. Hibiya. Three-dimensional numerical simulation of M2 internal tides in the East China Sea. *J. Geophys. Res.*, 109:C04027, 2004.

[67] J. Nycander. Generation of internal waves in the deep ocean. *J. Geophys. Res.*, 110:C10028, 2005.

[68] J. Nycander. Tidal generation of internal waves from a periodic array of steep ridges. *J. Fluid Mech.*, 567:415–432, 2006.

[69] G. I. Ogilvie. Wave attractors and the asymptotic dissipation rate of tidal disturbances. *J. Fluid Mech.*, 543:19–44, 2005.

[70] A. R. Osborne and T. L. Burch. Internal solitons in the Andaman Sea. *Science*, 208:451–460, 1980.

[71] A. R. Osborne, T. L. Burch, and R.I. Scarlet. The influence of internal waves on deep-water drilling. *J. Pet. Technol.*, 30(10):1497–1504, 1978.

[72] G. Oster. Density gradients. *Sci. Am.*, 213:70, 1965.

[73] T. Peacock, P. Echeverri, and N. J. Balmforth. An experimental investigation of internal tide generation by two-dimensional topography. *J. Phys. Oceanogr.*, 38:235–242, 2008.

[74] T. Peacock and A. Tabaei. Visualization of nonlinear effects in reflecting internal wave beams. *Phys. Fluids*, 17:061702, 2005.

[75] F. Pétrélis, S. G. Llewellyn Smith, and W. R. Young. Tidal conversion at a submarine ridge. *J. Phys. Oceanogr.*, 36:1053–1071, 2006.

[76] O. Pettersson. On the occurrence of lunar periods in solar activity and the climate of the Earth. *Svenska Hydrografiskbiologiska Kommissionens Skrifter*, 5, 1914.

[77] K. L. Polzin, J. M. Toole, J. R. Ledwell, and R. W. Schmitt. Spatial variability of turbulent mixing in the abyssal Ocean. *Science*, 276:93–96, 1997.

[78] L. Rainville and R. Pinkel. Baroclinic energy flux at the Hawaiian ridge: Observations from the R/P FLIP. *J. Phys. Oceanogr.*, 36:1104–1122, 2006.

[79] S. R. Ramp, T. Y. Tang, T. F. Duda, J. F. Lynch, A.K. Liu, C. S. Chiu, F. L. Bahrand, H. R. Kim, and Y. J. Yang. Internal solitons in the northeastern South China Sea part I: Sources and deep water propagation. *IEEE J. Oceanic Eng.*, 29(4):1157–1181, 2004.

[80] R. D. Ray and G. T. Mitchum. Surface manifestation of internal tides in the deep ocean: Osbservations from altimetry and island gauges. *Prog. Oceanog.*, 40:135–162, 1997.

[81] R. M. Robinson. The effects of a barrier on internal waves. *Deep Sea Res.*, 16:421–429, 1969.

[82] H. L. Simmons, R. W. Hallberg, and B. K. Arbic. Internal wave generation in a global baroclinic tide model. *Deep Sea Res. II*, 51:3043–3068, 2004.

[83] L. C. St. Laurent and C. Garrett. The role of internal tides in mixing the deep ocean. *J. Phys. Oceanogr.*, 32:2882–2899, 2002.

[84] L. C. St. Laurent and J. D. Nash. An examination of the radiative and dissipative properties of deep ocean internal tides. *Deep Sea Res. II*, 51:3029–3042, 2004.

[85] L. C. St. Laurent, S. Stringer, C. Garrett, and D. Perrault-Joncas. The generation of internal tides at abrupt topography. *Deep Sea Res. I*, 50:987–1003, 2003.

[86] A. Tabaei, T. R. Akylas, and K. G. Lamb. Nonlinear effects in reflecting and colliding internal wave beams. *J. Fluid Mech*, 526:217–243, 2005.

[87] W. Tang and T. Peacock. Dynamics of double ocean ridges. In preparation.

[88] Y. K. Tsang W. R. Young and N. J. Balmforth. Near-inertial parametric subharmonic instability. *J. Fluid Mech.*, 607:25–49, 2008.

[89] H. P. Zhang, B. King, and H. L. Swinney. Experimental study of internal gravity waves generated by supercritical topography. *Phys. Fluids*, 19:096602, 2007.

[90] Z. Zhao and M. H. Alford. Source and propagation of internal solitary waves in the northeastern South China Sea. *J. Geophys. Res.*, 111(C11012), 2006.